

Structural Aspects
of an
Arched Glass Masonry Bridge

Mike Aurik

Structural Aspects
of an
Arched Glass Masonry Bridge

in partial fulfillment of the requirements for the degree of

Master of Science

in Structural Engineering
at the Delft University of Technology
to be defended publicly on January 31, 2017

Mike Aurik

January 24, 2017

Cover image

Mock up of a 1m-span
glass arch, constructed
for the experimental
research in this thesis

Author

Mike Aurik
+31(0)615458795
mikeaurik@gmail.com

University

Delft University of Technology
Faculty of Civil Engineering and Geosciences
Master Structural Engineering, Structural Mechanics

Thesis committee

Prof.ir. R. Nijse (Chair)	TU Delft
Dr.ir. M.A.N Hendriks	TU Delft
Dr.ir. P.C. Louter	TU Delft
ir. A. Snijder	TU Delft
ir. D. Tuinstra	Arup
ir. C. Noteboom	Arup

Preface

You are looking at the final report of my graduation research, which I conducted to complete my master Structural Engineering, at the TU Delft.

The topic of the research resulted from the ambition of TU Delft's glass group, to realize a 14m span, arched glass masonry, pedestrian bridge. Due to the innovative nature of this project, a research about the structural behavior of such structures was desired.

I would like to thank my thesis committee for their expertise and feedback. More specifically, I would like to acknowledge Rob Nijssse for taking the lead in this and excellently fulfilling his role as chair of the committee. Furthermore, I would like to thank Max Hendriks for his critical view and his valuable comments. Thereby I really appreciated his quick responses to any of my messages. Therewith I would like to thank Cristian Louter for his expertise in glass structures and for indicating the points of attention for the experimental research. Perhaps most importantly, is to acknowledge Ate Snijder, for bringing me on board of the glass masonry bridge team in the first place. Possibly I never would have gotten to know the interesting world of glass structures otherwise. I have enjoyed our late night discussions and brainstorm session over a beer. Therewith I would like to acknowledge his contribution in the preparations for- and the execution of the experiments.

Also I would like to acknowledge, Fred Veer, Telesilla Bristogianni, Kees Baardolf and Kees van Beek, for their assistance and expertise with respect to the experimental research.

Furthermore I would like to thank Dimitri Tuinstra for providing me with the opportunity to graduate at the Arup office. In general I would like to thank the Arup-staff for their interest in my research and the input that they have given me. Most of all I would like to thank Chris Noteboom for his endless enthusiasm and for all his efforts in thoroughly reflecting on my work. Due to both our curiosity, our discussions would end far after working hours, only to be continued in the train on the way home. By asking the right questions, you have encouraged me to dig deeper into the relatively unclear aspects of my work.

Finally I would like to thank my family, friends and Sophie for their support, understanding and for motivating me throughout my graduation.

Mike Aurik

Rotterdam, January 2017

Abstract

The glass group of the TU Delft plans to realize a 14m span glass arched masonry bridge, yet no prescriptions are available on how to assess the structural safety of such a structure. Regulations and guidelines for structural glass relate to float glass elements and do not refer to structures of cast glass elements. In addition, to display the aesthetic glass masonry structure, the arch directly serves as deck limiting the slope of the arch. Therefore its rise is relatively low compared to traditional stone masonry structures. It is unknown how this will affect the stability. In this report the stability and strength of arched glass masonry bridges is investigated. In addition TU Delft's design is elaborated upon in more detail.

In order to establish which aspects are important when designing in glass, references of both glass bridges as well as glass brick structures are discussed. Subsequently a theoretical background is formed for both arched masonry, as well as for structural glass. In analytical investigations, the effect of the geometry on the stability is assessed. Both an analytical as well as a numerical analysis of the stability have been executed for the boundary conditions of TU Delft's design. Resilient interlayers may be applied to limit the tensile stresses introduced by imperfect conditions, i.e. an imperfect surface flatness of the glass and a discontinuous stress distribution due to an eccentric line of thrust. These imperfect condition were analytically respectively numerically investigated, in order to enable the formulation of a maximum interlayer-stiffness. This maximum interlayer stiffness will assure that the maximum tensile stress remains sufficiently low. This was followed by an experimental assessment of three interlayer materials in four thicknesses, to establish their suitability for application as interlayer in TU Delft's design. Finally, the failure behavior with respect to the strength was established, resulting from experimental research in which a 1m span glass arch was loaded.

Several design diagrams were composed that can be used to define the geometry of a circular segmented arch, taking into account the stability of the structure. A glass element in the arch is loaded in compression, but will only fail if too high tensile stresses are introduced as a result of imperfect conditions. If sufficiently large, the eccentricity of the line of thrust will cause tensile stresses. An imperfect glass surface may also introduce tensile stresses. An interlayer may be used to resolve these problems, if its stiffness is not too large. If fracture in a glass brick occurs, this will likely not lead to global failure, which means that the failure behavior of an arched glass masonry bridge is ductile.

The stability of TU Delft's glass masonry bridge is sufficient under the expected support settlements, as well as under an asymmetrical crowd load scenario. The load scenario concerning a service vehicle, significantly reduces the stability. It is therefore recommended to prevent entrance for service vehicles. Resilient interlayers with a stiffness between $26N/mm^3$ and $40N/mm^3$ should be applied between the bricks to assure adequate stress transfer, without compromising the stability. From the experimental research it followed that a 1mm-PVC or a 4mm-PU70 interlayer will be suitable. The design is deemed feasible, but before construction additional investigations on the time and temperature-dependent behavior of the interlayer should be executed. Additionally the strength of the full scale bricks must be assessed, too guarantee it is sufficient to resist the design loads.

Table of Contents

I Introduction

1	Introduction	3
1.1	Introduction of the research	3
1.1.1	Problem introduction	5
1.2	Objective and methodology	5
1.2.1	Objective	5
1.2.2	Methodology	6
1.3	Outline	7

II Theoretical Framework

2	Glass Footbridges	11
2.1	Introduction	11
2.2	Glass footbridge references	11
2.2.1	First glass bridge, Rotterdam 1994	11
2.2.2	A Dutch treat, Arnhem 1996	12
2.2.3	Double trouble, Arnhem 1998	13
2.2.4	BRÜCKE 7, Stuttgart 2008	13
2.2.5	Single span 9m long glass bridge, Toronto 2010	14
2.2.6	Glass bottomed suspension bridges	15
2.3	Glass footbridge concepts	16
2.3.1	Glass icicles, Hoofddorp, 2002	16
2.3.2	Thomas Heatherwick 2012	17
2.4	Evaluation	17
3	Glass Brick Structures	19
3.1	Introduction	19
3.2	Key factors	19
3.3	Glass brick facade references	21
3.3.1	Maison Hermes, Tokyo 2013	21
3.3.2	Optical House, Hiroshima 2012	22
3.3.3	Atocha memorial, Madrid 2007	22
3.3.4	Crystal House, Amsterdam 2016	24
3.4	Evaluation	26

4	Arched Masonry	27
4.1	Introduction	27
4.2	Arched support system	28
4.2.1	Line of thrust	28
4.2.2	Parabolic shape	29
4.2.3	Catenary	29
4.2.4	Approximation of the catenary	30
4.3	Masonry arches	31
4.3.1	Structural criteria	31
4.3.2	Elastic and plastic approach	33
4.3.3	Safety	33
4.3.4	Construction	34
4.4	Differential equation method	36
5	Structural Glass	39
5.1	Introduction	39
5.2	Material characteristics	39
5.2.1	Nanoscale structure	39
5.2.2	Properties	41
5.3	Production process	42
5.3.1	Float glass	43
5.3.2	Cast glass	43
5.4	Strength	44
5.4.1	Failure mode	45
5.4.2	Flaw size	45
5.4.3	Flaw shape	45
5.4.4	Static fatigue	46
5.4.5	Uncertainty in strength	47
5.4.6	Design value strength	48
5.4.7	Thermal treatment of the glass	48
5.4.8	Laminated glass	49
5.5	Safety and design	50
5.5.1	Risk	50
5.5.2	Design methods	51
5.5.3	Computing deformations and stresses	51
5.5.4	Force introduction	52
5.5.5	Design codes for glass	53
5.5.6	Risk reduction	54

III

Analytical and Numerical Stability Analysis

6	Analytical Stability Analysis	57
6.1	Introduction	57
6.2	Imposed displacements	59
6.2.1	Introduction	59
6.2.2	Definitions of the region-boundaries	60

6.2.3	Settlement analysis	62
6.2.4	Volume optimization	65
6.2.5	Geometrical non-linearity	66
6.2.6	Stability verification	67
6.3	Asymmetric load configurations	73
6.3.1	Introduction	73
6.3.2	Unconditionally stable arch	73
6.3.3	Analytical safety assessment	74
6.3.4	Case study: Resistance against asymmetrical load configurations	77
6.3.5	Thickness design graph	83
6.4	Results and Conclusions	84
6.4.1	Design diagrams	84
6.4.2	Case study analysis	84
7	Numerical Stability Analysis	87
7.1	Introduction	87
7.2	General model description	87
7.2.1	Model overview	88
7.2.2	Non-linearity	89
7.3	Support displacements	91
7.3.1	Symmetrical load scenario	91
7.3.2	Imposed displacements at instability	92
7.4	Asymmetric load scenario	94
7.5	Combination: Asymmetric and support displacements	96
7.6	Reduced interface stiffness	97
7.7	Conclusions	100
7.7.1	On Validation	100
7.7.2	Non-linear analysis method	100
7.7.3	Combination	100
7.7.4	Interlayer-stiffness	100
7.7.5	General conclusions	100

IV

Analytical and Experimental Stress Analysis

8	Glass in compression	103
8.1	Introduction	103
8.1.1	Introduction	103
8.1.2	Global effect	104
8.1.3	Local effect	104
8.2	Tensile stress due to global effect	105
8.3	Tensile stress due to local effect	109
8.3.1	Introduction	109
8.3.2	Interlayer-stiffness design	109
8.4	Interlayer-material selection	110
8.5	Conclusions	111

9	Experimental research	113
9.1	Introduction	113
9.2	Stacked glass-interlayer system	114
9.2.1	Introduction	114
9.2.2	Description of the experimental setup	114
9.2.3	Results	115
9.2.4	Conclusions and Recommendations	122
9.3	Glass arch scale test	123
9.3.1	Introduction	123
9.3.2	Description mock-up construction	123
9.3.3	Photographic displacement measurements	125
9.3.4	Photo-elastic stress measurements	128
9.3.5	Failure behavior	131
9.3.6	Conclusions and Recommendations	133

V

Conclusions and Recommendations

10	Conclusions and Recommendations	137
10.1	Introduction	137
10.2	General results and conclusions	137
10.3	Conclusions and recommendations for case study	138
10.4	Recommendations for future research	139

VI

Appendices

A	Tensile strength NEN 2608:2014	143
A.1	Strength assumption glass brick	143
B	Actions on a pedestrian bridge	145
B.1	Load cases	145
B.1.1	Permanent load	145
B.1.2	Traffic load	145
B.1.3	Wind load	146
B.1.4	Temperature load	147
B.2	Load combinations	149
B.2.1	Partial factors	150
B.2.2	Combination factors	150
B.2.3	Load combinations	150
B.3	Load Scenarios	151
B.3.1	Fundamental load configurations	151
B.3.2	Load scenarios	152
C	Derivations	153
C.1	Derivation I,f,t-notation of the boundary AB	153

C.2	Extraction and conversion of results regarding the span increase till collapse	153
C.3	Time-dependent stiffness derivation (Experiment)	155
C.4	Derivation differential equation of a cable	156
D	Assumptions and accuracy	157
D.1	Load distribution	157
D.2	Deviation of the line of thrust	158
D.3	Circle expression	160
E	Background information	161
E.1	Scale levels of imperfections	161
E.2	Fine and Kinney	162

VII**Bibliography**

Bibliography	167
---------------------------	------------

Nomenclature and Abbreviations

Symbol	Description
A	Area
A_{steel}	Cross sectional area steel tie
E	Young's modulus
E_{int}	Young's modulus of the interlayer-material
$E_{int,eff}$	Effective young's modulus of the interlayer-material
F	Point load
H	Horizontal component of the axial force
H_{crit}	Critical value for horizontal component of the axial force
$HK_{0.1/20}$	Hardness
P	Axial force
Q_{SV1}	First axle load of service vehicle
Q_{SV2}	Second axle load of service vehicle
I	Moment of inertia
M	Internal moment
R	Radius
T	Length of the brick
T_g	Glass transition temperature
T_s	Melting temperature
V	Shear component of the axial force
V_z	Vertical component of the axial force
q_{crit}	Critical value for applied distributed load
q_d	Distributed design load
$q_{hingeshift}$	Distributed load at which hinges start shifting
u_{crit}	Horizontal support displacement, when critical load is reaches
u_{max}	Maximum horizontal support displacement
w_{max}	Maximum deflection
b	Width of the arch
d	Diameter
f	Rise of an arch
$f_{mt;u;d;}$	Design value for the tensile strength
k	Horizontal support stiffness
l	Span of an arch
n	Poission's ratio
q	Distributed load
q_c	Distributed load, distributed along the arch its curve
q_G	Distributed load due to self weight
q_T	Distributed load due to trafic
q_W	Distributed load due to wind
t	Time; Thickness arch
t_{int}	Thickness of the interlayer
$t_{minimal}$	Minimal required arch thickness for stability under a load scenario

u	Displacement
u_{exp}	Expected deformation
u_l	Linear horizontal displacements of the supports
u_{nl}	Nonlinear horizontal displacements of the supports
u_{tot}	Total horizontal displacements of the supports
$u_{tot,d}$	Design value of the total horizontal displacements of the supports
$u_{tot,collapse}$	Total horizontal displacements of the supports at collapse
u_H	Horizontal support displacement due to horizontal component axial force
u_q	Horizontal support displacement due to distributed load
w	Deflection
w_0	Initial deflection
α	Thermal expansion coefficient
α_t	Angle at which the line of thrust is tangent to the intrados
β	half angle of embrace
Δ	Maximum deviation of an imperfect surface-flatness
ΔT_M	A linear variable temperature component
ΔT_N	An evenly distributed temperature component
θ	Angle between the centroidal axis and the horizontal
κ	Curvature
λ	Thermal conductivity
ϕ	Rotation
ρ	Density
$\sigma_{c;u;d}$	Design compressive strength
$\sigma_{contact}$	The stress that develops before full interlayer contact is achieved
$\sigma_{int,max}$	Maximum occurring stress in interlayers
$\sigma_{princ,comp,max}$	Maximum occurring principal compressive stress
σ_{xx}	Stress in x-direction
σ_{avg}	Applied average stress
ξ	Span increase factor

Abbreviation	Description
AN	Annealed glass
CNC	Computer Numerical Control
EVA	Ethyl Vinyl Acetate
FEM	Finite Element method
FT	Fully tempered glass
GSF	Geometrical Safety Factor
HS	Heat-strengthened glass
PU70	Polyurethane 70 Shore A
PU90	Polyurethane 90 Shore A
PVB	Polyvinyl butyral
PVC	Polyvinyl chloride
SG	Sentry Glass



Introduction

1	Introduction	3
	1.1 Introduction of the research	3
	1.2 Objective and methodology	5
	1.3 Outline	7

1 Introduction

1.1 Introduction of the research

Over the last few decades there have been significant developments regarding the structural application of *float glass*. These developments are driven by a desire for transparency. The pursuit of transparency is perfectly illustrated by the example given in Figure 1.1. It shows the Apple Store in New York, which was built in 2006 and then replaced by a more transparent version 5 years later. Developments in production allowed for the application of larger panels, that enabled a more transparent structure.



(a)



(b)

Figure 1.1: The substantiation of the pursuit of transparency; (a) Apple store New York in 2006, taken from idesignarch.com; (b) Rebuild Apple store in 2011, taken from architizer.com;

The structural behavior of *float glass* elements may have been extensively researched over the last few decades. However, the behavior of *cast glass* structures is relatively unknown. The casting process can be used to make solid glass elements (e.g. bricks), from which a larger structure can be composed. Although these structures may be considered transparent, rendering an invisible structure is not the focus. Rather than doing so, the refractive and reflective capabilities of glass are used to display an aesthetically appealing result. This is emphasized by Figure 1.2, which shows the recently completed Crystal Houses, located at 'de P.C. Hooftstraat' in Amsterdam. The facade is a masonry structure in which solid glass bricks are joint by a transparent adhesive.

By means of experimental research, the glass group of the TU Delft has significantly contributed to the realization of the Crystal Houses. Resulting from the acquired knowledge



Figure 1.2: An impression from within the Crystal Houses in Amsterdam, taken from mvrdrv.nl; The solid glass bricks aesthetically reflect and refract the light;

on cast glass, curiosity about its potential arose. Subsequently a new goal was formulated: The realization of a glass masonry bridge. This is a structurally more complex application, which cannot be found anywhere else in the world yet. The design for TU Delft's glass masonry bridge is illustrated in Figure 1.3.



Figure 1.3: An impression of the design for TU Delft's glass masonry bridge, taken from Snijder et al. (2016);

1.1.1 Problem introduction

At this point no prescriptions are available on how to assess the structural safety of a glass masonry bridge. Regulations and guidelines on structural glass are based on float glass elements. Therefore it is relatively hard to establish the safety of cast glass structures. Although some know-how resulted from the Crystal Houses, the concept of a masonry bridge is more complex.

In order to display the aesthetic glass masonry structure, it is assumed that the glass arch serves directly as bridge deck, such as shown in the design in Figure 1.3. Since the arch serves directly as deck, it must not be too steep. This results in a relatively flat arch, compared to traditional masonry arches. It should be established how this will affect the stability.

Understanding the structural behavior of a glass masonry arch is essential to establish its safety. Establishing which parameters significantly affect the structural response and how they do it, is necessary to provide a safe and economic design.

1.2 Objective and methodology

1.2.1 Objective

The objective of this research is to understand the structural behavior of an arched glass masonry bridge, to make a reliable safety assessment and well-grounded design choices.

To achieve this objective, a distinction is made between the *global behavior*, which relates to the stability of an arch, and the *local behavior*, which relates to the strength (i.e. the transfer of stresses between the bricks).

With respect to stability, the following research questions are formulated:

In general

- How does the geometry of an arch relate to its stability?
- How can the rise and the thickness of a certain arch be optimized for stability?

For TU Delft's glass masonry bridge (case study)

- Is the arch sufficiently stable for the chosen geometry?
- If a resilient interlayer would be applied, what is the minimal interlayer-stiffness before instability occurs?

With respect to the strength, the following research questions are formulated:

In general

- How does a non-slender glass brick fail in compression?
- How does the maximum tensile stress relate to the brick dimensions and the eccentricity of the line of thrust?
- How to formulate the maximum interlayer-stiffness, to assure adequate stress transfer between bricks?
- Is the failure behavior of a glass arch brittle or ductile?

For TU Delft's glass masonry bridge (case study)

- Which material and thickness combination is most suitable for application as interlayer in the design?

1.2.2 Methodology

Analytical research

Stability: To answer the stability-related questions, an analytical analysis is made which regards the position of the line of thrust within the arch-geometry. Both instability due to settlements and due to an asymmetrical load configuration is investigated.

Strength: For adequate stress transfer a method to formulate a maximal interlayer stiffness is proposed based on analytical considerations.

Numerical research

Stability: Finite element analysis are executed for the case study, in order to verify the analytical results. After establishing adequate functioning of the FEM, the effect of a stiffness reduction due to the application of an interlayer is investigated. A lower bound for the interlayer-stiffness can be formulated.

Strength: Through a series of FEM-models it is established how the maximum tensile stress relates to the brick dimensions and the eccentricity of the line of thrust.

Experimental research

Column-test: An experimental setup is made in which a stack of glass bricks with an interlayer (PVC/PU70/PU90) is loaded. Therewith the time-dependend stiffness is established as well as the thickness-stiffness relation. Based on previously established requirements, an interlayer for the case study can be recommended.

Arch-test: A 1m span glass bridge is loaded to validate the displacement field that follows from the FEM-analysis, therewith establishing the accuracy of the stability analysis. The stress distribution is visualized to provide insight in the stress flow in the arch, which relates to the position of the line of thrust. The experiment concludes with destructive tests which establish the failure behavior (brittle/ductile).

1.3 Outline

The outline of this report is illustrated in Figure 1.4. As shown, it is divided into five parts. Chapter 1, in part I, introduces the research. Subsequently, part II provides a theoretical framework for the research. Chapter 2 and Chapter 3 discuss several references of glass bridges and glass brick structures respectively. It is established which aspects are important when designing in glass. In Chapter 4 the relevant aspects concerning arched masonry are elaborated upon. It serves as a basis for the stability related research in part III. In Chapter 5 a background on glass is provided. It serves as a basis for the strength related research in part IV.

In part III, the stability of the arch is investigated. In Chapter 6 it is analytically investigated how the geometry of the arch relates to its stability. In Chapter 7 a numerical analysis is executed for TU Delft's design specifically. The results are compared to the analytical solutions and it is investigated what the minimal stiffness of an interlayer should be.

In part IV, the strength-related failure is investigated. Chapter 8 establishes the maximum stiffness of an interlayer to assure an adequate stress transfer, which will result in sufficient strength. In Chapter 9, the suitability of several interlayers is determined by an experiment in which a stack of glass bricks and interlayers is compressed. The interlayers have been selected based on the stiffness interval for TU Delft's design. Another experiment was executed to establish the failure behavior of an arched glass masonry bridge. In this experiment a 1m mock-up was loaded till failure.

The conclusions resulting from the analytical, numerical and experimental research are provided by Chapter 10 in part V.

The investigations in this report are partially about glass masonry bridges in general and partially about TU Delft's design (the case study). The numerical analyses in Chapter 7, hold for the case study only. The investigations in the other chapters hold in general, except when specifically indicated by the box for the case study:

Case study: Information in this box relates to the case study and does not hold in general.

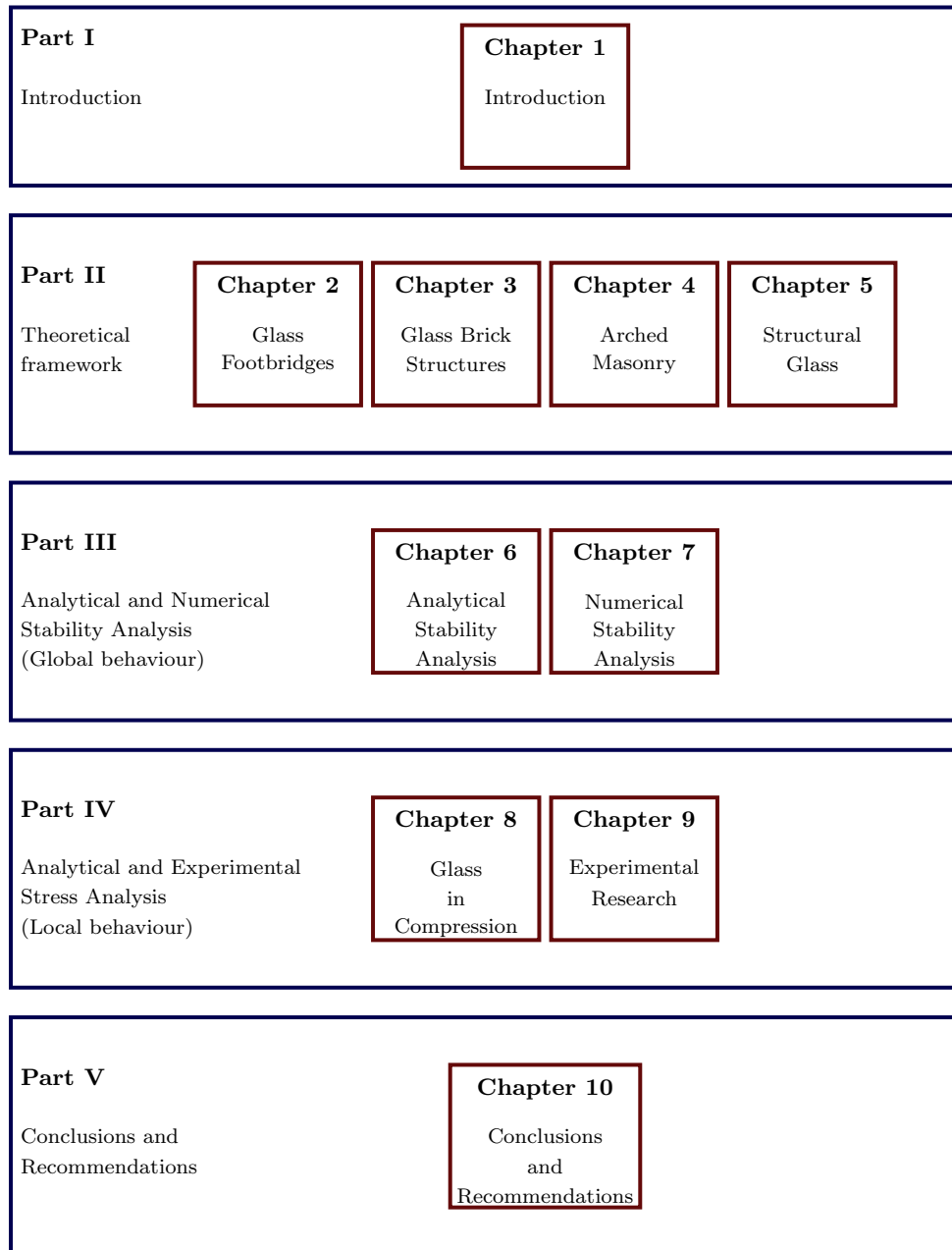


Figure 1.4: Report outline;



Theoretical Framework

2	Glass Footbridges	11
2.1	Introduction	11
2.2	Glass footbridge references	11
2.3	Glass footbridge concepts	16
2.4	Evaluation	17
3	Glass Brick Structures	19
3.1	Introduction	19
3.2	Key factors	19
3.3	Glass brick facade references ..	21
3.4	Evaluation	26
4	Arched Masonry	27
4.1	Introduction	27
4.2	Arched support system	28
4.3	Masonry arches	31
4.4	Differential equation method ..	36
5	Structural Glass	39
5.1	Introduction	39
5.2	Material characteristics	39
5.3	Production process	42
5.4	Strength	44
5.5	Safety and design	50

2 Glass Footbridges

2.1 Introduction

A bridge in which a glass brick structure is implemented, would be the first one ever made. Although the combination 'glass brick structure' and 'glass bridge' does not exist yet, there are several references of such concepts independently. In this chapter footbridges composed from float glass elements will be discussed. Several references of existing bridges are discussed first. This is followed by some interesting concepts that have not been realized. For references of glass brick structures is referred to Chapter 3.

2.2 Glass footbridge references

2.2.1 First glass bridge, Rotterdam 1994

When the architectural firm Kraayvanger Urbis was expanding to the first floor of an adjacent building, they wanted to create an indoor connection. The architecture of both buildings was quite sober, so it was difficult to come up with a design that would fit well in its surroundings and was interesting at the same time. For this reason, possibilities for a transparent connection using glass were discussed with ABT. The 3.5m span was realized by splitting up the bridge in a 'structural part' and a 'raincoat'. The raincoat is an independent structure, consisting of the walls and the roof.

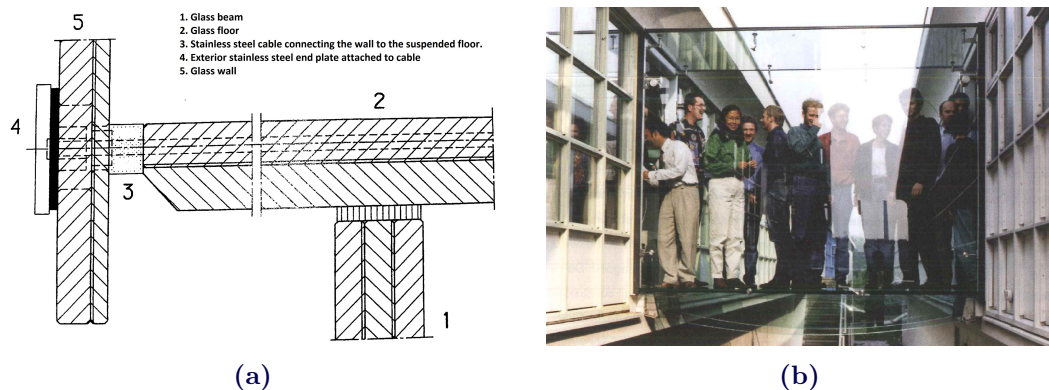


Figure 2.1: First glass bridge, taken from Nijssen (2003); (a) Connection detail of the beam, floor and wall; (b) The bridge during test loading;

The structural part consists of the floor and the beams supporting it. The beams are composed of three layers of 10mm toughened float glass and the floor is of two layers of 15mm toughened float glass. Those are laminated, using PVB as interlayer. The beams are connected to the floor using a structural silicone. The detail in Figure 2.1a shows this connection, as well as the floor-to-wall connection. In order to maintain the structural independent behavior, the floor and wall were connected by a cable, which does not transfer internal moments or shear forces. The client, architect and contractor agreed to all take a

certain part of the risk of this innovative structure. Figure 2.1b shows the test loading after realization of the project. The safety is ensured by the concept of outside layers protecting the inner ones. One time the bridge was vandalized: a street-tile was thrown. The first layer was cracked, while the rest of the bridge remained intact. The multiple layer concept proved to be safe. (Nijssse, 2003)

2.2.2 A Dutch treat, Arnhem 1996

Shortly after the realization of the first glass bridge, an improved version (designed by ABT) was built in Arnhem. This time a slightly bigger span of 3.8m had to be realized, to connect an older- and a more recent building of the Arnhem Zoo. For this bridge no mechanical connections were used. Instead, simple silicone joints were applied for all glass-on-glass connections. The ability of such joints to transfer small stresses was recognized by the local authorities at this moment. Originally, the concept was to use the walls as a load-carrying beam. The contractor found this idea too risky at the time, thus independent beams were used after all. The bridge is composed of the elements shown in Figure 2.2a. The elements consist of toughened float glass panes, laminated using PVB as an interlayer. An interesting practical aspect of this bridge, is the curved roof that enables the rainwater to flow down. (Nijssse, 2003)

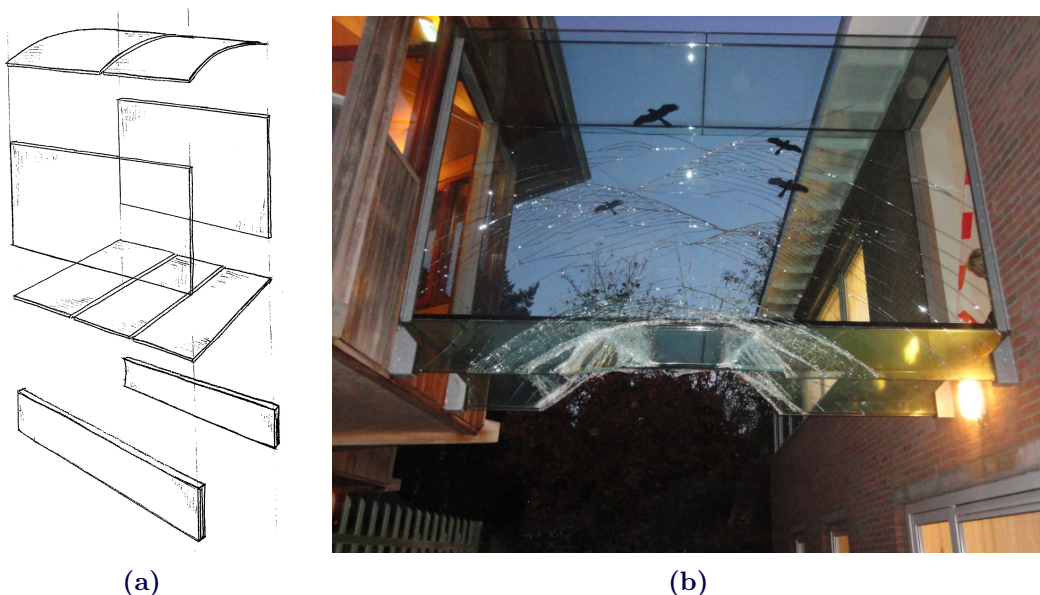


Figure 2.2: First glass bridge in Arnhem; (a)Exploded view, taken from Nijssse (2003); (b)Broken Arnhem-bridge in 2012, taken from Brincke (2013);

In 2012 there was an incidental collision between a forklift and the glass bridge. This caused the toughened glass to break, see Figure 2.2b. However, due to the application of laminated elements, the bridge did not fail. The bridge was rebuilt, but this time annealed glass was used instead of toughened glass. This type of glass has a lower strength, but generally people feel safer when its broken. This can be explained from the breaking pattern of annealed glass, which shows less fragmentation. Because of this, it also provides a bigger residual capacity. The new design was also improved in terms of sustainability. Insulated glass was applied to meet the higher thermal insulation standards. (Brincke, 2013)

2.2.3 Double trouble, Arnhem 1998

Another project for the Arnhem Zoo followed. This time a height difference had to be overcome as well. For this reason, stairs were incorporated in the glass bridge, as illustrated in Figure 2.3. To achieve this, the beam was shaped like the stairs. By using techniques such as water-jet cutting, customized shapes can be realized. Besides from this customized shape, the design is similar to the first glass bridge in Arnhem. (Nijse, 2003)



Figure 2.3: Second glass bridge in Arnhem, incorporating a glass stairs, taken from Nijse (2003);

2.2.4 BRÜCKE 7, Stuttgart 2008

The bridge shown in Figure 2.4, is an applied research project developed by the University of Stuttgart. It spans 7m and consists of a curved walkway and two curved glass parapets. The combination of those single curvature elements, produces a three-dimensional body. Traditionally, glass is curved plastically at temperatures exceeding 640°C, so called hot-bent glass. This method causes the glass to lose its stiffness and produces flaws during heating and cooling. These disadvantages do not arise when cold-bending glass. Brücke 7 consists of 4mm thin glass panes that were bended and then kept in position by a frame. After lamination in the autoclave, the curved laminate could be removed from the frame. The thin glass panes have a low flexural stiffness and allow for a radius of 16m, producing a flexural stress of about 9MPa. Therefore it was possible to obtain the desired curvature.

The walkway consists of eight glass panes laminated using 1.5mm-thick SG-foils as interlayer. The parapets contain six glass panes and the same interlayer. Figure 2.5 shows such a cold bended element. The SG-foils are considerably stronger and stiffer than the PVB-foils. Therefore, the laminated curved glass element approaches a monolithic behavior. The arch, with a 'rise/span'-ratio of 1/18, increases the structural performance of the bridge. Evenly distributed loads result in compression forces. The rigid abutments are of vital importance for this principle to work. For asymmetric load cases, the parapets provide the necessary support. The parapets are connected to the walkway by an elastic two-component silicone joint. (Bensing et al., 2010)

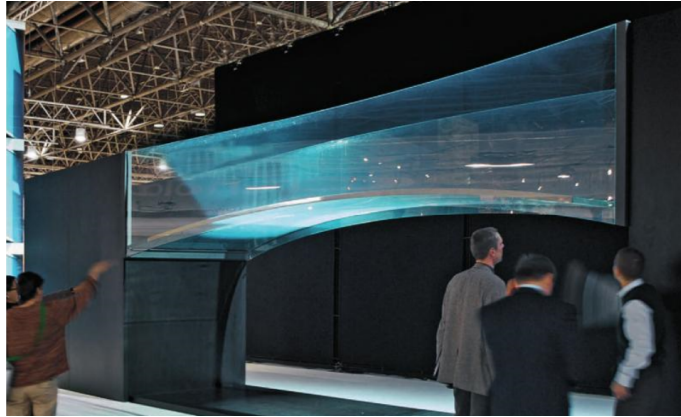


Figure 2.4: Arched bridge made of cold deformed curved glass, taken from Bensing et al. (2010);

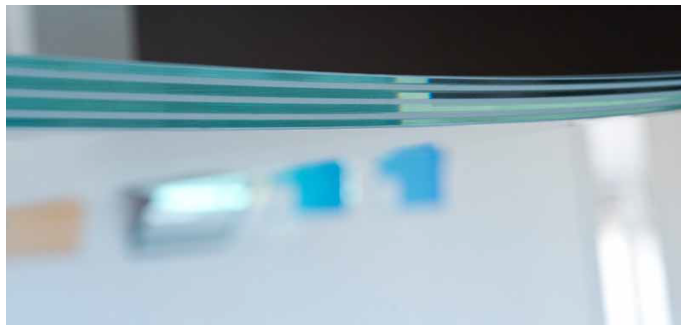


Figure 2.5: Laminated thin cold-bent glass, taken from Louter (2016);

2.2.5 Single span 9m long glass bridge, Toronto 2010

To complete the look of a hotel in Toronto, Halcrow Yolles designed a glass bridge spanning across the lobby on the mezzanine level. The structure consists of two balustrades, which serve as main beams. Cross beams, in which the glass floor panels are secured, span between them. Stainless steel brackets connect the main- and cross beams, as illustrated in Figure 2.6a. A detailed finite element analysis was executed to minimize the amount of steel. In this way maximum transparency was achieved.

In the original design, the balustrades consisted of three separate panels connected by splice joints. This was deemed necessary, due to the limited production sizes of glass sheets. The availability of unique glass products grew during the project. By reducing the original 10m span by 1m, the balustrades could be fabricated from one piece. It was decided to do so, since this would result in a more transparent and simpler structure. At both ends of the bridge, the half meter gap was filled using steel platforms. The safety of the bridge is assured by the application of laminated glass. All elements consist of three layers of glass, laminated with a PVB interlayer. Exposed layers are fully tempered, in order to increase the impact resistance. The remaining layers are heat-strengthened to ensure adequate post breakage rigidity. The completed glass bridge is shown in Figure 2.6b. (Wittenberg and Krynski, 2010)

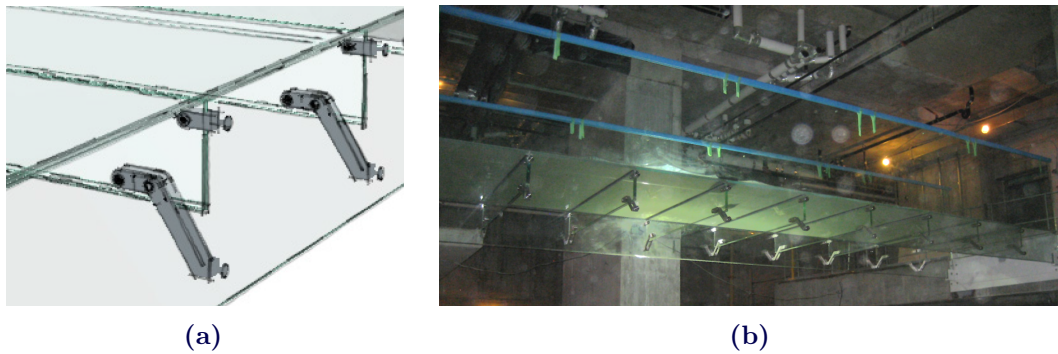


Figure 2.6: Nine meter spanning glass bridge, taken from Wittenberg and Krynski (2010); (a)Main- and cross beam connection; (b)Completed bridge;

2.2.6 Glass bottomed suspension bridges

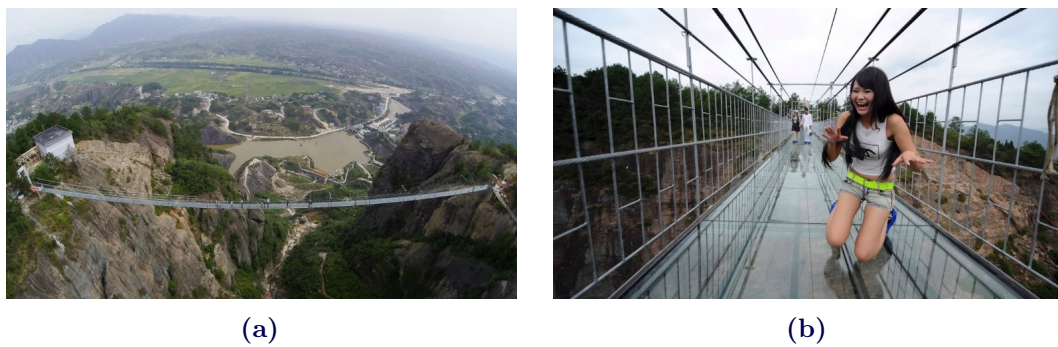


Figure 2.7: Glass bottomed suspension bridge in China, spanning 300m, taken from Wong (2015); (a)The suspension bridge spanning the cliff; (b)The transparent walkway;



Figure 2.8: Second glass bottomed suspension bridge, spanning 375m, taken from Lyme (2015); (a)Bridge under construction; (b)Artist impression;

The 300m suspension bridge illustrated in Figure 2.7a, is located in China and was finished in 2015. Figure 2.7b shows the glass floor situated in the steel structure. Although the structural application of glass is limited to floor panels in this project, the psychological aspects are rather interesting. A lot of people are scared to walk the 185m high (fragile appearing) “Brave men’s bridge”. The safety is guaranteed by the application of laminated glass, consisting of three tempered glass panes. An incident occurred two weeks after the

opening, causing a top pane to break. Although the safety concept worked, the safety of the bridge is questioned by the general public. This can be partially contributed to the severe fracture pattern of the broken tempered glass panel. (Wong, 2015)

At the moment an even longer (375m) glass bottomed bridge is being constructed in China, as illustrated in Figure 2.8a. An impression of the final result is shown in Figure 2.8b.

2.3 Glass footbridge concepts

2.3.1 Glass icicles, Hoofddorp, 2002

Figure 2.9a shows the glass bridge design developed by ABT for the 2002 Floriade in Hoofddorp. The concept was to use two cantilevering glass structures in order to realize the 21m span. Each cantilever consists of six tapered beams, which are each composed from three elements. The elements consist of four layers of toughened glass. The elements are connected to one another by the 'stitch', shown in Figure 2.9b. This connection can be considered as a truss section. It transfers internal moments and shear forces by axial forces in the bars. Gravity loads will cause tension in the top and diagonal bar. Compression will occur in the bottom bar. (Nijse, 2003)

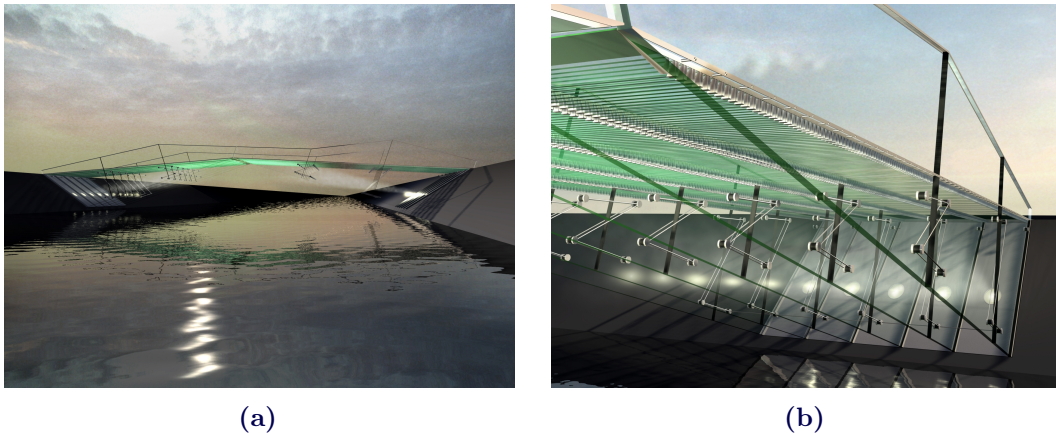


Figure 2.9: Glass bridge design consisting of two cantilevering structures, taken from Nijse (2003); (a) Impression of the cantilevering structure; (b) Impression of the 'stitched' connection;

2.3.2 Thomas Heatherwick 2012

In 2002, Heatherwick was appointed to design the link between ‘Goods Way’ and ‘Granary Square’, across the Regent’s Canal. A concept for an all glass bridge design followed, of which an impression is given in Figure 2.10a. The design consists of 1,334 sheets of 12mm glass, spanning 16m. Pre-stressing is introduced by lever-arm systems, that convert vertical ballast forces into higher horizontal forces. This concept is illustrated in Figure 2.10b. Due to the pre-stressing, the structure functions like a beam. In 2012 the project was dropped due to financial reasons. (Townsend, 2014)



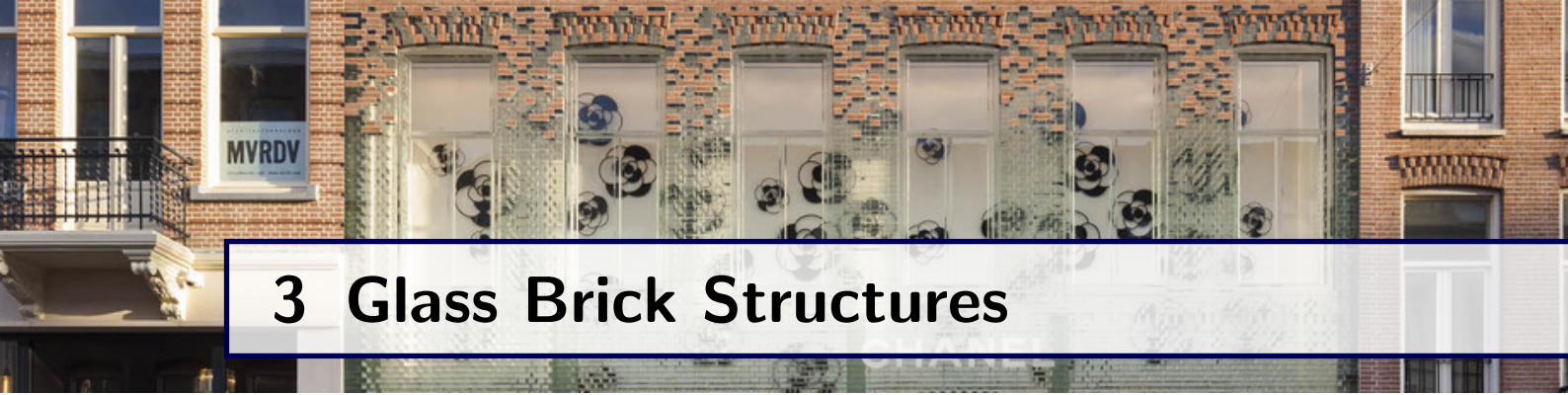
Figure 2.10: Glass footbridge consisting of compressed glass sheets, taken from Rinaldi (2014); (a) Impression of the bridge in its surroundings; (b) Introduction of compression force by lever-arm systems;

2.4 Evaluation

Over the last two decades some interesting glass bridge projects have been developed. A safety concept is an important aspect of a glass bridge design. Generally, a safe glass structure is achieved by the application of laminated elements. Several panes are bonded using a foil. Outer panes, exposed to impact, ‘protect’ the inner panes, so residual capacity is provided. The fragmented panes remain attached. If all panes are broken, residual capacity may result from the bonded fragments.

An interesting consideration is whether or not to apply thermally treated glass. Although it has a higher strength, it provides less residual capacity. This is due to the large amount of cracks, that result in a high fragmentation. In addition, it appears less safe to the general public.

Developments in the glass industry allow for improved glass bridge designs. Increased possibilities for production sizes, allow for bigger single-sheet beams. A higher transparency can thus be accomplished, since no (or less) spliced joints are necessary. Another development is the SG-foil used for lamination of the glass panes. It is considerably stronger and stiffer than the conventional PVB-foils. A higher strength and stiffness of a laminated element can be achieved in this manner.



3 Glass Brick Structures

3.1 Introduction

In Chapter 2, examples of glass bridges were discussed. These bridges are composed from float glass elements. A *bridge* composed from glass bricks does not exist yet. There are however several projects in which self-supporting glass brick systems are applied in a *facade*. The architectural desire for a transparent or translucent barrier between interior and exterior led to the development of these facades. This chapter contains several references of currently realized glass brick facades. The structural performance of those facades depend on certain key factors, which will be discussed first.

3.2 Key factors

According to Oikonomopoulou et al. (2014), there are three key factors that determine the structural performance of a glass brick facade. Figure 3.1 illustrates the following three key factors:

- Brick type
- Joint type
- Overall geometry

The first ‘key factor’ is the type of brick that is used. The choice is based on both structural and aesthetic considerations. Hollow glass bricks are produced by thermally fusing two shallow rectangular cups. The structural capacity of hollow glass bricks is rather limited compared to solid ones. The lower capacity can be attributed to the fact that the thin walls are vulnerable to buckling. According to Dietrich et al. (1995), the compressive strength of hollow glass bricks is about 2.75-4.1MPa. This is a rather low value compared to the strength of solid bricks, which can exceed 200MPa according to Oikonomopoulou et al. (2014).

Besides from those structural considerations, aesthetics is considered as well. The appearance of hollow and solid bricks is quite different. Solid bricks are more or less transparent, while hollow bricks are rather translucent. This difference is attributed to the different distortion of the light. In case of a hollow brick, the light has to pass multiple media and will thus be distorted multiple times. This decreases the transparency of the brick. This phenomenon illustrated in Figure 3.2.

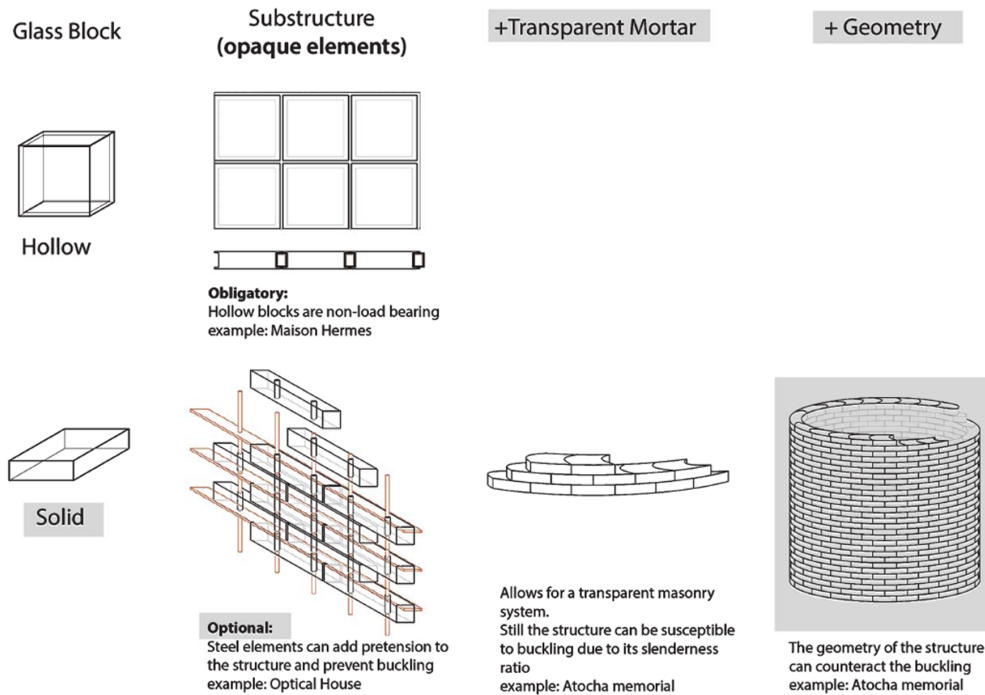


Figure 3.1: Factors determining the structural performance of glass brick facades, taken from Oikonomopoulou et al. (2014);

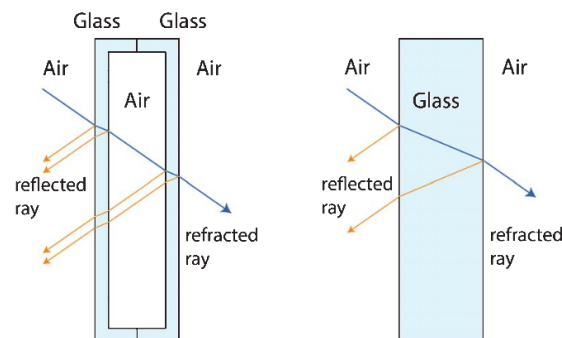


Figure 3.2: Light distortion of a hollow glass brick compared to a solid one, taken from Oikonomopoulou et al. (2014);

The second ‘key factor’, is the way in which the bricks are joined. According to Oikonomopoulou et al. (2014), this is commonly achieved by adding pre-stressed steel elements. Another method is to apply a transparent adhesive. Thus far there are only a few innovative projects that use this method. This can be attributed to the lack of standardized structural specifications.

The final ‘key factor’ to consider, is the geometry of the overall structure. This is of importance, mainly because of lateral loads and buckling modes. Steel reinforcement in a glass brick facade might already resolve those issues, but in an unreinforced glass facade other measurements might be required. By using ‘smart shapes’, such as a circle(segment), buckling modes and lateral loads can be resisted.

3.3 Glass brick facade references

3.3.1 Maison Hermes, Tokyo 2013

As was pointed out, hollow bricks have little structural capacity. Therefore they are commonly used as an ‘infill panel’. Maison Hermes located in Tokyo, is an example of a building in which hollow bricks are applied as such. The concept was to make the building look like a ‘magic lamp’, which is why hollow bricks were used in this case.

Due to the considerable dimensions of the facade, a supporting structure is necessary. Steel elements, attached to the concrete slabs at each floor, fit this purpose. The steel elements slightly separate the glass brick ‘skin’ from the building. The substructure is not clearly visible from the outside of the building. The impression is given that the bricks are carrying the full weight of the 14m high facade, which is illustrated by Figure 3.3a. From the inside of the building however, the support structure is clearly visible, as shown in Figure 3.3b. The glass bricks are located in a metal frame with moving joints. This causes the structure to behave like a skeleton. Controlled displacements are allowed to prevent collapse due to earthquakes. (Piano, 2013)

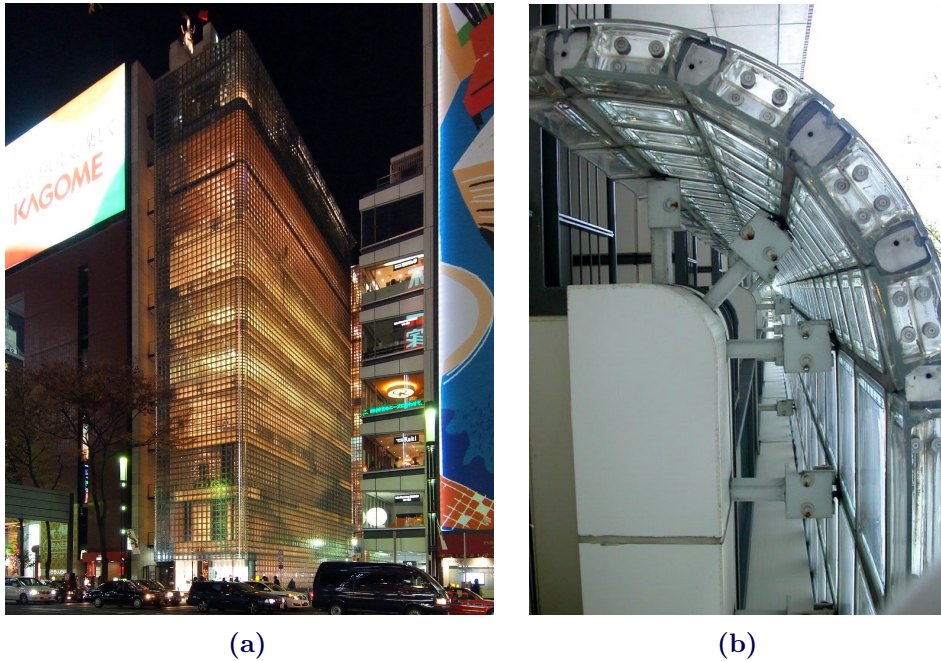


Figure 3.3: Maison Hermes, a hollow glass brick facade, taken from Piano (2013); (a) Impression at night; (b) Connection between concrete floor slabs and steel substructure;

3.3.2 Optical House, Hiroshima 2012

A reference of a glass facade that does use glass as a structural material is the Optical House, located in Hiroshima. This residence is illustrated in Figure 3.4a. Although solid bricks were used in this case, the 8.6m high facade could not stand independently. This is attributed to the slenderness of the bricks. Therefore it was decided to suspend the brick system from a beam at the top of the facade. To accommodate vertical bars within the bricks, they contain two holes each as illustrated in Figure 3.4b. The erection process is illustrated in Figure 3.4c, which clearly shows that the bricks are stung to steel bolts. In order to withstand lateral loads, every certain interval flat steel bars were applied along the glass bricks. The flat bar thickness of 4mm is rather small compared to the 50mm thickness of the glass blocks. In this way the transparency of the facade is not compromised, as shown in Figure 3.4d. (Nakamura, 2012)

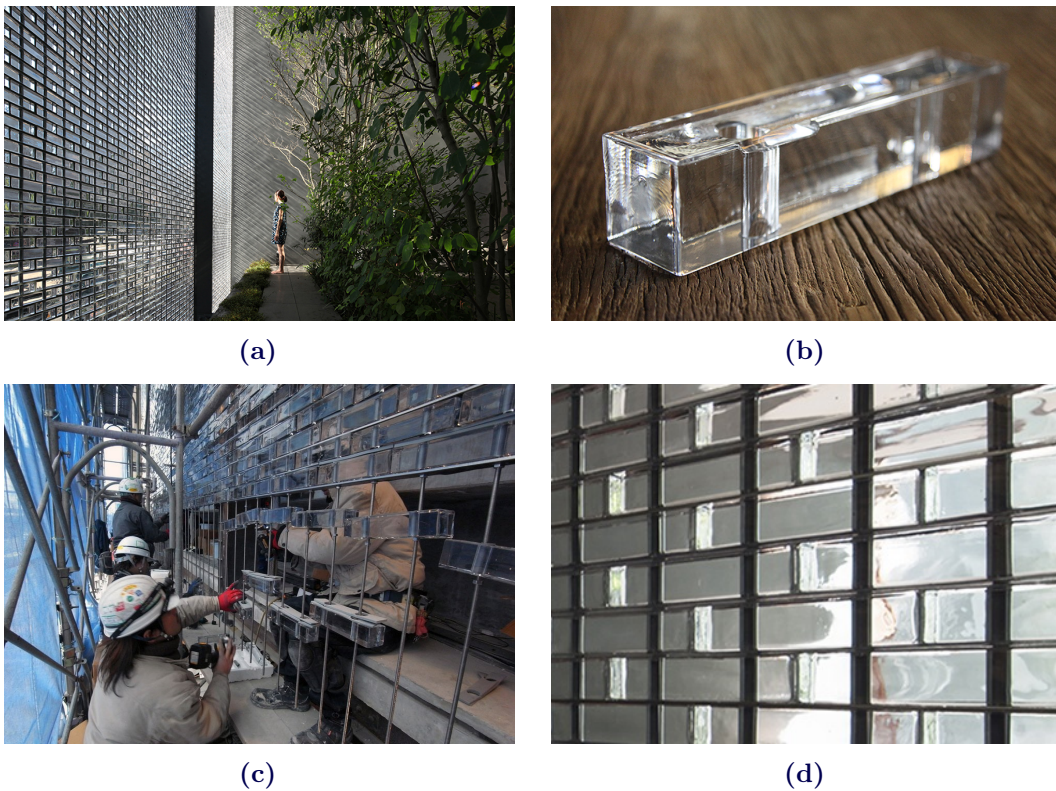


Figure 3.4: The Optical House, a glass brick facade, taken from Nakamura (2012); (a)End result; (b)Glass brick containing two holes to accommodate steel bars; (c)Erection process of the glass brick facade, taken from contemporist.com; (d)Close up from the transparent facade;

3.3.3 Atocha memorial, Madrid 2007

In the Atocha memorial located in Madrid, the structural possibilities of glass are used more extensively. It is an 11m high monument, in which no additional mechanical elements are used. The structure consists merely of glass bricks, joined by a transparent acrylic adhesive. The stability of the memorial is assured by the circular geometry. This geometry is achieved by concave and convex brick ends, as illustrated in Figure 3.5a. They allow the bricks to be connected at a certain angle. A close up of the wall is shown in Figure 3.5b.

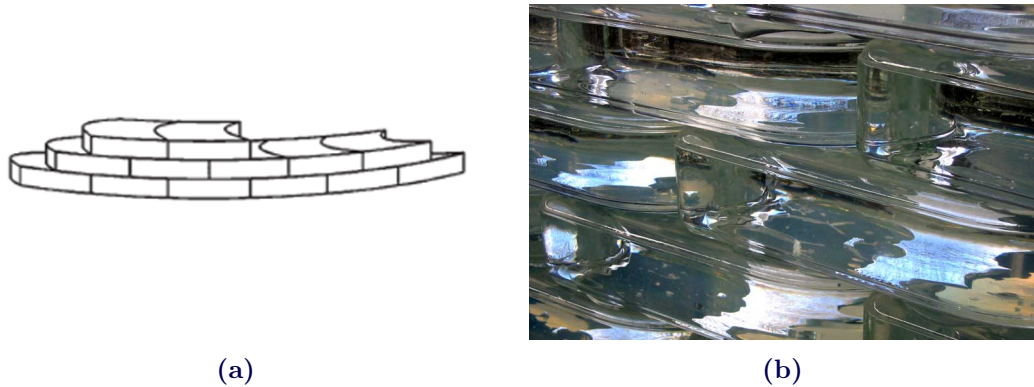


Figure 3.5: Atocha memorial; (a)Schematic representation of circular geometry due to brick-shape, taken from Oikonomopoulou et al. (2014); (b)Close up of the glass brick wall, taken from Lomholt (2014);

The monument consists of a glass cylinder connected to an underground presentation room. The inside of the glass cylinder, is covered by a transparent plastic film, in which quotes are engraved. They are illuminated by incident light at sunset and sunrise. The application of glass allows for this interesting display. This display can be experienced from the presentation room, as shown in Figure 3.6a. The outside appearance of the memorial is illustrated by Figure 3.6b. (Lomholt, 2014)

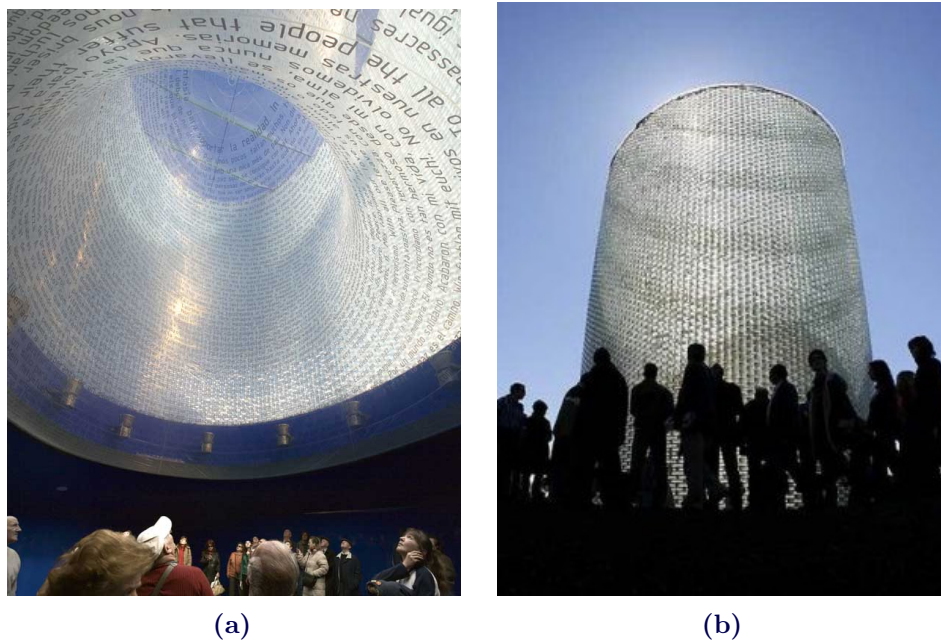


Figure 3.6: Atocha memorial, taken from Lomholt (2014); (a)Interior appearance; (b)Exterior appearance of the memorial;

3.3.4 Crystal House, Amsterdam 2016

The Crystal House is a recently realized innovative glass brick facade. This 10m high facade has a chic appearance, while being consistent with the (non-transparent) masonry structure of the surrounding 19th century buildings, as shown in Figure 3.7a. The Crystal House uses a transparent UV-modified acrylate, to join the glass bricks. In this case, the facade needed to be flat in order to match the appearance of its surrounding. To obtain a geometry that resists the lateral forces and buckling modes, four buttresses are applied. In Figure 3.7b one of those buttresses can be observed.



(a)



(b)

Figure 3.7: Crystal Houses; (a)Impression; (b)Buttress providing lateral stability;

The glass facade supports its own weight. The second floor of the building is supported by a different support system, as is indicated in Figure 3.8.



Figure 3.8: Crystal Houses; (a) Impression, taken from mvr.dv.nl; (b) Structural scheme;

As mentioned, a transparent UV-modified acrylate is used. This adhesive is photocatalytically cured. The qualitative representation of the strength of the adhesive, depending on the thickness, is illustrated in Figure 3.9. A thickness of 0.1-0.3mm corresponds to the optimal strength of the adhesive. The strength of the adhesive is significantly reduced outside these boundaries. Therefore, a high precision is required, also for the glass bricks. The tolerance for the bricks is therefore set to $\pm 0.25\text{mm}$ for both the flatness and the dimensions. The adhesive was only applied horizontally. Vertical application was inconvenient, because the adhesive would flow downwards before curing could be realized. This is due to the low viscosity of the adhesive. (Oikonomopoulou et al., 2014)

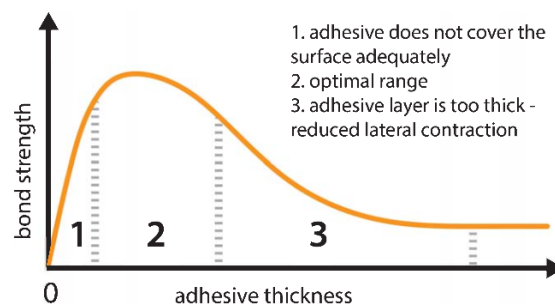


Figure 3.9: Adhesive shear strength as a function of the thickness, taken from Oikonomopoulou et al. (2014);

3.4 Evaluation

The different structural concepts of the references discussed in this chapter, can be compared by looking at the three key factors, described in Section 3.2. For each of the reference projects, the applied solutions are given in Table 3.1. Note that the first two references handle lateral loads and buckling modes in a different way (i.e. by the steel structure). Since the stability is not achieved by the geometry of the glass bricks in this case, it is not included in the table.

Table 3.1: Solutions for the key factors that determine the structural performance;

Reference project	Brick type	Joint type	Geometry
Maison Hermes	Hollow	Metal frame	-
Optical House	Solid	Pre-stressed elements	-
Atocha memorial	Solid	Transparent adhesive	Cylindrical shape
Crystal House	Solid	Transparent adhesive	Buttresses

The different solutions that are applied in the references, are a result of the different aesthetic and structural requirements. Generally speaking, the most transparent result can be obtained by application of solid bricks in combination with a transparent adhesive.

4 Arched Masonry

4.1 Introduction

For a bridge design, several support systems can be considered. A choice is made based on the span, the loads and several other consideration. The most frequently applied systems are schematically illustrated in Figure 4.1. It is shown whether components are in tension or in compression. Glass is able to resist relatively high compression stresses, compared to the flaw reduced tensile stresses (Chapter 5). Application of glass as a compression member is therefore a more efficient way to use the material. As a result, an arch is deemed to be a suitable support system. Due to its shape, the loads are mainly transferred as axial compression forces.

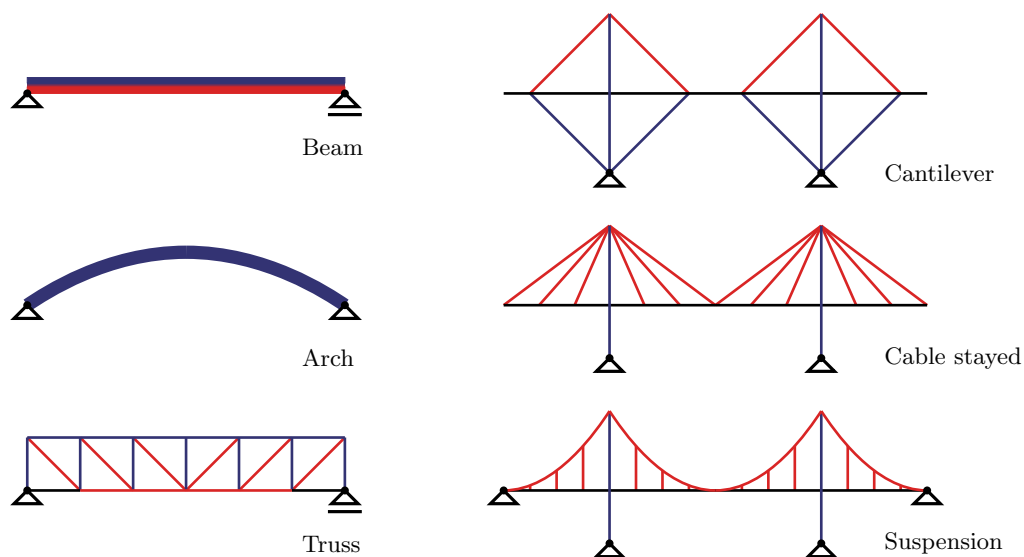


Figure 4.1: Schematic representation of several support systems; Red=tension, Blue=compression;

In order to establish the safety of a glass arched masonry bridge, it is desired to obtain a better understanding of its behavior. To achieve this, Section 4.2 elaborates upon the behavior of arched support systems *in general*. The concept of a line of thrust is explained and some ideal shapes are derived. In Section 4.3 *masonry* arched support systems are discussed. It will be shown which structural criteria are relevant. A theory is provided which may be used to assess the stability of a masonry structure. Section 4.4 concludes the chapter with an elastic method, in which the response of an arched structure is computed using differential equations.

4.2 Arched support system

Arches are a curved line support system. Convex arches mainly transfer downward loads as axial compression forces. In contrast to cables, arches also have a bending- and shear stiffness. Depending on the load configuration, internal moments and shear forces may occur. Nevertheless, those internal moments and shear forces remain rather small compared to those that would occur in a beam-system. (Welleman, 2012)

4.2.1 Line of thrust

For an arched support system, the *ideal shape* is considered to be the shape for which only axial (compression) forces occur. This is dependent on the load configuration that is regarded. For different configurations, the ideal shape is different. In 1675, Robert Hooke published an anagram that stated the following:

“
As hangs the flexible line, so but inverted will stand the rigid arch
”

Since a flexible line (i.e. cable) does not have any bending resistance, its shape will adapt in such a way that the loads are transferred as axial forces only. When the shape of the cable is inverted, the axial *tension* force becomes an axial *compression* force. This principle is illustrated in Figure 4.2.

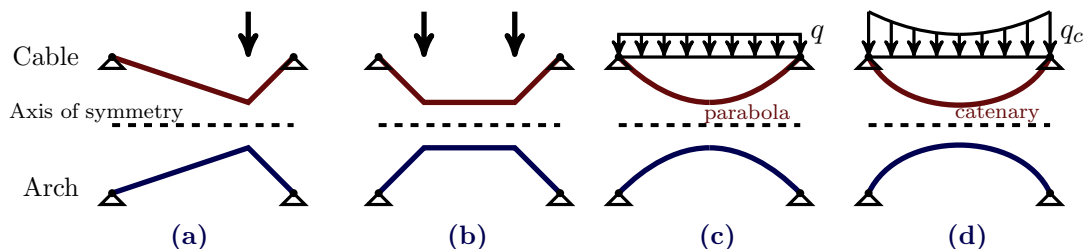


Figure 4.2: Ideal arch shape, obtained by inverting the shape of a cable under a particular load configuration;

In fact this shape represents the *line of thrust* of an arch. In every cross section, the distribution of stresses can be represented by a resultant force. The location of this resultant, is represented by the line of thrust. Independent of the geometric shape of the arch, the shape of the line of thrust remains the same. For the ideal shape, only axial compression forces occur, meaning that the stresses are equally distributed. In practice arches are not always loaded in the most advantageous way, e.g. a bridge that is asymmetrically loaded by a crowd present at one side only. In that case the line of thrust has a certain eccentricity with respect to the centroidal axis of the arch. This will result in internal moments with different stress distributions as a result. Nevertheless, if the line of thrust remains within the *middle third* of a rectangular cross section, no tensile stresses will occur. This principle is illustrated in Figure 4.3.

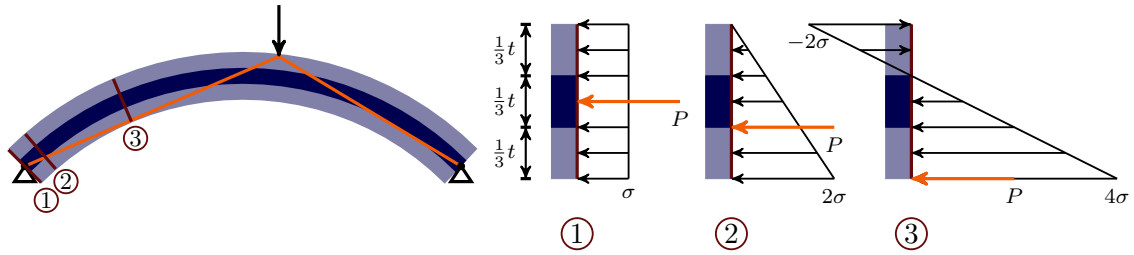


Figure 4.3: Stress distribution due to an eccentric line of thrust, based on Hoogenboom (2014);

4.2.2 Parabolic shape

According to Figure 4.2c, the ideal shape of an arch under a horizontally distributed load is a parabola. Welleman (2012), proved that this is indeed the ideal shape, by regarding the cable in Figure 4.4. For this cable, the following differential equation can be derived:

$$H \frac{d^2z}{dx^2} = -q \tag{4.1}$$

The derivation of (4.1) can be found in Appendix C.4. Integration and application of the boundary conditions ($z(0) = 0$ and $z(l) = 0$) provides the following function for the cable's position:

$$z(x) = -\frac{q}{2H}x^2 + \frac{ql}{2H}x \tag{4.2}$$

As function (4.2) shows, the position of the cable can be written as the general expression of a parabola:

$$z(x) = ax^2 + bx + c$$

Where in this case:

$$a = -\frac{q}{2H}; \quad b = \frac{ql}{2H} \quad \text{and} \quad c = 0$$

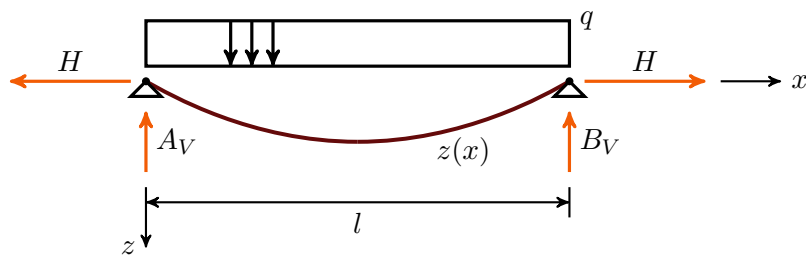


Figure 4.4: A cable loaded by a distributed load, based on Welleman (2012);

4.2.3 Catenary

In deriving the ideal parabolic shape, the load configuration was horizontally distributed. If a cable is merely loaded by its own weight, the configuration is somewhat different. In that case the load is distributed *along the curve*. The difference is illustrated in Figure 4.5.

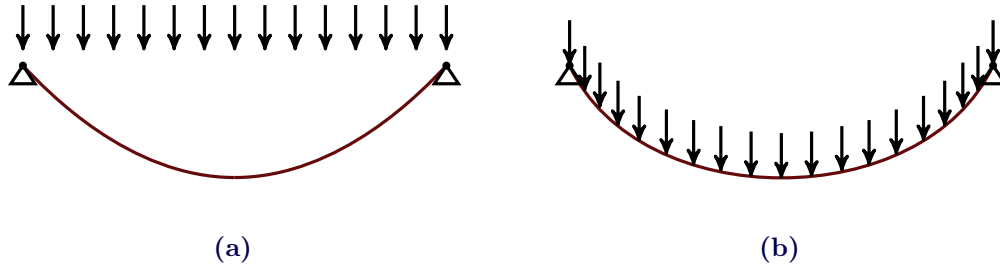


Figure 4.5: A cable piece loaded by a distributed load, based on Welleman (2012);
 (a)Horizontally distributed; (b)Distributed along the cable;

If a load distributed along the curve is now projected on a horizontal axis, the following equation holds:

$$q(x) = q_c \cdot \frac{dL}{dx} \quad (4.3)$$

In this equation, q_c is the weight of the cable per unit of length and L represents the length of the curve. It can be observed that a bigger slope results in a bigger load. The length of a certain interval dx , can be obtained using the general expression for the length of a curve:

$$L = \int_x \sqrt{1 + (z')^2} dx \quad (4.4)$$

Substitution of (4.4) in (4.3) provides:

$$q(x) = q_c \cdot \sqrt{1 + (z')^2} \quad (4.5)$$

This expression can now be used to adjust the load configuration in the differential equation of a cable. Substitution of (4.5) in (4.1) provides:

$$H \frac{d^2 z}{dx^2} = -q_c \cdot \sqrt{1 + (z')^2} \quad (4.6)$$

From (4.6) an expression for the position of the cable under its own weight can be derived:

$$z(x) = -\frac{H}{q_c} \cosh \left(-\frac{q_c x}{H} + C_1 \right) + C_2 \quad (4.7)$$

The shape that equation (4.7) describes is referred to as a *catenary*.

4.2.4 Approximation of the catenary

For low rise-span ratios, the arch is rather flat (i.e. everywhere along the span, the slope is approaching a horizontal line). As a result, $\frac{dL}{dx}$ in equation (4.3) approaches the value 1. This means that a horizontally distributed load configuration is now approached. This is rather convenient, since it means that a horizontal distribution accurately approximates reality. As a result, the much more simple previously found parabolic expression may be used:

$$z(x) = \frac{l}{H} \left(-\frac{1}{2} q x^2 + C_1 x + C_2 \right)$$

Application of this approximation may result in easier and/or faster computations. Due to the simplification it may also be easier to interpret the results.

4.3 Masonry arches

4.3.1 Structural criteria

Structures in general must satisfy a (large) number of criteria. The three main criteria relevant for establishing the structural safety of a design, are those of:

- Strength
- Stiffness
- Stability

The structure must be strong enough to withstand the loads that are imposed. Furthermore, it must not deflect excessively and it must not develop large unstable displacements. If those three criteria can be satisfied, the next step is to check the criteria regarding the serviceability of the structure. (Heyman, 1995)

When analyzing the structural capacity of a masonry arch, the following assumptions are made:

- Masonry has an infinite compression strength
- Masonry has no tensile strength
- Sliding failure does not occur

In a masonry design, the basis of design is to keep the stresses relatively low. The strength is between 10 and 30 times bigger than the average stresses. Therefore the *strength* criteria is usually met. However, stress concentrations may arise. They may eventually lead to splitting of the material. If this local failure will not result in global failure, the structure will still be safe. Sliding failure rarely occurs in masonry structures, but occasionally precaution must be taken to avoid slip. The structure's *stiffness* is deemed to be sufficient, since masonry-designs are relatively non-slender and stone is a relatively stiff material. (Heyman, 1995)

The final criteria, that of *stability*, is usually governing. Arches in general may buckle, as illustrated in Figure 4.6a. For flat arches, the buckling length corresponds to half of the span, as derived by Welleman (2012). As the load increases towards the critical load and initial imperfections are taken into account, large unstable displacements are developed, as illustrated in Figure 4.6b.

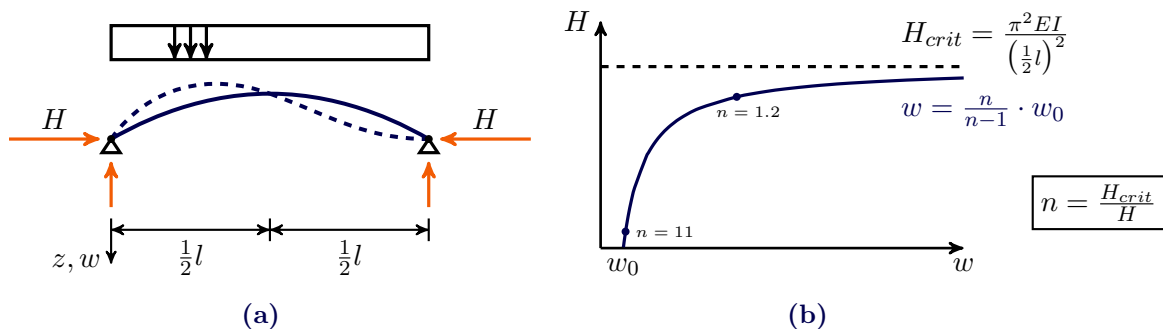


Figure 4.6: Buckling of an arch; (a) Buckling mode; (b) Large displacements as critical load is approached, based on Hartsuijker and Welleman (2007);

However, arched *masonry* structures are rather stiff and are typically designed such that the average stress is low. Therefore critical load is significantly larger than the working load, resulting in a low amplification factor $n/(n-1)$. Typically $n > 11$, meaning that the additional displacement is less than 10% of the original imperfection w_0 , as indicated in Figure 4.6b. Therefore the increased eccentricity resulting from additional deflections is usually disregarded when assessing the stability of a masonry structure.

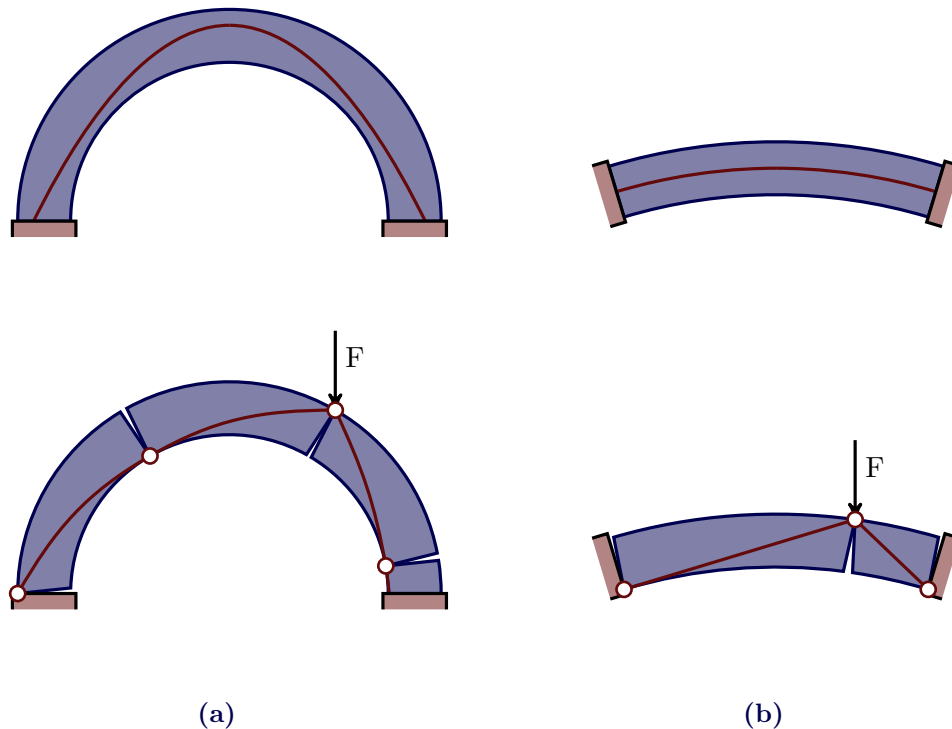


Figure 4.7: Formation of hinges in a circular arch (a) Instability by the formation of a four-hinge mechanism due to a point load, based on Heyman (1995); (b) Flat arch becoming a stable statically determined structure under a point load;

If in a section the eccentricity of the position of the line of thrust becomes sufficiently large, this will result in the formation of a hinge. Formation of sufficient hinges will lead to a *collapse mechanism*. The force F in Figure 4.7a, affects the position of the line of thrust. Eventually the line of thrust cannot be contained within the geometry. At the locations where the line of thrust reaches the arch's outer boundaries (i.e. the extrados and intrados), hinges will be formed. If sufficient hinges are formed, a collapse mechanism will arise. In some cases such a mechanism cannot be constructed. For the flat arch shown in Figure 4.7b, it is not possible to form the four-hinge collapse-mechanism. Failure will only happen if the loads are increased to such an extent that the material crushes. These 'flat arches' may also fail due to the occurrence of a snap-through mechanism, which is illustrated in Figure 4.8. This snap-through mechanism may occur due to settlements of the supports, axial shortening of the arch under compression or thermal shrinking. (Heyman, 1995) (Oschendorf, 2002)

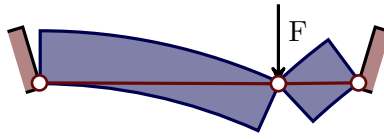


Figure 4.8: Snap through mechanism that may occur in flat arches, due to sufficiently large support settlements or axial deformation, based on Oschendorf (2002);

4.3.2 Elastic and plastic approach

If the line of trust of a masonry structure remains within the intrados and extrados, a collapse mechanism will not occur. By determining the position of the line of trust, one can determine whether the structure is stable. Attempting to find the position of this line of trust, is in fact an elastic approach. Masonry arches are generally *hyperstatic* structures (i.e. statically indeterminate). Therefore the line of trust cannot be obtained by the static equilibrium equations only. An additional requirement can be formulated by allowing slight deformations. This type of analysis is elaborated upon in Section 4.4. Through this analysis, the position of the line of trust is obtained. However, the result of this analysis is extremely sensitive to very small imposed displacements at the location of the supports (i.e. displacements less than 5% of the thickness). Since very small imposed displacements will always occur and cannot be accurately estimated, it is impossible to determine the ‘actual’ position of the line of trust. (Heyman, 1995)

For structures in general it is true that practical imperfections lead to an unpredictable working state. For this reason a new philosophy arose, that does not regard the actual state of a structure, but analysis the collapse mechanisms of a structure. Two structures that are visually identical, may be in a very different working state due to small imperfections. However, if those structures are loaded slowly until they collapse, the same collapse loads will be found. This plastic analysis is applicable to any ductile material. Although stone or glass is not ductile in itself, it may be regarded as ductile when applied as masonry. The ductile response is a result of cracks that may slowly develop *inbetween* the bricks. They allow for plastic hinges to be developed, analogous to the formation of plastic hinges in steel frames. In order to establish the failure mechanism, the loads are increased by a hypothetical factor. Since the loads will be smaller in reality, the structures safety is established. (Heyman, 1995)

4.3.3 Safety

The master safe theorem

When regarding a masonry structure elastically, one attempts to compute the *actual* equilibrium state of the structure. A plastic approach on the other hand, regards a *hypothetical* equilibrium state at the boundary of collapse. Due to the hyperstatic nature of the structure, in reality there are infinitely many possible equilibrium states. In order to establish whether a masonry arch is sufficiently stable, both approaches apply the master safe theorem of plasticity. A formulation of this theorem that holds for masonry, is provided by Theorem 4.1.

Theorem 4.1 — The master safe theorem

If any position for the *line of thrust* can be found that lies *within the boundaries* of the masonry, then this is absolute proof that the structure is *stable* and collapse can never occur under the given loading.

After taking the imposed displacements into consideration, the master safe theorem still holds. The small imposed support displacements mentioned in subsection 4.3.2, barely affect the geometry of the arch. So if a position of the line of thrust can be found within the boundaries of the arch's geometry, this will still be possible in the deformed state. Therefore this state will have practically the same margin of safety as in the ideal situation. So although small imposed displacements may cause large shifts in the position of the actual line of thrust, it will never result into a collapse mechanism. (Heyman, 1995)

Geometrical factor of safety

The master safe theorem states that the structure is stable if a line of thrust can be found that lies within the boundaries of the masonry. However, it does not provide the margin of safety of the structure (i.e. if the structure will still be stable if there are slight imperfections). In order to assess the margin of safety, the geometrical factor of safety is introduced. As illustrated in Figure 4.9, there is a minimal thickness for which the line of thrust can be contained within the arch. For this minimal arch, only one position for the line of thrust can be constructed. The structure is now at the boundary of collapse and any slight imperfection will cause collapse. In order to increase the safety, the thickness of the arch is increased. The geometrical safety factor represents the ratio between the actual thickness of the arch and the minimal thickness. For a ratio of 3, the line of thrust can be contained within the middle third. In practice, a geometrical factor of 2 is sufficient to account for construction imperfections, slight settlements and accidental superimposed loading (i.e. temperature loads). Note that for explanatory reasons the self-weight is neglected for the construction of the line of thrust in Figure 4.9. (Heyman, 1995)

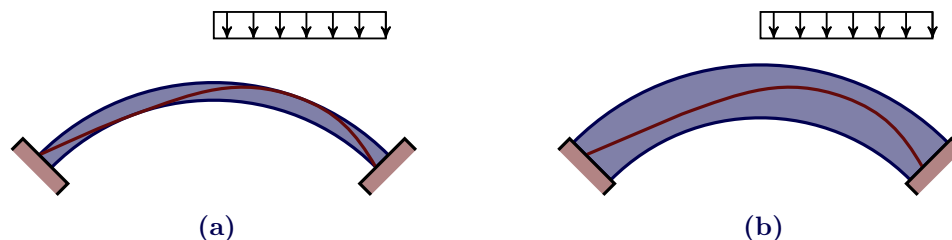


Figure 4.9: Application of a geometrical factor of safety, based on Heyman (1995); (a) Minimal arch with a safety factor of 1; (b) Arch with safety factor 3;

4.3.4 Construction

Only when a masonry arch is completely finished and constrained at its ends, it is able to function as a curved line support system. Therefore a temporary support system is necessary during construction. After placement of the keystone the arch is completed and the temporary support may be removed. Stresses due to the self-weight are introduced during this process. As a result, there may be a slight axial shortening of the arch and some small imposed displacements at the location of the supports. Tolerances between the bricks may also result in axial shortening. Thus, the geometry of the arch will never correspond

exactly to the geometry implied by the supports. The arch will now accommodate itself by the formation of hinges as illustrated in Figure 4.10. These hinges will not result in a collapse mechanism, but are merely a stable statically determined arch. Even when the arch is fitted more accurately, formation of these hinges is inevitable, although they may not be observable. (Heyman, 1995)

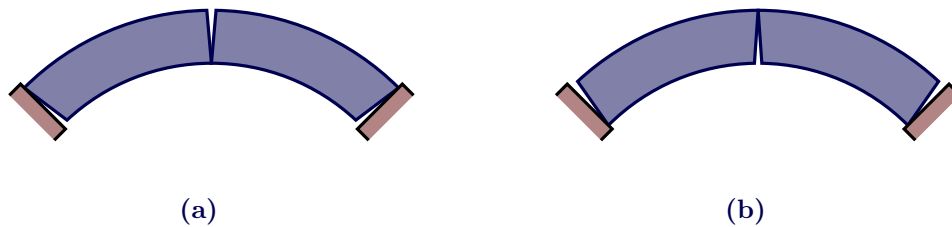


Figure 4.10: Inevitable imperfect fit of masonry arches, based on Heyman (1995);

The described formation of hinges does not affect the stability of the arch and therefore usually no additional measurements are taken to prevent them. A better fit would however result in a smaller crack depth, with lower maximum stresses as a result. One strategy to realize a better fit is by compensating the expected settlements by constructing an overreaching arch, as illustrated in Figure 4.11a. Another method to compensate the settlements is by horizontally jacking the arch as illustrated in Figure 4.11b. This last strategy has the advantage that it does not depend on the expected settlements, but may be adjusted according to the actual occurring settlements.

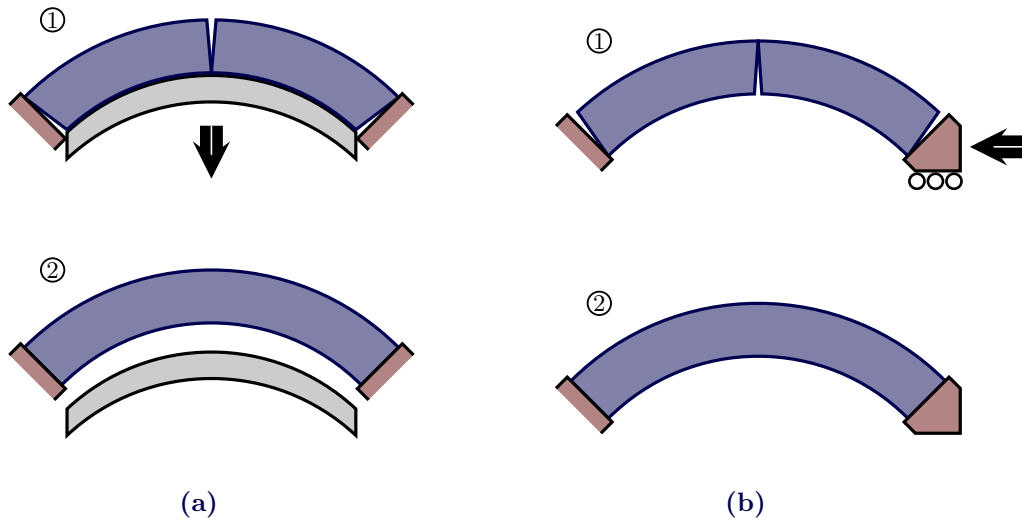


Figure 4.11: Construction methods to reduce crack depth caused by imperfect fit; (a)Overreaching arch; (b)Jacking;

4.4 Differential equation method (Elastic approach)

An elastic analysis of the behavior of an arch, may be done by formulating a differential equation for the system. This equation can then be used to compute the deflections, the internal forces and the position of the line of thrust. This section, which is based on Welleman (2012), will show how the position of the line of thrust can be obtained using the differential equation for an arch. It can be stated that an arch behaves similar to a cable, since it mainly transfers axial forces. As was mentioned earlier, in contrast to cables, arches also have a bending- and a shear stiffness. The deflections due to shear are usually rather small compared to the deflections due to bending. Therefore the deflections due to shear are neglected. It then follows that an arch may be modeled as a combined system of an Euler bending beam and an inverted cable. The cable part includes the axial force transfer as a result of the shape. ‘Inverted’, basically comes down to changing the sign. As a result, the axial tension forces become axial compression forces. The differential equation for the arch illustrated in Figure 4.12 may be formulated as follows:

$$\underbrace{EI \frac{d^4 w}{dx^4}}_{\text{bending beam}} + \underbrace{H \frac{d^2 z}{dx^2}}_{\text{inversed cable}} = q(x) \quad (4.8)$$

In this equation, the location function z describes the geometry of the arch and follows from the design. An efficient design applies the ideal shape. However, since the ideal shape of the arch depends on the applied loads, it can not be ideal for every scenario. Therefore, the arch will partially function as a beam and no longer transfer the loads as axial forces only.

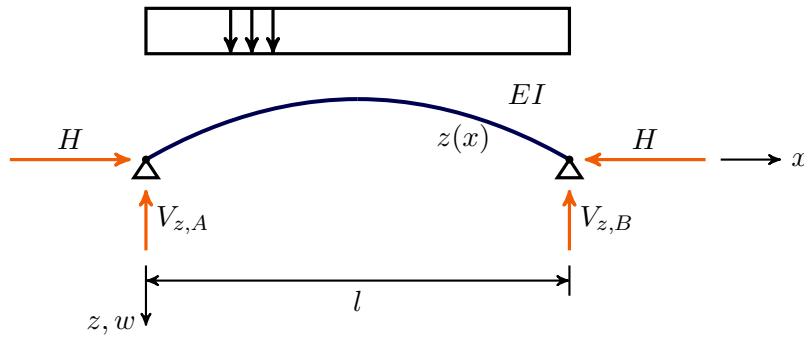


Figure 4.12: Schematic drawing of an arched support system, taken from Welleman (2012);

As an example, a parabolic shape is now regarded. This shape would be ideal in case of a horizontally distributed load. It has the following location function:

$$z(x) = -\frac{4fx(l-x)}{l^2} \quad (4.9)$$

After substitution of (4.9) in (4.8) and four times integration of the result, the deflection w is found:

$$w(x) = \frac{1}{24EI} \left(q - \frac{8Hf}{l^2} \right) x^4 + \frac{1}{6} C_1 \cdot x^3 + \frac{1}{2} C_2 \cdot x^2 + C_3 \cdot x + C_4$$

Four boundary conditions have to be applied, to obtain the integration constants C_1 , C_2 , C_3 and C_4 . At the location of the supports, there is no deflection. In case of *hinged supports*, the moment may be set to zero. Therefore, the following boundary conditions may be formulated:

$$\begin{aligned} x = 0 & \quad \rightarrow \quad w = 0; & \quad M = 0; \\ x = l & \quad \rightarrow \quad w = 0; & \quad M = 0; \end{aligned}$$

In order to apply these boundary conditions, the definitions of the rotation and the moment are introduced:

$$\begin{aligned} M(x) &= -EI \frac{d\phi}{dx} \\ \phi(x) &= \frac{dw}{dx} \end{aligned}$$

With these definitions the boundary conditions can be applied and the integration constants can be solved. The only unknown that remains, is the horizontal support reaction H . It is unknown since the system is statically undetermined. In order to solve H , an additional requirement is formulated. In order to do so, a horizontal displacement is allowed at one of the supports (i.e. it is turned into a roller support). As a result the system is now statically determined. According to Welleman (2012), the horizontal displacement at the support may be expressed as follows:

$$u(l) = \int_0^l -\frac{dz}{dx} \frac{dw}{dx} dx \quad (4.10)$$

This formula computes the horizontal displacement of the support under the given loads and support reactions. This displacement should be zero, since the support is not allowed to move in reality. This principle is illustrated in Figure 4.13. The equation for solving H can now be derived using (4.10):

$$\begin{aligned} u(l) &= \underbrace{\frac{qfl^3}{15EI}}_{u_q} - \underbrace{\frac{8f^2l}{15EI}H}_{u_H} = 0 \\ &\rightarrow H = \frac{ql^2}{8f} \end{aligned}$$

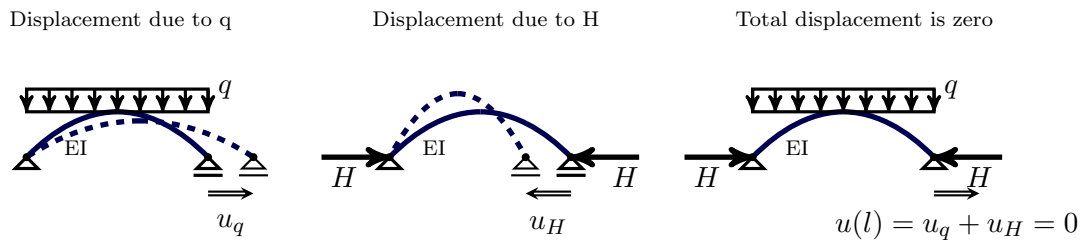


Figure 4.13: Additional requirement to solve the unknown horizontal support reaction;

At this point, all unknowns have been solved and the desired output (i.e. internal forces, stresses, position line of thrust etc.) may be derived. To compute the *vertical* component of the internal forces, the following expression may be used:

$$V_z(x) = -EI \frac{d^3w}{dx^3} - H \frac{dz}{dx}$$

This vertical component is different from the *shear force*, of which the direction is parallel to the cross section. The shear force and also the axial force may be derived from the horizontal and vertical forces:

$$\begin{aligned} V(x) &= H \sin \theta + V_z \cos \theta \\ P(x) &= -H \cos \theta + V_z \sin \theta \end{aligned}$$

Where θ is the angle between the centroidal axis and the horizontal (i.e. the slope of the arch):

$$\theta(x) = \arctan \frac{dz}{dx}$$

From these internal forces, the internal stresses may be derived. The highest stress occurs either in the top or bottom fiber.

$$\begin{aligned} \sigma_{top} &= -\frac{M \frac{1}{2}t}{I} + \frac{P}{A} \\ \sigma_{bottom} &= \frac{M \frac{1}{2}t}{I} + \frac{P}{A} \end{aligned}$$

The position of the line of thrust z_t , is determined using the eccentricity of this line relative to the centroidal axis:

$$\begin{aligned} e(x) &= \frac{M}{P} \\ z_t(x) &= z(x) + e(x) \end{aligned}$$

If the obtained position of the line of thrust lies within the middle third of the thickness, no tensile stresses will occur in any cross section perpendicular to the centroidal axis.



5 Structural Glass

5.1 Introduction

The main quality that makes glass such an appealing material, is that unlike many other materials it is transparent. Currently, there is a growing interest in transparent structures. Glass has a high compressive strength (i.e. it can be higher than concrete). This makes it possible to use glass in a structural way. This chapter provides a theoretical background of the material glass, to explain its behavior.

5.2 Material characteristics

5.2.1 Nanoscale structure

In order to put the material 'glass' in a larger perspective, materials in general are considered. Materials can be classified by distinguishing four categories. This commonly used classification, makes the following distinction according to Bourhis (2008):

metals: pure, alloyed with other metals or alloyed with non-metals

ceramics: ionic ceramics or covalent ceramics

polymers: organic chains ($-CH_2-$)

composites: combinations of the categories above

Ceramic materials are inorganic and can be either ionic or covalent. Ionic ceramics are a combination of metals and non-metals, e.g. $NaCl$, MgO , Al_2O_3 and TiN . Covalent ceramics are a combination of non-metals only, e.g. Si_3N_4 and SiO_2 . The distinction between these categories, is based on the different types of bonding. Generally the four bonding-types in Table 5.1 are distinguished.

Table 5.1: Bonding types and corresponding binding energy, based on Bourhis (2008);

Bond	Binding energy (kJ/mol)	
Ionic	600	- 1600
Covalent	500	- 1300
Metallic	100	- 840
Van der Waals	\leq	45

It can be observed that ionic bonding and covalent bonding show the highest bonding strengths. Those bond types are formed in ionic and covalent ceramics. Figure 5.1 illustrates the relation between the bonding types and material categories.

Glass is considered to be a ceramic material, since the bonds are either ionic or covalent. It has corresponding qualities, such as a high stiffness, an elevated yield stress and an elevated chemical resistance. It also has an elevated density. However, like ceramics, glass behaves

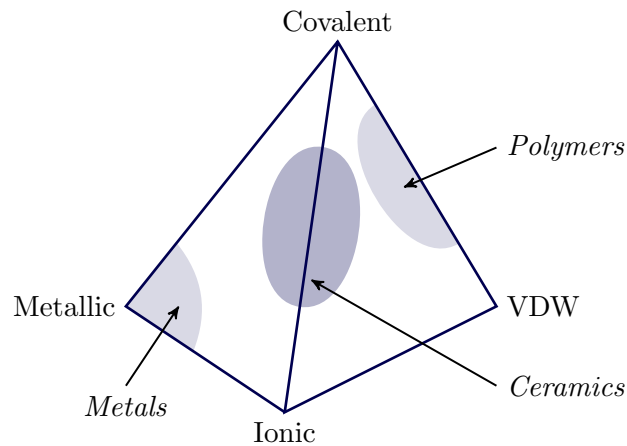


Figure 5.1: Schematic representation of relation between material categories and bond types, taken from Bourhis (2008);

brittle, has a low toughness and a low thermal shock resistance. Only small reversible deformations are possible. (Bourhis, 2008)

Glass is made by melting and annealing a mixture of silica sand (SiO_2), alkaline oxides and alkaline earth oxides (Schittich et al., 2014). The nano-structure of glass distinguishes itself from ionic and covalent ceramics. Glass presents a short-range order, where a long-range order is general. Since a long-range order is lacking, glass is considered to be an amorphous material. According to Louter (2011), glass turns into a frozen solid when it is cooled down over the glass transformation range. This is in contrast to metals, which form a lattice structure when cooled down from liquid to solid (crystallization). The difference is shown in Figure 5.2. This is why glass is considered to be a super-cooled liquid, rather than a solid.

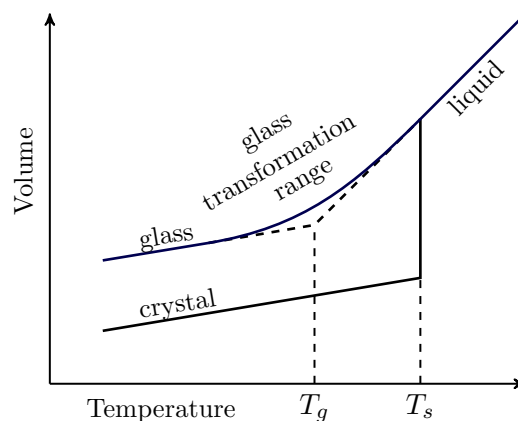


Figure 5.2: Glass its volume dependence on temperature, taken from Louter (2011); T_G =glass transition temperature; T_s =melting temperature;

According to Louter (2011), the irregular nano-structure of glass, presents a network of tetrahedral modules. Those modules contain one silicium atom and four oxide atoms, as illustrated in Figure 5.3. According to Veer (2007), the network can be characterized as

joined rings consisting of three to seven silicium atoms bridged by oxygen atoms. The connection within these rings is based on a covalent bond. Additives cause some of the covalent bonds to break and form an ionic bond instead, which decreases the melting point. In Figure 5.3 this is shown for soda-lime-silica glass.

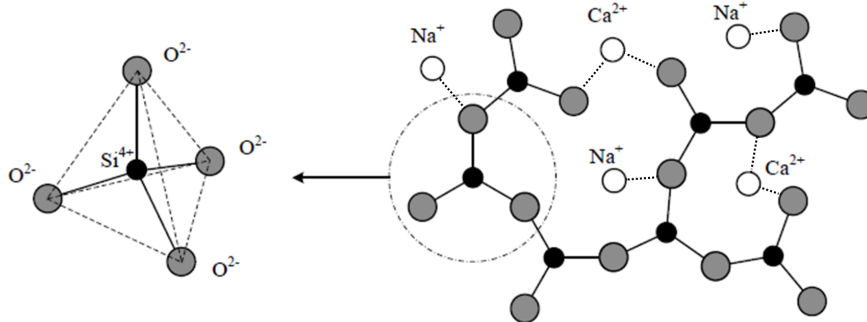


Figure 5.3: Amorphous molecular structure of glass, based on Louter (2011);

In order to improve the properties of glass for a certain application, there has been a lot of experimenting with its composition. For structural purposes, the most commonly used type of glass is soda-lime-silica glass. An alternative is borosilicate glass. The composition of both types is given in Table 5.2. The differences will be discussed in the next subsection.

Table 5.2: Chemical composition of soda-lime-silica glass and borosilicate glass, based on Schittich et al. (2014);

Substance	Formula	Soda-lime-silica glass	Borosilicate glass
		Portion [%]	Portion [%]
Silicon dioxide (silica)	SiO_2	69-74	70-87
Calcium oxide (lime)	CaO	5-12	
Sodium oxide (soda)	Na_2O	12-16	1-8
Boron oxide	B_2O_3		7-15
Magnesium oxide	MgO	0-6	
Aluminum oxide	Al_2O_3	0-3	1-8
Potassium oxide	K_2O		1-8

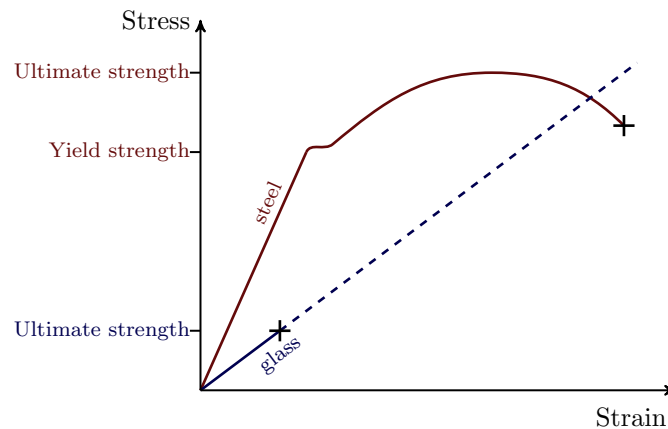
5.2.2 Properties

The properties of both soda-lime-silica glass and borosilicate glass, are given in Table 5.3. As was mentioned in the previous subsection, glass presents an elevated density and stiffness. It also presents an elevated yield strength. This strength however, is not incorporated in the table, since it is not merely a material property (see section 5.4). In comparison though, borosilicate presents a slightly lower strength (about $\sim 70-90\%$) compared to soda-lime silicate (Oikononopoulou et al., 2014). Thereby currently its costs can be 2-4 times higher. The advantage of borosilicate compared to soda-lime silicate glass however, is that it has a lower thermal expansion coefficient. It is therefore better resistant against thermal shock. It also results in significantly less shrinkage during cooling. Therefore the production results are more accurate, which could avoid expensive post-processing. However, according to Oikononopoulou et al. (2014), this advantage becomes superfluous when a higher accuracy of the final product is demanded. In that case cold-working is necessary regardless.

Table 5.3: Properties of soda-lime-silica glass and borosilicate glass, based on Schittich et al. (2014);

Property	Symbol	Unit	Soda-lime-silica glass	Borosilicate glass
Density	ρ	kg/m^3	2500	2200-2500
Hardness	$HK_{0.1/20}$	GPa	6	4.5-6
Modulus of elasticity	E	GPa	70	60-70
Poisson's ratio	ν	-	0.2	0.2
Thermal expansion coefficient	α	$10^{-6}K^{-1}$	9	Class 1: 3.1-4.0 Class 2: 4.1-5.0 Class 3: 5.1-6.0
Thermal conductivity	λ	$W/(mK)$	1	1

Glass fails in a brittle manner. It can only deform elastically or fracture. Metals, such as steel, are able to deform plastically due to movement of dislocation in a crystal lattice. Steel shows large plastic deformation after reaching the yield strength, before it finally fails. According to Veer (2007), glass is not able to deform plastically due to the lack of a crystal lattice. If the covalent bonding is broken, it cannot reform easily. A bond failure around a defect, will cause the local stresses to increase. This causes another bond failure, increasing the local stresses even further. The result is a completely broken glass element. The brittle behavior of glass compared to the ductile behavior of steel is illustrated in Figure 5.4. Due to this brittle failure, special care should be taken when designing glass structures.

**Figure 5.4:** Stress-strain curve, comparing glass to steel;

5.3 Production process

Glass was discovered many years ago and has been produced in several creative ways since (e.g. spinning and pulling). Nowadays, the float process is the primary production process. This production process is largely automated and continuous. For the production of glass bricks, a different method is used, called casting. This method is generally a batch process and has not been automated yet. This is because the bricks are custom made and therefore no standardized sizes are currently available. The float process and the casting process will be elaborated upon in this section.

5.3.1 Float glass

To produce float glass, the raw materials are melted in a furnace at a temperature of 1550°C. Float glass thanks its name to its production method. At a temperature of 1000°C, the melt is ‘floated’ onto a tin bath. This way of production provides a very flat and smooth surface at the ‘tin side’ of the glass. The other side is referred to as the ‘air side’. The thickness of the glass sheets is controlled by rollers, which are applied at the top of the glass. By adjusting the speed, the desired thickness can be obtained. A lower speed provides a thicker sheet and vice versa. The thicknesses are standardized and vary between 2mm and 25mm. After reaching a temperature of 600°C, the glass is annealed (i.e. slowly cooled down) in the annealing lehr to prevent residual stresses. The glass is inspected automatically for visual defects. The sides contain roller-tracks, which are cut off and recycled. A standard width of 3.21m remains. Due to limitations with respect to handling, the standard length of the sheet is 6m. Bigger sizes do exist, but are still quite rare and much more expensive. The float glass production process is illustrated in Figure 5.5. (Louter, 2011)

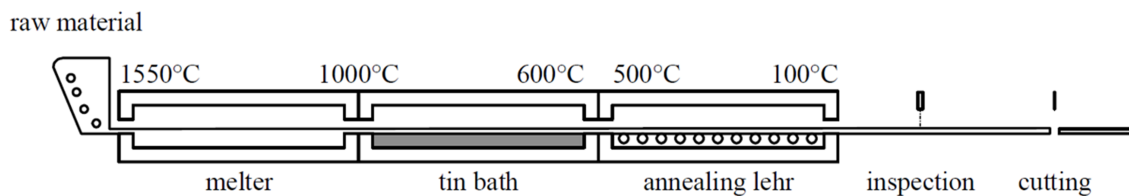


Figure 5.5: Schematic representation of the production process of float glass, taken from Louter (2011);

Cutting sheets of glass is usually done by applying an intentional line defect. The sheet is then bend, which usually results in breakage along the line defect. Another method is ‘waterjet cutting’, which can be used to make customized shapes. Since defects in the glass reduce the strength, the edges are treated afterwards. They can be polished, rounded or faceted.

5.3.2 Cast glass

There are no standardized glass bricks available yet for structural purposes. So far, casted bricks have been custom-made. Oikonomopoulou et al. (2014), describe the production process of cast glass bricks, used by ‘Poesia Company’ in Italy. The first step is producing a steel mold, coated with nickel. The coating provides a smooth surface and also makes it easier to release the form from the mold. The raw materials are heated to a temperature of about 1200°C. The liquid glass is then poured into the mold. This is illustrated in Figure 5.6a. The mold is then closed, as illustrated in Figure 5.6b. The glass needs to cool to about 700°C. After reaching this temperature, the brick is removed from the mold and placed in the oven to be annealed, therewith preventing residual stresses. The required annealing-time depends on the dimensions of the product. After production, the top surface is convex. If desired, it can be flattened using a CNC-machine.

The TU Delft has its own facilities to produce customized glass bricks. This allows for rapid prototyping, thereby improving a certain glass element design. In this production process, a mold is made from a mixture of crystalcast and water. Before casting the glass, the mold has to be heated slightly above the boiling point of water, until all water inside it



Figure 5.6: Cast glass production by Poesia Company, taken from Oikonomopoulou et al. (2014); (a)Casting molten glass into mold; (b)Closing the mold;

has evaporated. This step is crucial, since it is likely that the mold will break otherwise, due to the enclosed water which expands rapidly at higher temperatures.

Instead of melting raw materials, the glass lenses shown in Figure 5.7a are being re-melted. These lenses were damaged during the production process and are now recycled. They are made from ‘B270’-glass, because this type has good optical qualities. The molds are placed into the kiln, as illustrated in Figure 5.7b. The lenses are not put directly into the molds, because this might lead to inclusion of air bubbles. Instead, flower pots containing a hole in the bottom are positioned above the molds. The lenses are accommodated in the flower pots, after which the kiln is heated. After heating up to about 880°C, the highly viscous glass slowly pours out of the pot into the mold. After annealing, the cast object is obtained, as shown in Figure 5.7c.

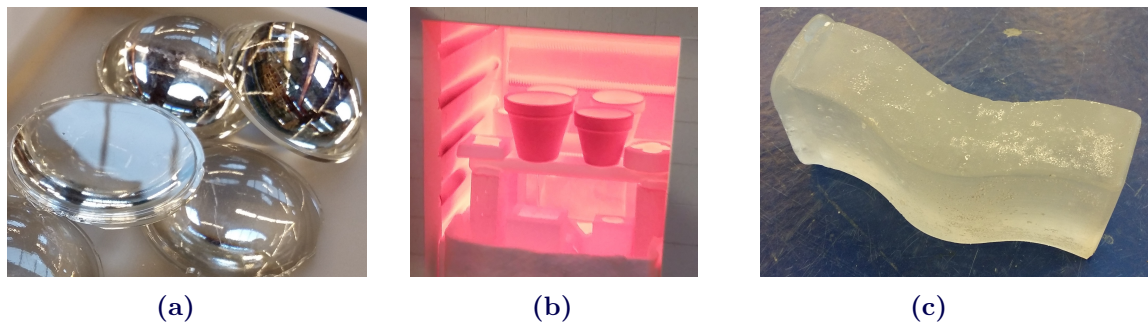


Figure 5.7: Cast glass production at TU Delft; (a)Lenses made of B270 glass; (b)Inside kiln; (c)Annealed glass brick;

5.4 Strength

It is hard to put a value on the strength of glass. According to Pepi (2014), the theoretical strength of glass might exceed 14,000MPa. This is based on the capacity of the strong covalent bonding between the silica and oxygen atoms. In practice however, this strength is highly reduced, as will be explained in this section.

5.4.1 Failure mode

The strength of glass is highly dependent on the presence of defects, located at the surface of the glass. High local stresses will arise around such defects. Since glass is not able to deform plastically, redistribution of the stresses is not possible. Bond breakage, will increase the local stresses around the defect causing more bonds to break. This is why a crack initiates from the defect, causing complete fracture of the glass element. This corresponds with failure mode I (i.e. an opening failure mode), as illustrated in Figure 5.8.

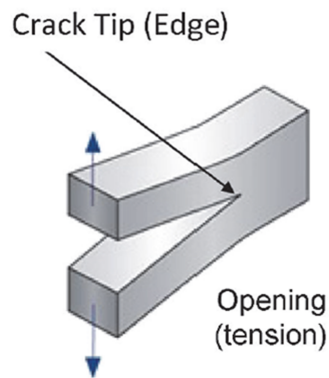


Figure 5.8: Mode I; Opening failure mode, taken from Pepi (2014);

In a sheet of glass, a moment causes tensile- as well as compressive stresses. The compressive strength of glass far exceeds the flaw reduced tensile strength (Pepi, 2014). Therefore in practice failure due to an exceeded compressive strength, does not occur. In a sheet of glass loaded in compression only, the strength is usually limited by buckling. Glass bricks are not slender and will therefore not necessarily buckle when loaded in compression. Their failure behavior is elaborated upon in Chapter 8.

Both the size and the shape of defects influence the strength. If the size of a defect is bigger, the strength of the glass is automatically lower. The flaws arise from the production method, as well as the handling afterwards. Once the glass is installed, new defects may still arise due to weathering (sand/wind) and human interaction (touching/scratching). For cast glass, the manufacturing process is a bit harder to control than that of float glass. Without post processing, there is an increased chance on the presence of defects, which causes a lower average strength.

5.4.2 Flaw size

As stated, the tensile strength is dependent on the flaw depth. Theoretical considerations of Haldimann et al. (2008), formulate the relationship illustrated in Figure 5.9. It can be observed that the size of the defects significantly affects the strength. Because the presence of flaws cannot be avoided, a certain level of flaw-depth must be accepted. This generally leads to a rather low design strength compared to the theoretical possibilities.

5.4.3 Flaw shape

Besides from the depth of the defect, also the shape is of importance. Usually three main types are distinguished, which are illustrated in Figure 5.10. The through crack or Griffith

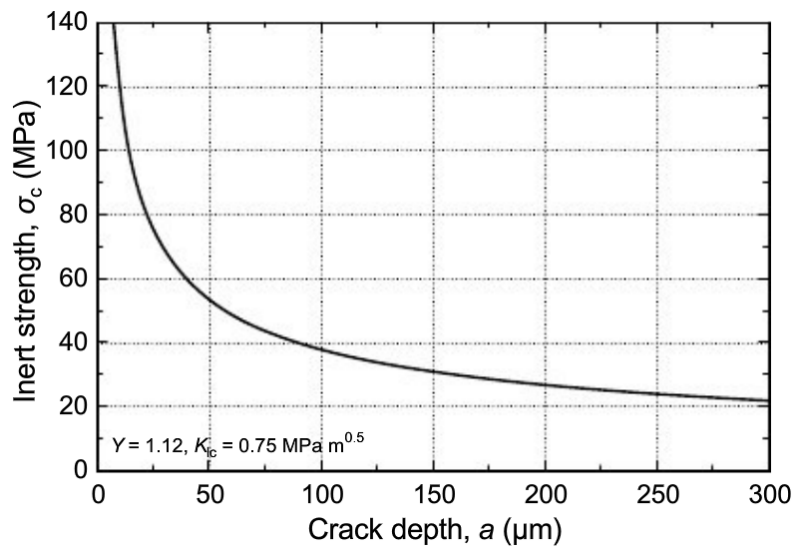


Figure 5.9: The dependence of the tensile strength of glass on the flaw depth, taken from Haldimann et al. (2008);

crack, is considered to be the worst one. It is a long and shallow flaw extending over the entire width of the piece. As a result, the b/c ratio is almost infinite. The second type is the less severe partial crack. In this case the crack does not cover the full width. The special case in which $b/c=1$ is called the penny shaped crack, and this type reduces the strength the least. Fortunately this type is the most common one at the surface. (Pepi, 2014)

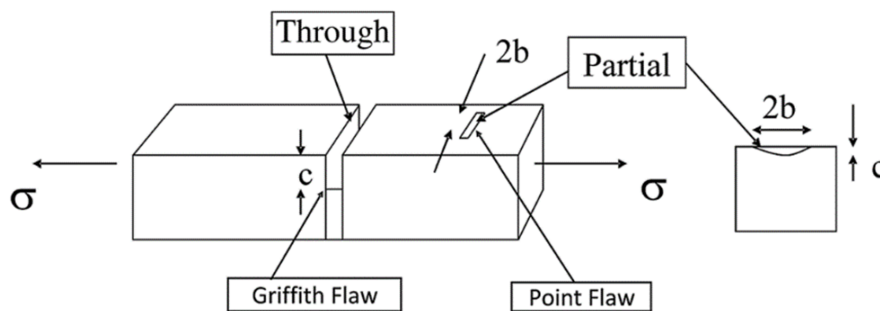


Figure 5.10: Flaw shapes, taken from Pepi (2014);

Shapes and sizes of defects are quite hard to measure. This applies especially on the depth of a defect. Therefore, the strength of a glass panel is usually obtained by performing (bending) tests. Since the presence of a (severe) defect is based on statistics, the size of a sheet is also relevant. A bigger sheet has an increased chance of containing a severe flaw. Therefore, on average, a bigger panel has a lower strength.

5.4.4 Static fatigue

Thus far the *short-term* tensile strength has been regarded. When located in a humid environment, the tensile strength of glass is time dependent. A phenomenon called 'static

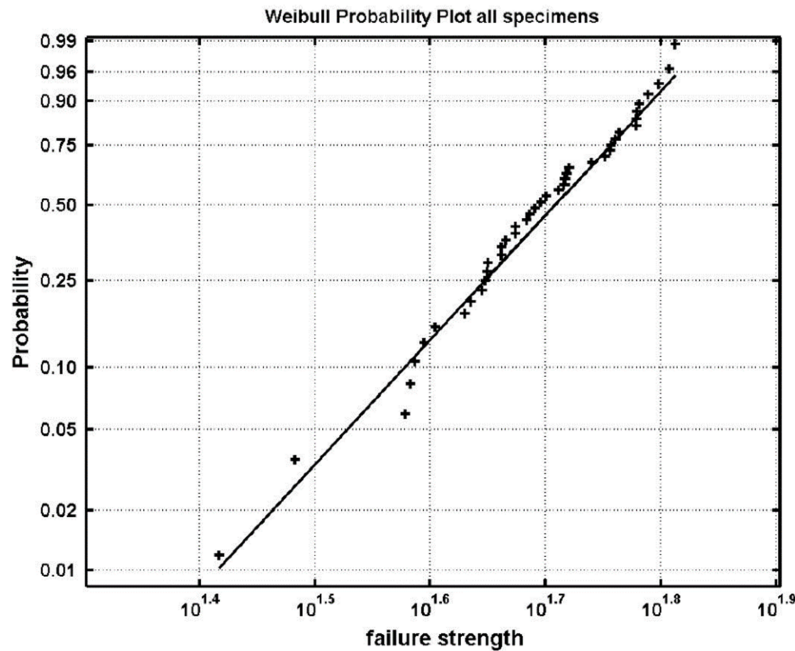


Figure 5.13: Weibull plot of bending tensile strength, taken from Veer (2007);

5.4.6 Design value strength

In order to be able to perform structural calculations for glass, a design strength needs to be formulated. The 'EN 572-1:2012', which is a part of the Eurocode, defines a characteristic bending strength of 45MPa. This value relates to a 5% probability of breakage at the lower limit of the 95% confidence interval. Higher characteristic bending strengths may be used if the glass is thermally treated.

5.4.7 Thermal treatment of the glass

In order to increase the strength of a glass pane, it can be thermally treated. The following types of glass can be distinguished, according to the treatment:

Annealed glass (AN): This is normal float glass. If the glass is cooled unequally, residual stresses will be present in the glass. To prevent these internal stresses, the glass is annealed (i.e. slowly cooled).

Heat-treated glass: This process is illustrated in Figure 5.14. The treatment is executed after the glass has been cut to its final size. In this case residual stresses are inserted intentionally. After cleaning, the glass is heated up to about 100°C above the glass transition temperature, which is about 620°C to 675°C. After heating, the glass is cooled rapidly, causing the outside of the glass sheet to cool faster than the core. Due to this differentiated cooling, the glass is pre-stressed. The outside of the glass is now in compression, while the inside is in tension. Failure of the glass occurs, when the local stresses around a defect exceed the tensile capacity. In case of heat-treated glass, the residual compression stress first has to be overcome. In this way a higher strength of the glass pane is obtained. (Louter, 2011)

Two types of heat-treated glass can be distinguished:

- heat-strengthened glass (HS)
- fully tempered glass (FT)

The difference lies within the cooling rate and therefore the amount of pre-stressing. Fully tempered glass is cooled faster and is therefore stronger. For heat strengthened glass a characteristic bending strength of 70MPa may be used. For fully tempered glass it is 120MPa. The strengths are summarized in Table 5.4. (Louter, 2011)

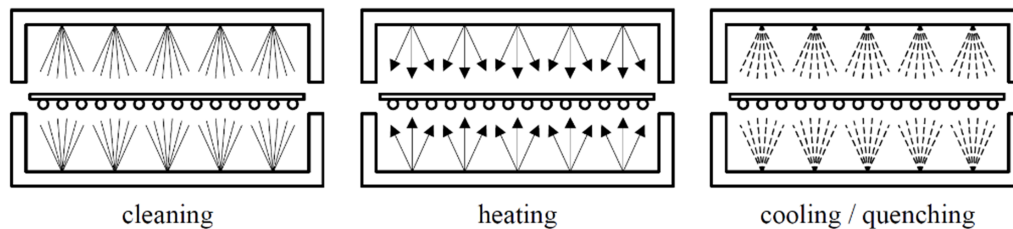


Figure 5.14: Heat treatment process, taken from Louter (2011);

Table 5.4: Glass strengths according to NEN 2608:2014;

Glass type	Tensile bending strength (MPa)
Annealed glass	45
Heat strengthened glass	70
Fully tempered glass	120

The pre-stressing does not only influence the strength, but also the breaking pattern of the glass, as shown in Figure 5.15. Because fully tempered glass is highly pre-stressed, a lot of energy is released when it breaks. Due to this energy release, the breaking pattern shows fragmentation into a lot of small pieces. Annealed glass does not contain any pre-stress, so the breaking pattern is less fragmented. The crack only propagates along a few lines. The pre-stressing in heat-strengthened glass, is lower than in fully tempered glass and therefore shows a crack pattern that lies somewhat in-between. (Louter, 2011)

5.4.8 Laminated glass

Laminated glass consists of multiple glass panes that are bonded by an interlayer. Most commonly this interlayer is an adhesive foil. The foil is positioned between the panes, after which heat and pressure are applied by an autoclave. The purpose of the interlayer is to keep the glass fragments in place after failure. This prevents human injury and can also provide residual strength after breaking. The glass type that is used in the laminated element, relates to the amount of residual strength. When annealed glass panes are broken, large pieces of glass remain. The broken pieces overlap one-another and are connected by the interlayer, providing some residual capacity. Fully tempered glass shows large fragmentation, and will therefore have a lower residual capacity.

The residual capacity also depends on the interlayer that is used. The most commonly applied foils are PVB (polyvinyl butyral), EVA (Ethyl Vinyl Acetate) or SG (SentryGlas®). SG provides enhanced strength and stiffness. It is designed to resist vandalism and burglary. (Louter, 2011)

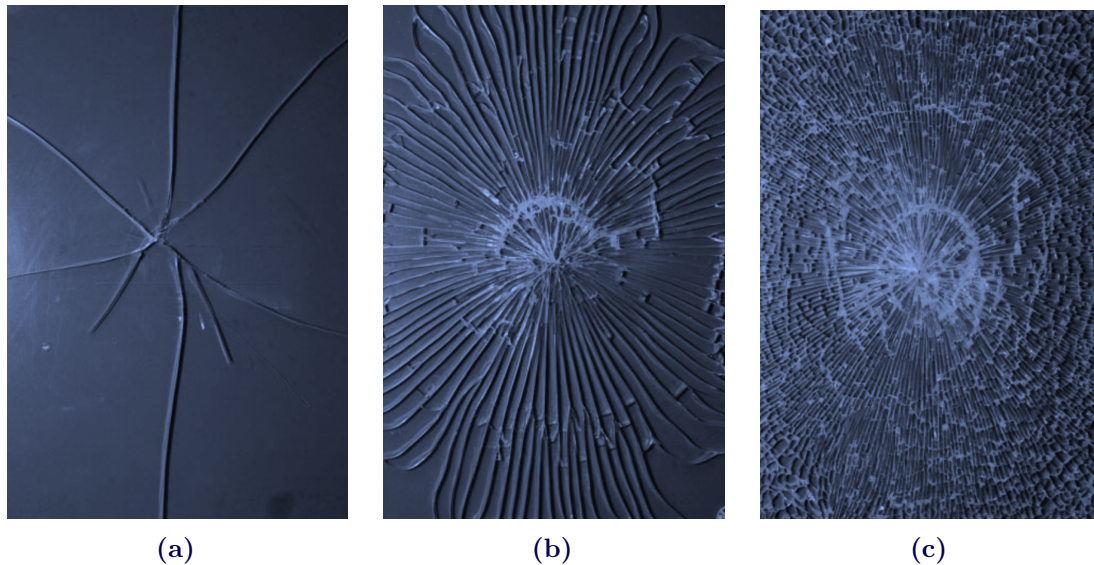


Figure 5.15: Fracture patterns of glass, depending on treatment, taken from Louter (2011); (a) Annealed glass; (b) Heat-strengthened glass; (c) Fully tempered glass;

5.5 Safety and design

Due to its brittle failure, glass is regarded as an unsafe building material. It breaks suddenly and it breaks completely. After thoughtful considerations however, glass can be applied in a safe way. The different structural design approach of glass compared to other building materials will be discussed in this section. This difference is perfectly outlined by the following statement:

“

Much more than common structural materials like steel and reinforced concrete, glass is highly susceptible to a wide range of incidents causing glass breakage. Hence the question should not just be ‘when will the glass break’ (probabilistic approach) but also ‘what will happen when it does?’ (consequence-based approach)

(Bos, 2007)

”

5.5.1 Risk

A structure is considered safe, when it is unlikely that it will cause injury or serious damage. Safety can be quantified by ‘risk’. Usually, risk is defined as an expected value and can be calculated by the following formula:

$$\text{Risk} = \text{Probability} \times \text{Consequence}$$

So the risk depends on the *probability* that an undesired event will occur, as well as the *consequence* of that event. Since it is not possible to design a structure without any risk, a certain level of risk is accepted. The acceptable level can be determined in several ways, but

for structures it is usually based on predetermined safety standards. The safety standards are usually composed by regarding the loss of life. If the risk of a structure is bigger than allowed by the standards, measures can be taken in order to fulfill those standards. The risk can be minimized by decreasing the probability and/or the consequence.

5.5.2 Design methods

A few design methods will be discussed here, outlined by Schittich et al. (2014). The ‘permissible stress design’-method and the ‘design according to the probability of failure’-method, are both based on a probabilistic approach. The ‘limit state design’-method includes a probabilistic approach, as well as a consequence-based approach. This is necessary for a safe design in glass.

Permissible stress design: In this method, the governing load is checked against the maximum permissible stress. The governing load is determined by calculation of dead, snow, wind or imposed loads. In order to deal with uncertainties, high safety factors are applied to guarantee a sufficient level of safety. This method is rather simple, so can provide fast results.

Design according to the probability of failure: In this method the usable strength is determined by describing the statistical nature of it. For glass, this is done by applying fracture mechanics. Also the duration of the load is considered. This method is far more accurate than the previous one, but obviously way more complex. For components that are commonly used, the calculation could be standardized by making design tables.

Limit state design: This method considers both the statistical nature of the material strength, as well as the statistical nature of the loading. This means that both the *probability* that a load case occurs and its *duration* are taken into account. Various failure modes are checked. This is done for both the ultimate limit state, as well as the serviceability limit state.

Furthermore, the consequences of single-component failure are investigated. This aspect is necessary for a safe design in glass. For structures of steel, timber or reinforced concrete, failing of a single component is not allowed. This makes it superfluous to analyze what would happen if it does. For glass, single-component failure can be caused by rather simple incidents. Therefore this failure is allowed as long as it does not lead to dangerous situations, such as people falling through. In addition, the safety of the global structure may not be compromised.

The most important part of the design calculation, is the determination of the safety concept. This concept shows which consequences might occur and how they will be handled. Varying strategies may be used to handle the possible consequences, e.g. laminating and providing alternative load paths.

5.5.3 Computing deformations and stresses

Glass behaves elastically and does not show any plastic deformations. Therefore the first-order theory, in which the response is assumed to be linear, is most common when calculating the stresses due to external loads. A more accurate result is obtained from second-order theory, which takes into account the geometric non-linear behavior. An example of non-linear behavior, is a plane that transfers membrane-stresses *after* a certain

deformation. Although second order calculations might be more accurate, the first order calculations are easier to execute and can provide conservative results.

The situations at locations where loads are transferred or introduced, can become quite complex. This is why manual calculations can become rather impossible. Fortunately, there are finite-element methods available, which can help performing these calculations. They are custom when examining stresses in glass. According to Schittich et al. (2014), it is important to keep in mind the following aspects:

- Areas where stresses are concentrated require careful modeling
- Load transfers can only be realistically modeled by using resilient interlayers

An example of a project where FEM is applied, is the Crystal Houses (discussed in Section 3.3), as shown in Figure 5.16.

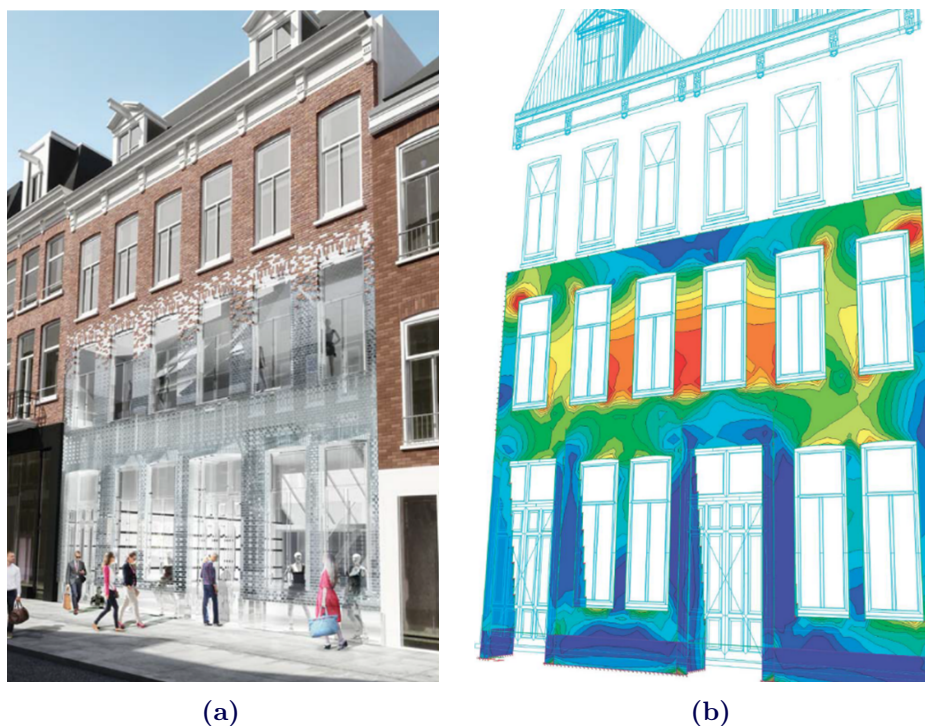


Figure 5.16: Crystal House impression, taken from Brincke (2016); (a)Impression; (b)Result from finite element analysis;

5.5.4 Force introduction

The introduction of forces into the glass requires some attention. Since glass is not able to deform plastically, an improper introduction of the loads lead to high local stresses. Compression tests done by Oikonomopoulou et al. (2014), show a decrease of the strength, when the load was introduced improperly. A nominal strength of 20-30MPa was the result of compression of a brick between two steel plates. This is significantly lower than the results that were found when an intermediate material was used to introduce the forces. Nominal strengths exceeding 135MPa were found in that case. Force transfer between two solids, only occurs at the location of contact points. High local stresses are the result, causing the glass brick to fail at a lower strength. When a soft intermediate material is

used, the stresses can be distributed more equally. To prevent local stress concentrations, attention must be given to the detailing. (Oikonomopoulou et al., 2014).

5.5.5 Design codes for glass

For the structural design of glass only national codes are available at this moment. Within the Structural Eurocodes section of the European Committee for Standardization, a working group is assigned to develop structural design rules for glass components. At the moment the pre-normative document CEN/TC250-WG3 serves as a guideline for the structural design of glass components. For the basis of the structural design and for the actions on structures the Eurocodes EN-1990 and EN-1991 are available.

In the Netherlands, the norm ‘NEN 2608’ is available, which uses a *limit state design approach*. It takes into account the statistical nature of the material strength. The characteristic value of the strength, corresponds to a 5% probability of breakage at the lower limit of the 95% confidence interval. To compute the design strength, several safety factors are applied. They cover different aspects that influence the capacity, such as the duration of the load.

Furthermore the consequence-based approach is implemented in the code. The code allows *local* failure in a structure, as long as the *global* structure is not compromised. Thereby it formulates several rules, such as: ‘local failure may not result in a person or object falling through’ and ‘damaged structural elements should be replaced shortly after failure’.

Although a lot of aspects have been implemented in the code already, it has its limitations. It mainly focuses on soda-lime-silica *float glass*, applied in buildings. In the future even more challenging implementations of structural glass will probably be strived for. Therefore it might be useful to develop the codes further on. An interesting development could be the implementation of *cast glass* elements in structures.

The code ‘NEN-EN 1990:2011’ handles the risk by formulating consequence classes. A higher consequence class means bigger consequences and thus requires a higher reliability index. The reliability index can be transferred into a probability of failure. So if the consequence class is higher, the allowed probability of failure is lower. The definitions of the consequence classes are given in Table 5.5. Based on the consequence class, the partial factors are established.

For glass, the code ‘NEN 2608:2014’ evaluates the risk for a *structural element* of float glass, based on the method of Fine and Kinney. The method determines the risk based on several factors and is given by the following formula:

$$RD = LD \times ED \times SD \quad (5.1)$$

In which,

RD is the Risk of Damage

LD is the Likelihood of Damage, intentional or unintentional

ED is the level of Exposure to the Damage

SD is the Seriousness of the consequences of the Damage

This method is further elaborated upon Appendix E.2.

Table 5.5: Consequence classes according to NEN-EN 1990:2011;

Consequence class	Description	Examples in civil engineering
CC3	Big consequences regarding the loss of human life, or very big economic consequences, social consequences or consequences for the surrounding	Stands, public buildings in which the consequences of failure are big, such as a concert room
CC2	Moderate consequences regarding loss of human life, severe economic consequences, social consequences or consequences for the surrounding	Residences and office buildings, public buildings in which the consequences of failure are limited, such as an office building
CC1	Limited consequences regarding loss of human life, or small or negligible economic consequences, social consequences or consequences for the surrounding	Buildings for agriculture where humans usually are not present, such as barns and greenhouses

5.5.6 Risk reduction

Although it is never possible to avoid risk entirely, it can be minimized by decreasing the probability and/or the consequence of an undesired event. Risk reduction in glass structures, usually focuses on reducing the consequences in the case of failure. The consequences that may arise are formulated. They are then resolved by taking the appropriate measures. At the level of the element, laminated glass can be applied for instance. In this way residual capacity is provided and the shards will not fall down (if supported properly). At the level of the structure, the most important measure is to provide a secondary load path if one element fails.

III Analytical and Numerical Stability Analysis

6	Analytical Stability Analysis	57
6.1	Introduction	57
6.2	Imposed displacements	59
6.3	Asymmetric load configurations	73
6.4	Results and Conclusions	84
7	Numerical Stability Analysis	87
7.1	Introduction	87
7.2	General model description	87
7.3	Support displacements	91
7.4	Asymmetric load scenario	94
7.5	Combination: Asymmetric and support displacements	96
7.6	Reduced interface stiffness	97
7.7	Conclusions	100

6 Analytical Stability Analysis

6.1 Introduction

Stability is the main structural criteria that affects an arched masonry bridge design. This chapter aims to provide insight in the failure behavior with respect to instability. It is investigated how the geometrical parameters of the design, affect the failure behavior. Therewith providing *diagrams* which can be used for an arched masonry bridge design. For TU Delft's glass masonry bridge a stability analysis is executed.

For glass masonry bridges, an arch shaped as a *circular segment* is deemed most practical. It has the advantage that it can be composed of smaller *identical* circular segmented bricks. Manufacturing distinctive brick shapes, would either require the production of distinctive steel molds, or post processing of the bricks. When using standard production techniques, it is most cost-effective and practical to keep the number of distinctive brick-geometries as low as possible. This is achieved through the circular segmented shape. Therefore, this chapter is based on circular arches.

Instability of an arched masonry structure may be caused by (a combination of) the following events:

- Support settlements (imposed displacements)
- An asymmetric load configuration

The sensitivity to these events, depends on the geometry. The geometry of a circular arch can be defined by three parameters: the span l , the rise f and the thickness t . From these parameters, the relative thickness t/l , and relative rise f/l can be computed. These parameters are related to the slenderness and the flatness respectively.

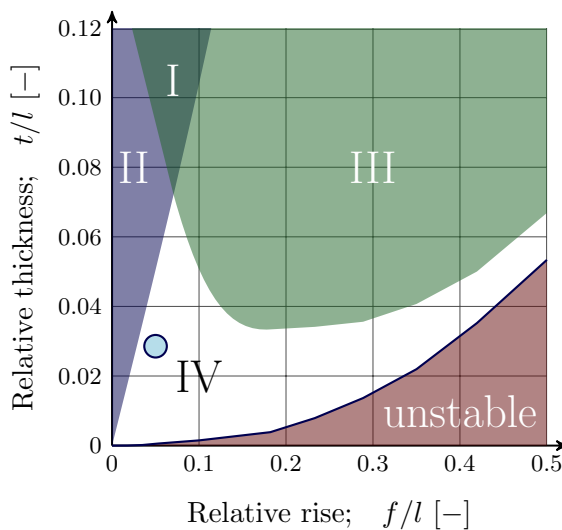


Table 6.1: Geometry categories and stability;

Cat.	Stable under:	
	Asymmetric load	Support settlements
I	✓	✓
II	✓	→ sec. 6.2
III	→ sec. 6.3	✓
IV	→ sec. 6.3	→ sec. 6.2

Figure 6.1: Geometry categories and stability;

Based on these properties it is proposed to distinguish four geometry-categories. These categories indicate which instability aspects are relevant to investigate, as shown in Figure 6.1 and Table 6.1. The areas corresponding to those categories have been established after the derivations provided in this chapter.

The red area in Figure 6.1 refers to arches that will collapse under their own weight. This area is based on the requirement that circular arches have to contain a parabolic line of thrust within their geometry (the parabola approximates a catenary). To do so, a minimal thickness is required. The green area indicates the arches for which collapse requires support-settlements larger than 4% of the span. The effect of settlements is therefore not likely to be significant and can be disregarded. How this area is defined will be shown in section 6.2. Arches in the blue area are not susceptible to an asymmetrical load. The definition of this area is derived in section 6.3.

Case study: Geometrical parameters

The required span for the case study is 14m. Since the arch will directly function as deck, pedestrians must overcome the slope of the bridge. The rise therefore follows from a limited maximum slope of the bridge. To assure a sufficiently safe and comfortable bridge, the maximum slope is limited to 10%. This provides a rise of $f = 0.7m$. An additional benefit of this relatively low rise, is the esthetically appealing slender appearance. As a starting point for the thickness, $t = 0.4m$ is chosen.

The result of these parameters is indicated by the dot in Figure 6.1. As can be observed, the bridge is located in category IV, which means that instability due to both settlements and asymmetric load configurations should be investigated.

In section 6.2 instability due to settlements and other imposed displacement loads is investigated. In section 6.3, instability due to asymmetric loads is discussed.

6.2 Imposed displacements

6.2.1 Introduction

Up to a certain level, an arch is able to accommodate itself to supports-settlements. If they become sufficiently large however, the arch becomes unstable due to the formation of a mechanism. Which failure mechanism occurs, depends on the geometry. Based on the failure behavior concerning settlements, three geometry-regions may be distinguished. These regions are illustrated in Figure 6.2, which is derived in this section. The characteristic behavior of the arches in each region is presented in Figure 6.3. Region A indicates arches which fail by a 3-hinge snap-through mechanism and has stationary hinges. Region C indicates arches that fail by a 5-hinge mechanism. In this region the hinges will shift during the settlements, to accommodate for the changes in the line of thrust. Region B indicates a 'transition zone'. In this region the hinges will not move up until the point that the line of thrust becomes tangent to the geometry at the location of the supports.

This section starts by defining the *boundaries* between the geometry-regions. Subsequently, the settlement-behavior for each region is analyzed, which results in the *contour lines* shown in Figure 6.2. It is then shown how this diagram can be used to optimize the geometry of a design. Subsequently it is shown how the geometrical non-linear behavior can be incorporated into the formulations, after which a geometrically non-linear analysis can be executed for the case study.

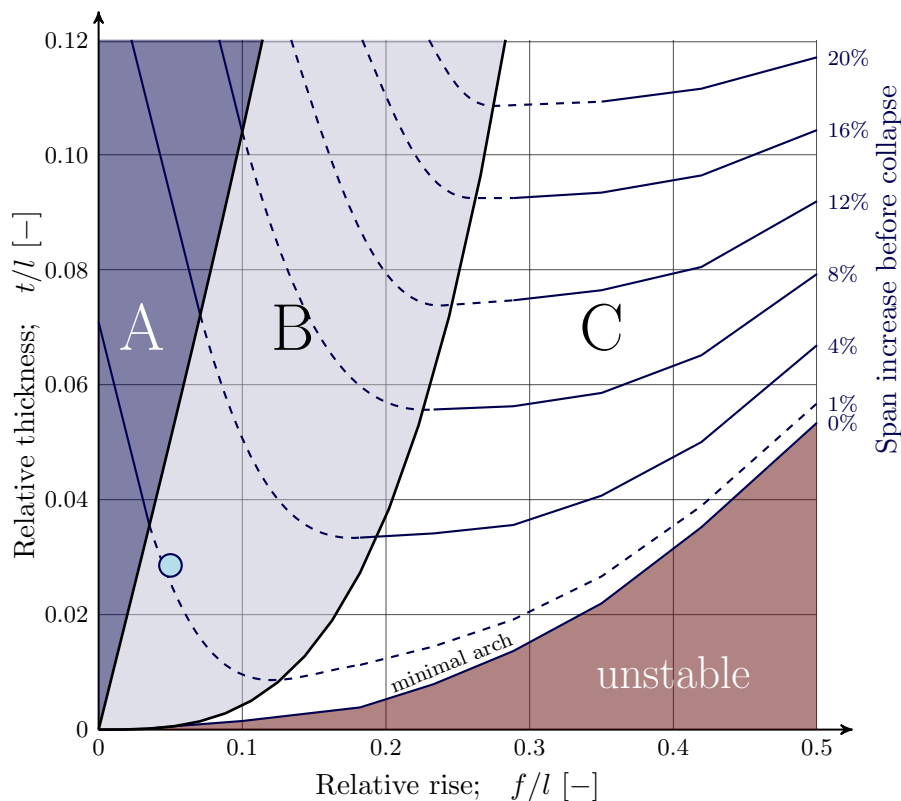


Figure 6.2: The three geometry-regions, which each have a characteristic failure behavior; These regions affect the trajectory of the contour lines, that indicate the span increase at collapse; Dot indicates geometry of the case study;

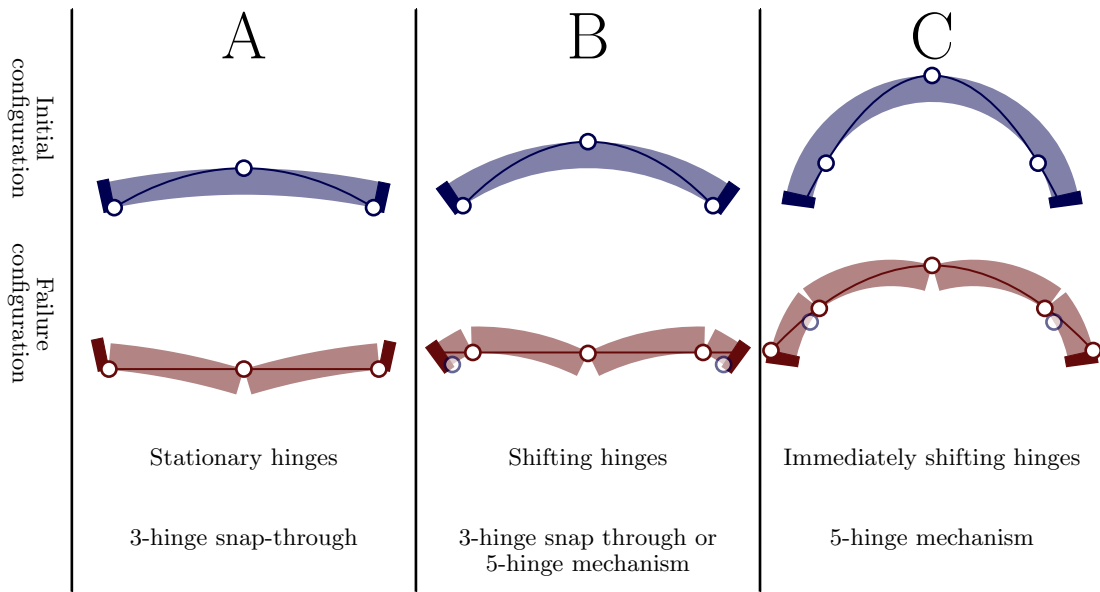


Figure 6.3: Characteristics of the three geometry-regions;

6.2.2 Definitions of the region-boundaries

Here the derivations of the region boundaries A-B and B-C are given. The A-B-boundary was found by Oschendorf (2002) and is rewritten in a different geometry-notation. The B-C boundary is not literature-based.

Boundary between region A and B

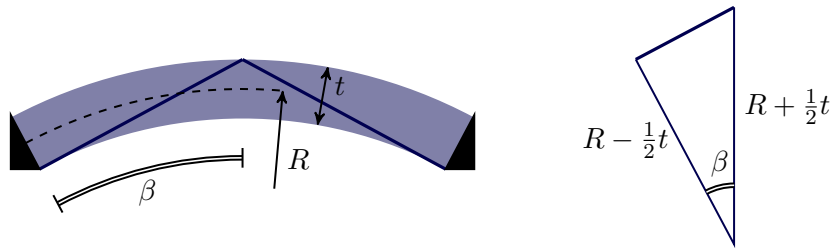


Figure 6.4: Definition of an arch at the boundary between region A and B: An arch with a straight line between the initial hinge locations, which is tangent at the supports;

At the moment that an arch in region A collapses, the line of thrust is horizontal (Figure 6.3). So for an arch in region A, it must be possible to draw a straight line between the hinges, without exceeding the geometrical boundaries. An arch on the boundary between region A and B, is shown in Figure 6.4. The straight line is tangent to the intrados (inner geometrical boundary) at the support. An expression for the boundary between A and B can be derived using this figure:

$$\beta = \arccos \left(\frac{1 - \frac{t}{2R}}{1 + \frac{t}{2R}} \right) \quad (6.1)$$

The advantage of defining a circle by the parameters R , β and t (compared to f , l and t), is that in some cases it results in simpler expressions. Interpretation of the results however, may be more difficult. In order to assess the effect of variations in height for example, both parameters β and R must be adjusted. Therefore expression (6.1) is rewritten such that it provides the slenderness for any given flatness:

$$\frac{t}{l} = \frac{2(1 - \cos \beta)}{1 + \cos \beta} \cdot \frac{1}{2 \sin \beta} \quad (6.2)$$

$$\text{where } \beta = \arcsin \left(\frac{\frac{f}{l}}{\left(\frac{f}{l}\right)^2 + \frac{1}{4}} \right) \quad (6.3)$$

These expressions have been used to indicate the boundary between region A and B in Figure 6.2. The derivation of (6.2) and (6.3) from (6.1), is given in Appendix C.1.

Boundary between region B and C

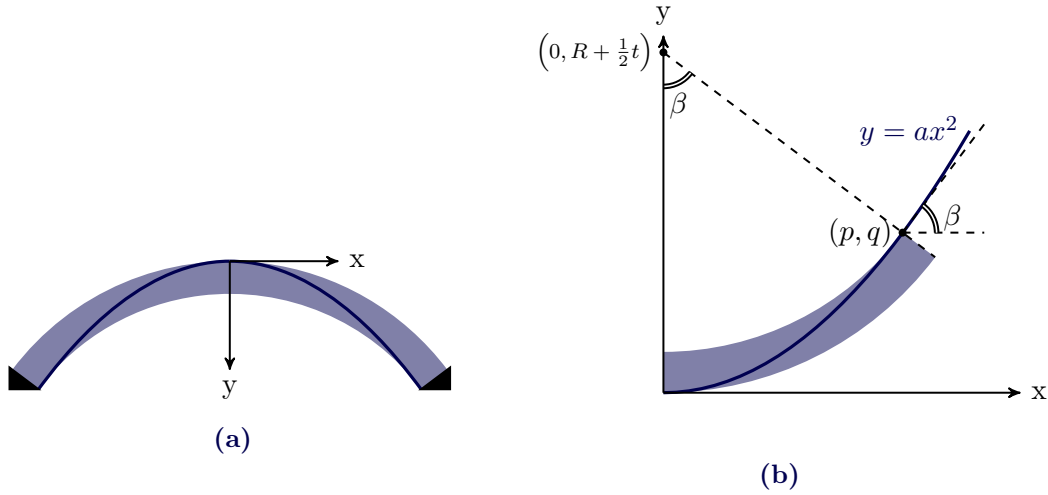


Figure 6.5: Definition of an arch at the boundary between region B and C: Initial line of thrust is tangential at the supports;

An arch at the boundary of region B and C, has a parabolic line of trust that is tangential at the supports, as illustrated in Figure 6.5a. To provide an expression for this boundary, the coordinate system is chosen such that its origin is located in the vertex of the parabola. This provides Figure 6.5b. It must hold that the slope of the parabola is equal to the slope of the intrados, at the indicated coordinate (p, q) . This provides the following equation:

$$\frac{2q}{p} = \tan(\beta) \quad (6.4)$$

The coordinates p and q are given by the following expressions:

$$p = (R - \frac{1}{2}t) \cos(-90 + \beta) \quad (6.5)$$

$$q = R + \frac{1}{2}t + (R - \frac{1}{2}t) \sin(-90 + \beta) \quad (6.6)$$

Substituting (6.5) and (6.6) in equation (6.4) and simplifying the result, provides the following definition of the boundary between region B and C:

$$\frac{R + \frac{1}{2}t}{R - \frac{1}{2}t} \cos(\beta) = 1 - \frac{1}{2} \sin^2(\beta)$$

6.2.3 Settlement analysis

The percentage that the span of an arch can increase before it collapses, is indicated by the contour lines of Figure 6.2. The failure mechanism that arises due to settlements, differs per region. Therefore also the trajectory of the contour lines does. The part of the contour lines that is located in region A, follows from an analytical relation. This relation will be derived in this subsection. Region B can be considered as a transition zone and will be investigated as well. For region C the contour lines have been derived using results found in literature.

Settlement analysis region C

The five-hinge collapse mechanism corresponding to region C, was investigated by Oschen-dorf (2002). The investigation depended on an iterative model, validated by some physical experiments. The results were used to construct (the non-dashed part of) the contour lines in region C. The process of this construction is provided by Appendix C.2.

Settlement analysis region A

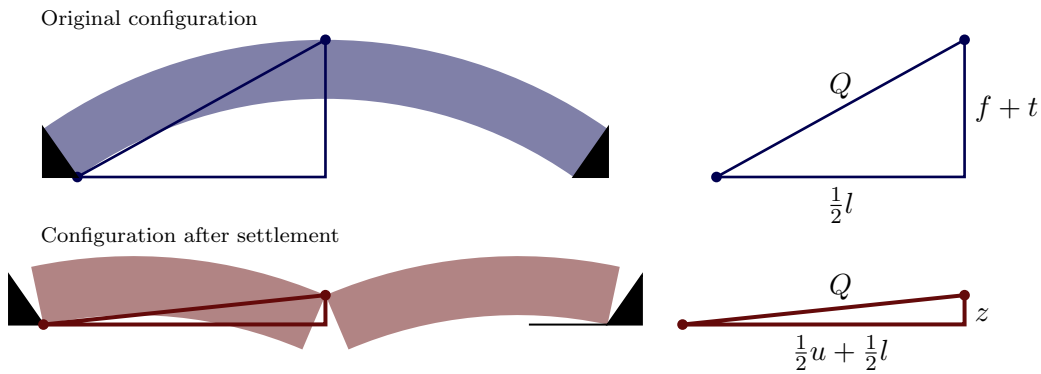


Figure 6.6: Rigid body movement [Q is a constant length];

The effect of settlements can be assessed using rigid body kinematics. Assuming an infinite stiffness, hinges will directly be formed when settlements start to occur. They will be located at the supports and in the middle of the arch. Instability in the form of a snap-through mechanism will occur as soon as the hinges are on a horizontal line. The vertical distance between the hinges, z may be expressed as a function of the total displacement u . Using Figure 6.6, the following formula may be derived:

$$z(u) = \frac{1}{2} \sqrt{l^2 + (2f + 2t)^2 - (l + u)^2} \quad (6.7)$$

This relationship is plotted in Figure 6.7 [Animated in the online version of this report].

The contour lines of Figure 6.2, indicate the *span increase percentage till collapse*. For region A these contour lines can be derived by substituting $l + u = \xi l$ and $z = 0$ in equation (6.7). The variable ξ is the span increase factor at the moment of collapse, i.e. for a span increase percentage of 2%, this factor equals $\xi = 1.02$. The contour lines are defined by the following formula:

$$\frac{t}{l} = -\frac{f}{l} + \frac{1}{2} \sqrt{\xi^2 - 1}$$

Figure 6.7: Relation between z and u ; ANIMATED IN ONLINE VERSION;

Settlement analysis region B

An arch in region B initially behaves the same as one in region A. Thus, the hinges will initially be located at the supports and in the middle. This means that the same rigid body movement occurs, as expressed by formula (6.7). After a certain settlement however, the line of thrust will be tangent to the intrados of the arch, as illustrated in Figure 6.8. At this point the outer hinges will start to shift to the middle, similar as to what happens in region C. Increasing the settlements further, will finally result in collapse.

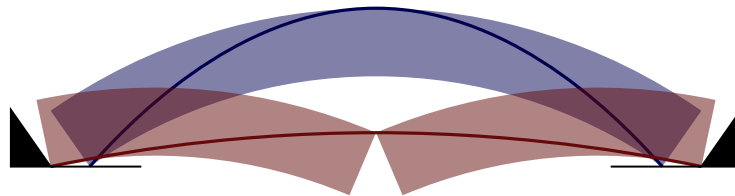


Figure 6.8: An arch in region B; (blue) In its original configuration; (red) At the moment the line of thrust becomes tangent to the intrados;

So up to a certain limit, formula (6.7) can be used for region B as well. The settlement

corresponding to this limit, is determined using Figure 6.9 [Animated in the online version of this report]. To reduce complexity of the derivation, the coordinate system is conveniently chosen and the parameters R , β and t are used to express the geometry of the arch. The line of thrust is tangent to the intrados after the circle segment has rotated by an angle α_t .

Figure 6.9: Parametric illustration to determine the settlement for which the line of thrust becomes tangent with the intrados; ANIMATED IN ONLINE VERSION

The expressions for the coordinates can be derived using Figure 6.9:

$$\begin{aligned}
 p &= (R - \frac{1}{2}t) \cos(-90 + \beta) \\
 q &= R + \frac{1}{2}t + (R - \frac{1}{2}t) \sin(-90 + \beta) \\
 \\
 v &= (R + \frac{1}{2}t) \cos(90 - \alpha_t) \\
 w &= (R + \frac{1}{2}t) \sin(90 - \alpha_t) \\
 \\
 r &= v + (R - \frac{1}{2}t) \cos(-90 - \alpha_t + \beta) \\
 s &= w + (R - \frac{1}{2}t) \sin(-90 - \alpha_t + \beta)
 \end{aligned}$$

After a rotation α_t , the line of thrust can be defined by a parabola of the form $y = ax^2$, intersecting the point (r, s) . This means that $a = s/r^2$. The slope of the line of thrust at the support can be found by computing the derivative in point (r, s) .

$$\begin{aligned}
 y'(x) &= 2ax = \frac{2s}{r^2} \cdot x \\
 y'(r) &= \frac{2s}{r}
 \end{aligned}$$

This slope must be equal to the slope of the intrados, which provides the following equation:

$$\frac{2s}{r} = \tan(\beta - \alpha_t)$$

Using this equation, the angle α_t can be computed. The result can be used to compute all relevant coordinates. The coordinates can be used to determine the settlement for which the line of thrust becomes tangent and the hinges will start to shift.

$$u = 2(r - p)$$

For an arch close to the boundary with region A, the settlement-boundary is close to the maximum settlement. Therefore this arch behaves almost entirely the same as an arch in region A. By moving away from this boundary, the behavior will start to deviate. Similarly an arch close to the boundary with region C behaves almost entirely the same as an arch in region C. Therefore it is expected that the contour lines in region B, illustrated in Figure 6.2 are tangent at both region boundaries. Based on these considerations, the dashed part of the contour lines have been drawn.

6.2.4 Volume optimization

When the contour lines that represent equal bridge-volumes are drawn into Figure 6.2, this results into Figure 6.10. This enables optimization of the geometry. The ratios t/l and f/l can be chosen such that the resistance against support settlement instability is the highest. To do so these parameters should be chosen around the orange line presented in the figure.

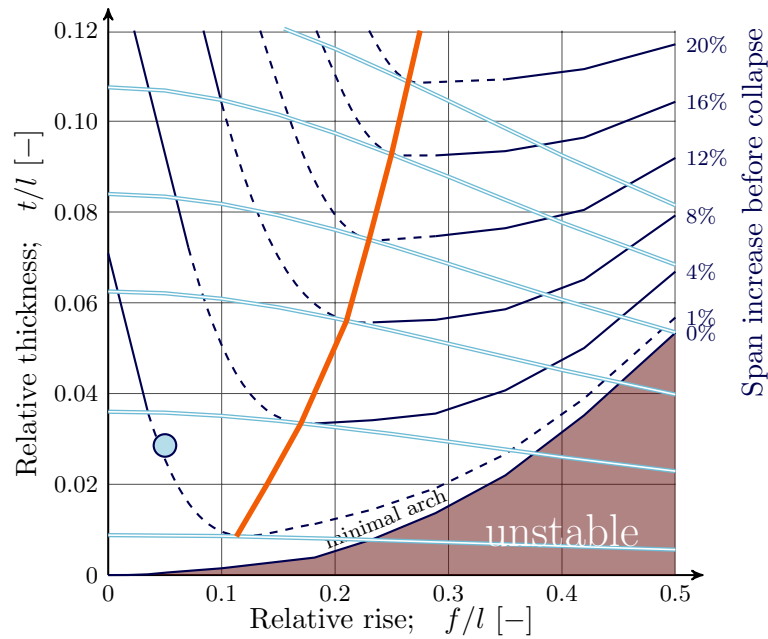


Figure 6.10: Contour lines for which the volume of the material is equal, so chosen ratios can be optimized such that the arch is best resistant against settlements;

6.2.5 Geometrical non-linearity

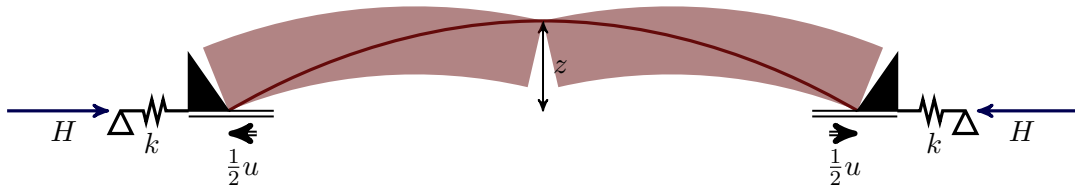


Figure 6.11: Snap through model with implemented horizontal support stiffness

It was stated that when the middle hinge is on a horizontal line with the outer hinges, the arch becomes unstable. This is based on the assumption that the arch is infinitely stiff and that the settlements are independent of the horizontal support reaction. However, it is more likely to assume that as the horizontal support reactions increase, the settlements do as well. To implement this effect, the horizontal support stiffness k is introduced, as shown in Figure 6.11. Instability now arises after reaching the critical point, i.e. the point for which the maximum applicable load has been reached. To determine the critical point, the distributed load corresponding to a certain settlement is expressed:

$$q = \frac{8Hz}{l^2} \quad (6.8)$$

$$\text{where } z = \frac{1}{2} \sqrt{l^2 + (2f + 2t)^2 - (l + u)^2} \quad (6.9)$$

$$\text{and } H = \frac{k}{2} \cdot u \quad (6.10)$$

Due to geometrical non-linearity a softening can be observed in the q, u -diagram in Figure 6.12. Due to this softening, the maximum applicable load (q_{crit}) is reached *before* the hinges are on a horizontal line (which happens at u_{max}). As the functional height of the arch (z) decreases, the horizontal support reaction corresponding to a certain load-increment becomes much higher. Therefore the settlements corresponding to this load-increment will also increase. When the critical load is reached, an equilibrium can no longer be found, resulting in snap-through failure.

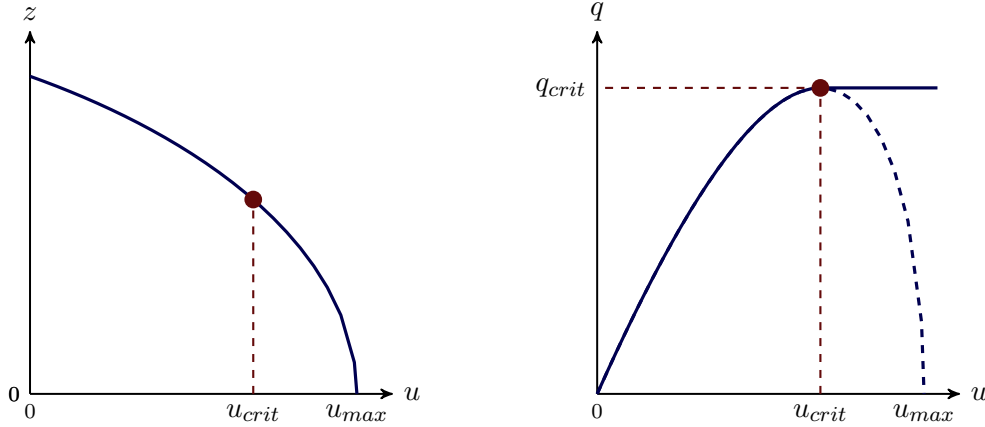


Figure 6.12: z, u - and q, u -diagram based on (6.8), (6.9) and (6.10); At u_{max} the hinges are on a horizontal line indicating the instability-boundary. However due to geometrical non-linearity, instability occurs at u_{crit} , before u_{max} is reached.

6.2.6 Stability verification

Thus far the effect of support settlements on the stability has been investigated. Thermal loads and axial shortening have the same effect and can therefore also be regarded as settlements. For stability-verification it is convenient to incorporate these effects into equation (6.10). Snap-through verification is only relevant for arches in region A and B, which are rather flat. Therefore the assumption can be made that the axial shortening is directed horizontally, despite being directed along the circle segment in reality. Concerning the temperature, both axial thermal expansion and the displacement due to a positive temperature gradient are implemented. This provides the following equation:

$$u_{tot} = \underbrace{\left(\frac{l}{EA} + \frac{2}{k}\right)H}_{\text{non-linear}} + \underbrace{\alpha l \left(\frac{2}{3} \frac{f}{t} \Delta T_M - \Delta T_N\right)}_{\text{linear}} \quad (6.11)$$

Note that thermal *expansion* compensates for the settlements (minus sign), therefore thermal *shrinkage* should be considered instead. Expressing equation (6.11) in terms of H provides:

$$H = \frac{u_{tot} - \alpha l \left(\frac{2}{3} \frac{f}{t} \Delta T_M - \Delta T_N\right)}{\left(\frac{l}{EA} + \frac{2}{k}\right)} \quad (6.12)$$

Proposed is the following method for an analytical assessment, regarding instability due to a snap-through mechanism:

A method to verify the stability of a masonry arch in geometry-regions A and B, in which geometrical non-linearity is incorporated:

- Use equations (6.8), (6.9) and (6.12) to obtain the q,u -diagram
- Compute the critical load
- Compute the load corresponding to the moment when the hinges start shifting and this method is no longer valid, as explained in subsection 6.2.3 (geometry-region B only)
- Execute the governing unity check:

$$\frac{q_d}{q_{crit}} \leq 1 \quad \frac{q_d}{q_{hingeshift}} \leq 1$$

- If the second unity check is not met, this means that the hinges will start moving and this method is no longer valid.

Note: Geometrical non-linearity is relevant in region A and B, since the horizontal support reaction significantly increases as the instability boundary is approached. For region C the increase of the horizontal support reaction is minimal. To verify the stability of an arch in region C, the occurring support movement should be checked against the support movement at collapse (with a certain margin of safety). The support movement at collapse can be determined from the contour lines in Figure 6.2.

Case study: Verification of the stability under support settlements

The geometry defined for TU Delft's Glass Masonry Bridge, is within geometry-region B, as indicated in Figure 6.2. Therefore the just proposed method for analytical stability assessment can be used. For this analysis, the following parameters are used:

$$\begin{aligned} l &= 14m \\ f &= 0.7m \\ t &= 0.4m \\ b &= 2.4m \\ E &= 70 \cdot 10^6 kN/m^2 \\ \alpha &= 9 \cdot 10^{-6} K^{-1} \\ k &= 4.8 \cdot 10^4 kN/m \end{aligned}$$

The young's modules and thermal expansion coefficient of soda-lime silica glass are used, as presented in Table 5.3. The support stiffness is based on the requirement that the abutments have to satisfy: The horizontal settlement of each abutment may not be bigger than $10mm$ under a horizontal load of $1155kN$. From this requirement, the stiffness of each support *per meter width* can be derived: $1155/(2.4 \cdot 0.01) = 4.8 \cdot 10^4 kN/m$. It is chosen to consider the soil settlements by defining a stiffness rather than applying an imposed load. In this way non-linear effects can be taken into account, i.e. the settlements can become larger if the horizontal force becomes larger due to non-linearity. In case that steel ties would be used for the horizontal support reaction, the same stiffness

could be achieved through a total cross sectional area of:

$$A_{steel} = \frac{Hl}{Eu} = \frac{1155 \cdot 14}{200 \cdot 10^6 \cdot 2 \cdot 0.01} \cdot 10^6 = 4043 \text{mm}^2$$

This corresponds to *two* steel ties with a diameter of:

$$d = 2 \cdot \sqrt{\frac{A}{2 \cdot \pi}} = 51 \text{mm}$$

The load cases and load combinations are obtained using the NEN-EN 1991, as shown in Appendix B.1 and Appendix B.2 respectively. The load scenario is illustrated in Figure 6.13. The governing load combination is LC2, where traffic is the directive variable load:

$$\begin{aligned} q_d &= 1.2q_G + 1.35q_T + 0.45q_W = 1.2 \cdot 10 + 1.35 \cdot 5 + 0.45 \cdot 0.5 = 19.0 \text{kN/m}^2 \\ \Delta T_N &= -27 \cdot 0.45 = -12.15^\circ \text{C} \quad \rightarrow \quad u_{T_N} = 1.53 \text{mm} \\ \Delta T_M &= 12 \cdot 0.45 \cdot 0.75 = 4.05^\circ \text{C} \quad \rightarrow \quad u_{T_M} = 0.59 \text{mm} \end{aligned}$$

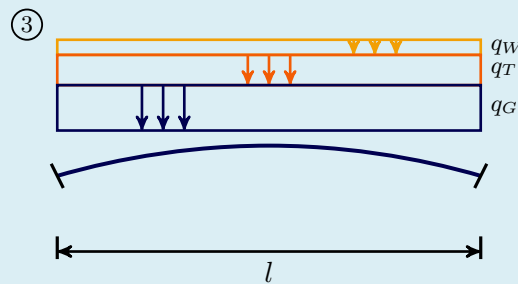


Figure 6.13: Worst case load scenario with respect to the support reactions;

By filling in the parameters in equations (6.8), (6.9) and (6.12), the following formula is obtained:

$$q(u) = \frac{8}{14^2} \frac{u - 2.1 \cdot 10^{-3}}{4.22 \cdot 10^{-5}} \cdot \frac{1}{2} \cdot \sqrt{(14)^2 + (2 \cdot 0.7 + 2 \cdot 0.4)^2 - (14 + u)^2} \quad (6.13)$$

This formula is displayed in the q, u -diagram in Figure 6.14. The critical displacement is obtained by solving $q'(u) = 0$, which provides:

$$u_{crit} = 0.115 \text{m} \quad (6.14)$$

Using equation (6.13) the corresponding critical load can now be computed:

$$q_{crit} = 69.3 \text{kN/m} \quad (6.15)$$

Since the geometry of the arch is within geometry-region B, the settlement is computed for which the hinges will start to move and the trajectory is no longer valid. Using the expressions provided in section 6.2.3 this value is obtained:

$$u_{shiftinghinges} = 0.158m \quad (6.16)$$

The dashed line segment in the z, u -diagram in Figure 6.14, indicates that the relationship between z and u will now deviate from the analytical formula. However, since this will happen after the critical load has been reached, it is not of concern.

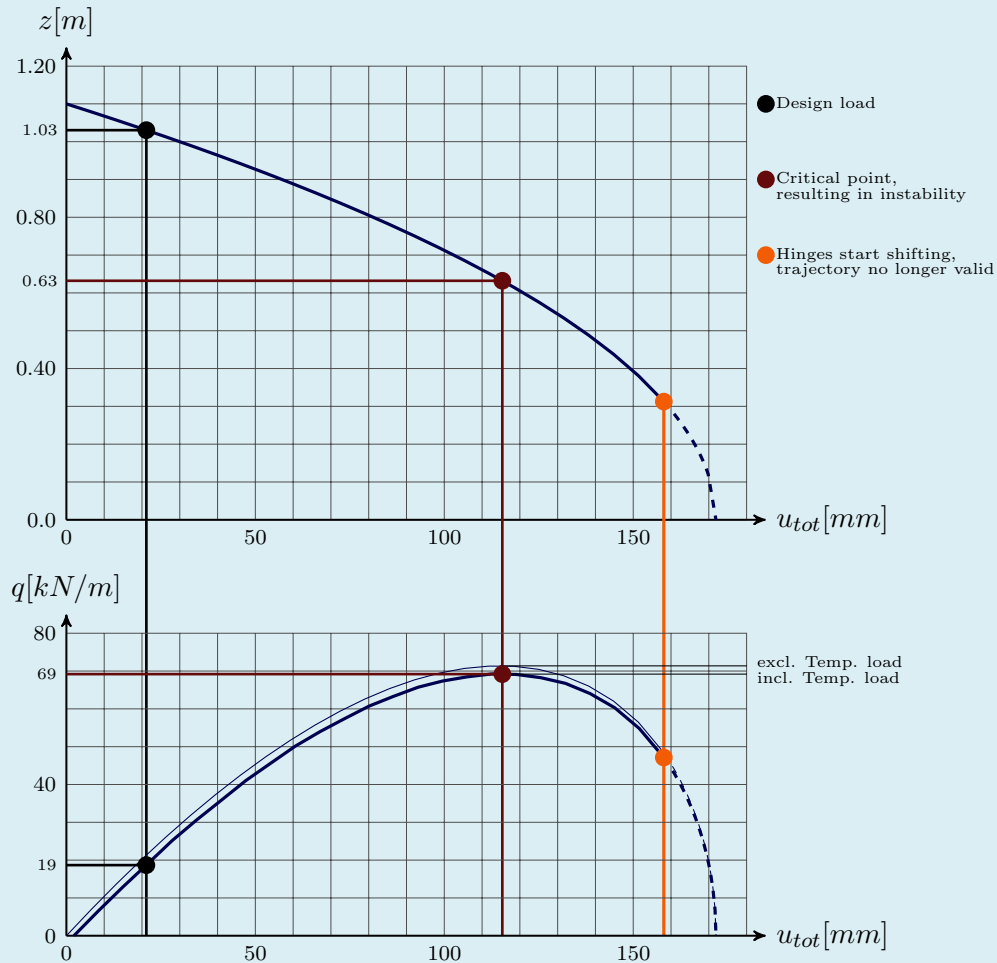


Figure 6.14: z, u -diagram and q, u -diagram, in which the stability is analyzed;

The governing unity check is executed:

$$\frac{q_d}{q_{crit}} = \frac{19.0}{69.3} = 0.27 \leq 1 \quad \checkmark \quad (6.17)$$

The unity check is satisfied, meaning that the arch will be stable under the design load. For the design load the total settlement is 21mm, which corresponds to a sag of 69.6mm. In Figure 6.15 the configuration of the arch at several characteristic points is shown.

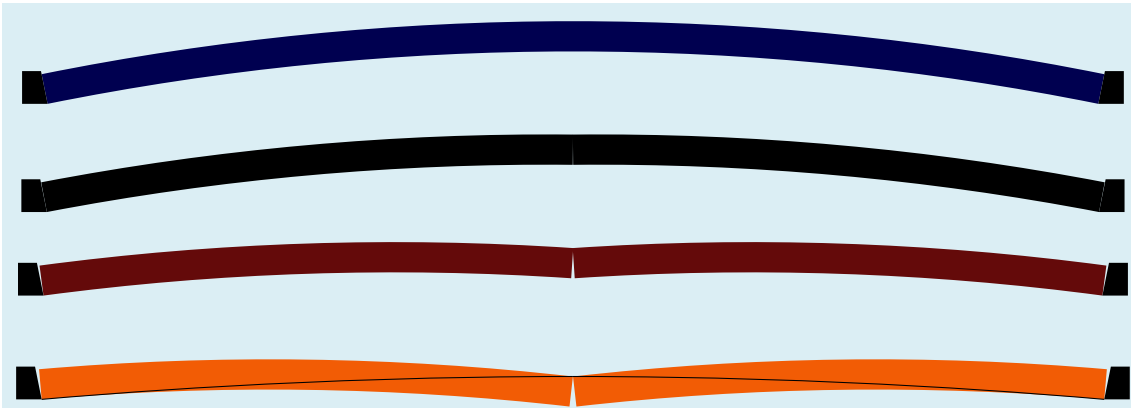


Figure 6.15: Configuration of the arch, for several typical points; From top to bottom: Initial configuration, configuration under design load, configuration for critical load, configuration when line of thrust is tangent to the intrados;

So the distributed load q can increase to $69.3kN/m$ before instability occurs, given the linear imposed displacement (in this case resulting from temperature effects). Another question that arises is for which displacement instability occurs. The total displacement is composed of a linear and a non-linear part:

$$u_{tot} = u_l + u_{nl}$$

The total displacement for which instability occurs depends on the size of the distributed load q . For a higher q the total displacement for which instability occurs is higher. Given a certain q , the total displacement can be determined. To find this value, equation (6.8), (6.9) and (6.11) are used to formulate two expressions for the horizontal support reaction:

$$H_1 = \frac{1}{\left(\frac{l}{EA} + \frac{2}{k}\right)} u_{nl}$$

$$H_2 = \frac{ql^2}{8z(u_{tot})} = \frac{ql^2}{4\sqrt{l^2 + (2f + 2t)^2 - (l + u_l + u_{nl})^2}}$$

It must hold that:

$$H_1(u_{nl}, u_l) = H_2(u_{nl}, u_l) \quad (6.18)$$

So given a certain linear displacement u_l , the corresponding non-linear displacement can be found. Typically two solutions are found: One stable solution and one that occurs during collapse. This can be understood by drawing a horizontal line in Figure 6.14. However for a certain value of the linear displacement, only one solution is found. This solution is the boundary between stability and instability. Equation (6.18) has only one solution if it holds that:

$$\frac{d}{du_{nl}} H_1(u_{nl}, u_l) = \frac{d}{du_{nl}} H_2(u_{nl}, u_l) \quad (6.19)$$

Figure 6.16 is constructed by solving equations (6.18) and (6.19), using Maple. It shows the displacements at the boundary of instability. Note that for $q = 71kN$, no

additional linear displacements can be resisted. For a design load of 19kN a maximum linear displacement of 100mm can be applied, before instability occurs. At this point the displacement due to the non-linear displacement is 48mm, which makes the total displacement at collapse 148mm. Note that the non-linear displacement at collapse is bigger than the initial value, since it increases as the linear displacement increases.

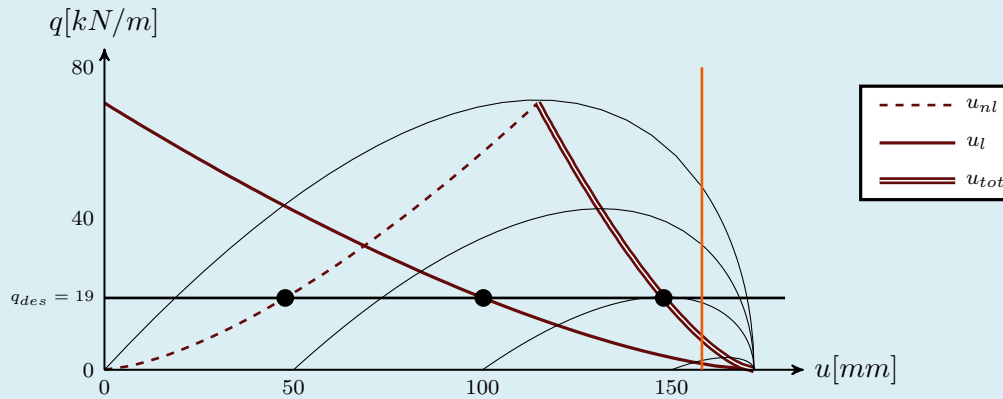


Figure 6.16: Displacements at the boundary of instability: For the design load of 19kN a maximum linear displacement of 100mm can be applied (the non-linear displacement will than be 48mm, which makes the total displacement at collapse 148mm);

A unity check for the displacement can be executed:

$$\frac{u_{tot,d}}{u_{tot,collapse}} = \frac{21}{148} = 0.14 \leq 1 \quad \checkmark \quad (6.20)$$

Both Unity checks's (6.17) and (6.20) are sufficiently low and therefore the stability of TU-Delft's glass masonry bridge is sufficient, based on the assumption that it consists of solid glass bricks only.

6.3 Asymmetric load configurations

6.3.1 Introduction

Under its self-weight, an arch has a symmetric line of thrust. An external asymmetric load causes a disturbance in the line of thrust, which may result in a four-hinge mechanism. Whether an asymmetrically loaded arch is stable, depends on the following aspects:

- geometry
- load configuration
- ratio between asymmetric load and self-weight

For certain *geometries* the stability can be guaranteed independent of the other aspects. For these ‘unconditionally’ stable arches an analysis of the stability under asymmetric loading is superfluous. This section starts by defining the set of arch-geometries for which this qualification holds.

If the arch can not be considered as unconditionally stable, an additional analysis is necessary. In this section two asymmetrical load scenarios are assessed, by composing the corresponding differential equations. These provide the eccentricity of the line of thrust. According to the *master safe theorem*, which was introduced in Chapter 4, the arch is stable if the line of thrust can be contained within its boundaries. For the case study it is then shown how the minimal required thickness can be obtained and if it is sufficiently thick. After that, a diagram is composed that provides the minimal required thickness for several spans and rise/span-ratios, such that it can be used for an arched masonry bridge design.

6.3.2 Unconditionally stable arch

For a certain set of arch-geometries, instability due to an asymmetric load configuration is not possible. In the introduction of this chapter, this set is indicated by the blue area in Figure 6.1. This area is based on an expression which will now be derived. To do so the following definition of an unconditionally stable arch is introduced:

Unconditionally stable arch: An arch that is stable under any asymmetrical load configuration, independent of the ratio between the asymmetric load and self-weight.

The most unfavorable scenario would be the application of a point load at a certain position along the span. So for possible location for the point load, the line of thrust must be contained within the geometry, as illustrated in Figure 6.17. It can be observed that this requirement is fulfilled, if a horizontal line can be contained within the geometry. To make the analysis independent of the ratio between the asymmetric load and self-weight, the advantageous effect of the self-weight is disregarded.

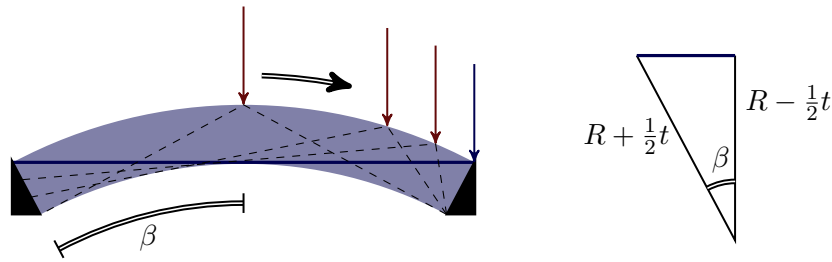


Figure 6.17: Definition unconditionally stable arch

A horizontal line can be contained if the following requirement is fulfilled:

$$\beta \leq \arccos \left(\frac{1 - \frac{t}{2R}}{1 + \frac{t}{2R}} \right)$$

Note that this result is the same as was found for the boundary between region A and B in section 6.2. The results are the same since the requirement that an unconditionally stable arch has to satisfy is indirectly the same as the requirement that an arch in region A has to satisfy (see Figure 6.4).

6.3.3 Analytical safety assessment

If the geometry of an arch is not a part of the unconditionally stable geometry-set, an additional analysis is required to state whether the arch is stable under a asymmetrical load configuration. To perform this analysis, the master safe theorem presented in Chapter 4 may be used:

Theorem 6.1 — The master safe theorem

If any position for the *line of thrust* can be found that lies *within the boundaries* of the masonry, then this is absolute proof that the structure is *stable* and collapse can never occur under the given loading.

A possible position for the line of thrust may be found by applying the load configuration on a cable and then inverting the result. However this method provides many solutions, depended on the chosen cable length or on the chosen horizontal support reaction. Another possibility is computing the elastic solution based on the ‘beam + inverted cable’-system. The horizontal support reaction in this analysis is based on the elastic properties of the arch. If this solution lies within the boundaries, the arch is stable.

Note that the elastic solution is **not** the actual solution, as was explained in Chapter 4. The actual solution cannot be obtained, since the structure is hyperstatic. This is why the master safe theorem is used in the first place.

In this report, the two asymmetrical load scenarios presented in Figure 6.18 are considered. For an arched masonry pedestrian bridge these scenarios may be critical. A background on these scenarios is provided by Appendix B.3.

To analyze these scenarios a differential equation is formulated for each continuous interval. Discontinues locations are the locations where there is a sudden change in loading. For scenario 1 two domains can be distinguished, as shown in Figure 6.19. Therefore the

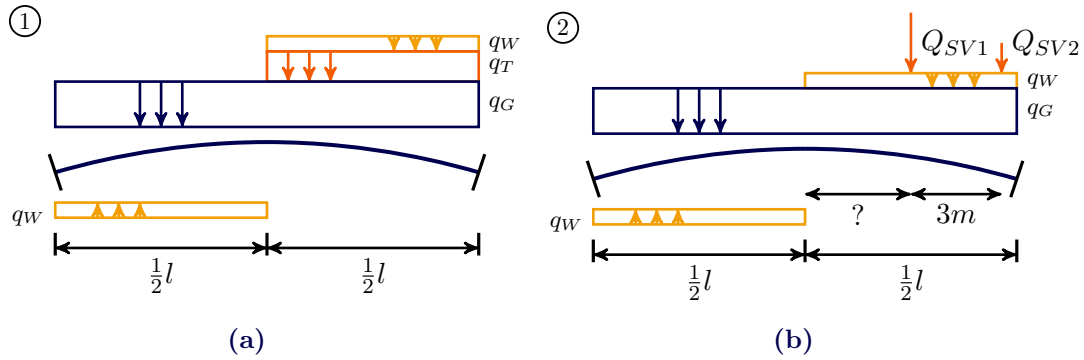


Figure 6.18: Unfavorable load scenarios with respect to stability; (a)Scenario 1: Asymmetrically loaded by crowd; (b)Scenario 2: Asymmetrically loaded by service vehicle;

following differential equations are formulated.

$$EI \frac{d^4 w_A}{dx^4} + H \frac{d^2 z}{dx^2} = q_A(x)$$

$$EI \frac{d^4 w_B}{dx^4} + H \frac{d^2 z}{dx^2} = q_B(x)$$

Integration will result in four unknown integration-constants for each differential equation. They can be solved by formulating the four boundary conditions and the four matching conditions for each domain-split:

$$\begin{aligned} \text{at } x = -\frac{1}{2}l &\rightarrow w_A = 0; \quad \phi_A = 0; \\ \text{at } x = 0 &\rightarrow w_A = w_B; \quad \phi_A = \phi_B; \quad M_A = M_b; \quad V_{z,A} = V_{z,B}; \\ \text{at } x = \frac{1}{2}l &\rightarrow w_B = 0; \quad \phi_B = 0; \end{aligned}$$

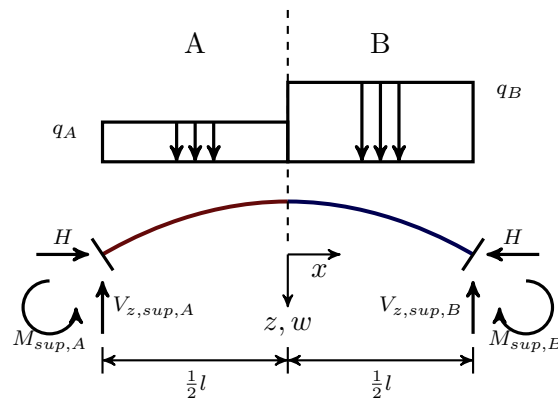


Figure 6.19: Schematic drawing of an arch under a discontinuous load configuration;

Since this method only holds for rather flat arches, some additional simplifications are made based on the flat-arch assumption:

- The loads are horizontally distributed (Appendix D.1)
- The (circular) shape of the arch may be modeled as a parabola (Appendix D.2)

Due to these simplifications, the results are better interpretable. The validity and accuracy of these simplifications are investigated in the stated appendices.

Application of the boundary- and matching conditions onto the differential equations, provides the position of the line of thrust. The eccentricity of the line of thrust (i.e. the location relative to the centroidal-axis), is provided by the following expressions:

$$e_A(x) = -\frac{1}{2} \frac{(q_A - q_B)(8x^2 + 3lx)f}{(q_A + q_B)l^2} \quad (6.21)$$

$$e_B(x) = -\frac{1}{2} \frac{(q_A - q_B)(-8x^2 + 3lx)f}{(q_A + q_B)l^2} \quad (6.22)$$

The location of the line of thrust can be obtained using the following equations:

$$z_{t,A}(x) = z(x) + e_A(x) \quad (6.23)$$

$$z_{t,B}(x) = z(x) + e_B(x) \quad (6.24)$$

For load scenario 2 a similar procedure can be executed. At three locations a discontinuity arises, dividing the arch into four domains as illustrated in Figure 6.20a. This results in four differential equations with 16 unknown integration constants. The point loads are implemented through the coupling equations regarding the vertical force, as shown in Figure 6.20b.

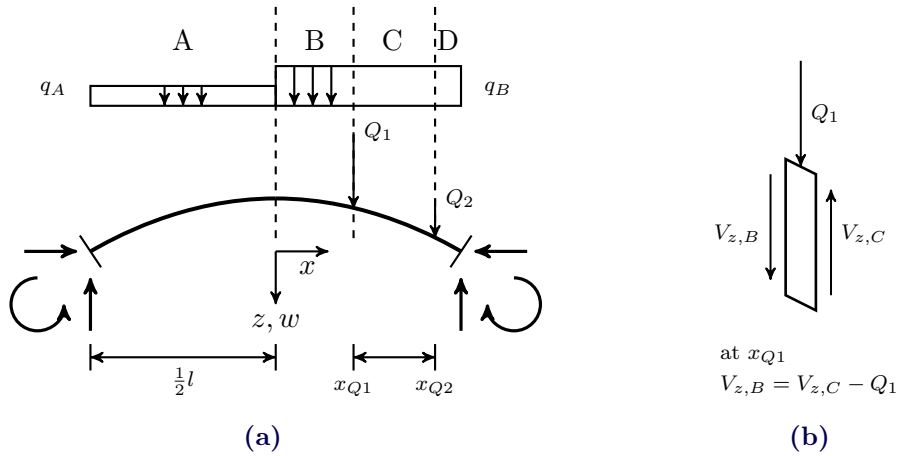


Figure 6.20: (a) Schematic drawing of an arch with several discontinuities; (b) Matching condition at the location of a point load

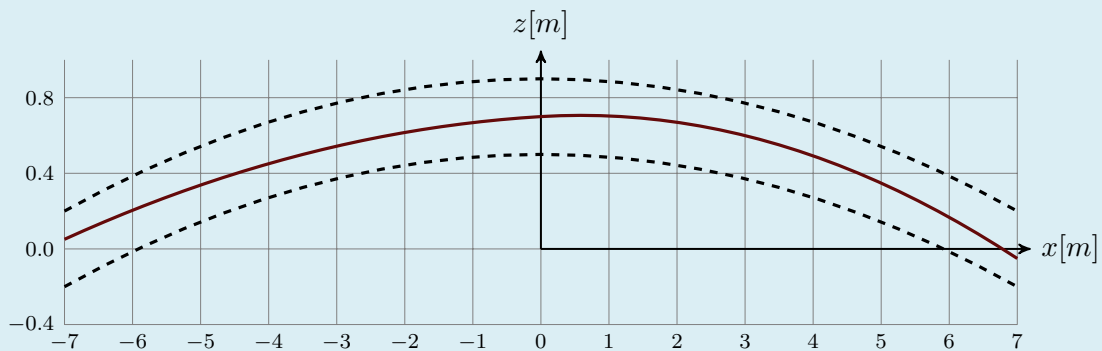
Establishing that the elastic solution lies within the geometry is prove that the arch is resistant against the asymmetrical load configuration. However, the amount of resistance is yet to be determined. This is done by computing the *minimal arch*, that is the arch with a reduced thickness which is at the boundary of collapse. In order for this minimal arch to be computed, the elastic solution is manipulated such that it provides the position of the line of thrust at the moment of collapse. This approach is best to be explained by application onto the case study. For a geometrical safety factor of 2, the resistance is deemed sufficiently safe, as was stated in Chapter 4. This means that the thickness of the arch should be twice as big as the minimal arch.

6.3.4 Case study: Resistance against asymmetrical load configurations

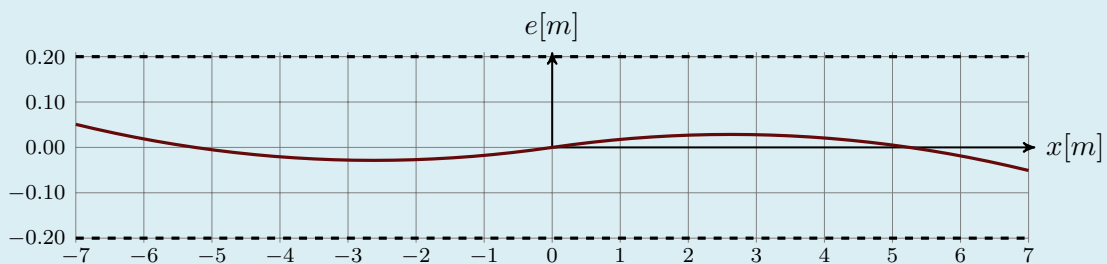
Load scenario 1 (crowd)

For TU-Delft's glass masonry bridge design, the resistance against asymmetrical load scenarios is investigated. For scenario 1, the elastic solution of the position of the line of thrust is given by expressions (6.21), (6.22), (6.23) and (6.24). The result is presented in Figure 6.21, for which the following parameters were used:

$$\begin{aligned}
 l &= 14m \\
 f &= 0.7m \\
 t &= 0.4m \\
 q_A &= 0.9q_G - 0.45q_W = 22.5t - 0.225 \quad kN/m^2 \\
 q_B &= 0.9q_G + 1.35q_T + 0.45q_W = 22.5t + 6.75 + 0.225 \quad kN/m^2
 \end{aligned}$$



(a)



(b)

Figure 6.21: Line of thrust; (a) Line of thrust in global coordinate system; (b) Line of thrust relative to the centroidal axis;

Since the line of thrust lies within the geometrical boundaries, the arch is resistant against the asymmetrical loading (i.e. it is stable). In order to quantify the resistance, the geometrical safety-factor is determined. This factor is based on the minimal thickness. To find the minimal thickness, the thickness is reduced until the line of thrust touches

the geometrical boundaries, as is done in Figure 6.22. The white planes represent the geometrical boundaries. The line of thrust is represented by the red and blue surface (domain A and B respectively). Due to a reduction of the thickness, the beneficial self-weight becomes smaller, resulting in a higher eccentricity of the line of thrust. For a thickness of 0.173m the line of thrust-surface intersects with the outer geometry.

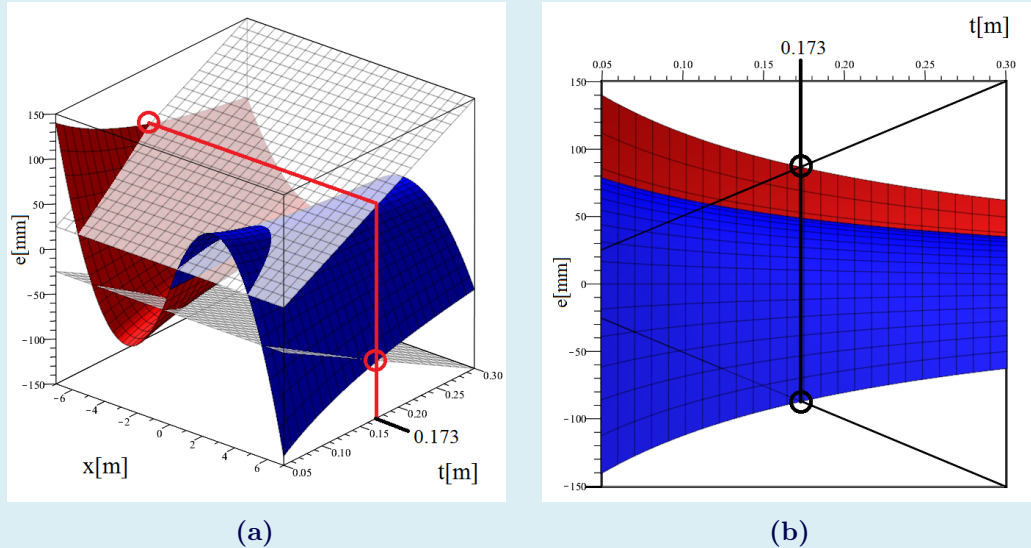


Figure 6.22: Reducing arch thickness until eccentricity of line of thrust touches the boundary (at $t = 0.173m$);

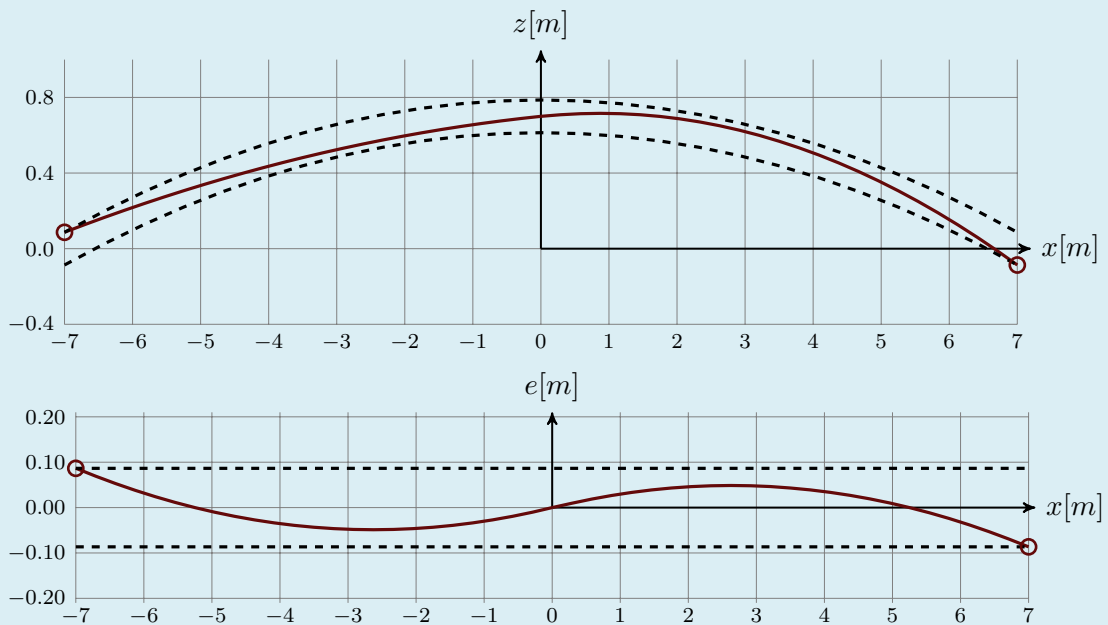


Figure 6.23: Elastic line of trust for the thickness where two hinges are formed; (top) Line of trust in global coordinate system; (bottom) Line of trust relative to the centroidal axis;

The elastic line of thrust for a thickness of 0.173m is presented in Figure 6.23. As can be observed, only two hinges are present which do not form a mechanism yet. This implies that the minimal thickness is not yet found. However for lower thicknesses the elastic solution will propagate outside the geometrical boundaries, as could be observed in Figure 6.22. Since the actual masonry behavior is plastic, this will not happen in reality. The effect of plasticity can be implemented by regarding the bi-linear M, κ -diagram illustrated in Figure 6.24.

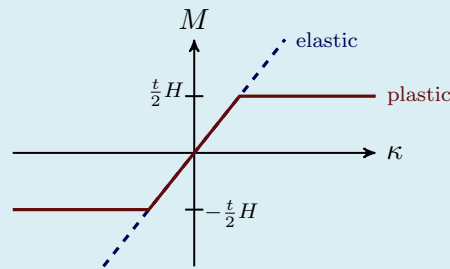


Figure 6.24: Incorporation of the plastic behavior using a bilinear M, κ -diagram;

The bi-linear plastic behavior is now implemented by fixing the position of the line of thrust at the locations of the hinges. This can be done through re-formulation of the boundary conditions. Subsequently, the thickness is reduced until the line of thrust touches the geometrical boundaries at the two additional locations. This happens for a thickness of 0.135m, as can be observed in Figure 6.25. At the sides the line of thrust follows the geometrical boundary (white plane) for all thicknesses since it is a plastic hinge.

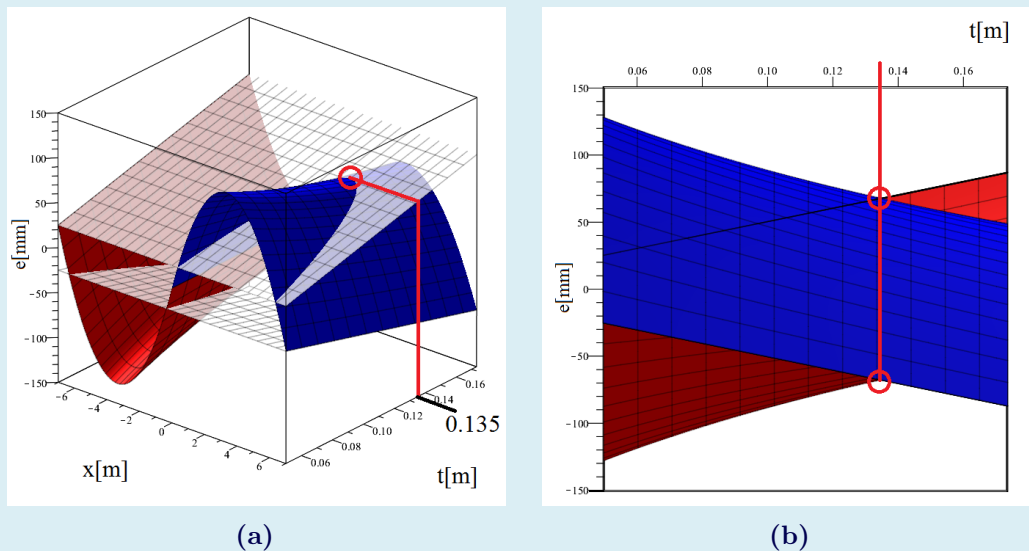


Figure 6.25: Reducing arch thickness until eccentricity of line of thrust touches the boundary at four locations (at $t = 0.135m$);

For a thickness of 0.135m, the line of thrust is illustrated in Figure 6.26. It touches at

four locations, meaning that this is the minimal arch. For the minimal arch there is only *one* possible configuration for the line of thrust. The geometrical safety-factor (GSF) is as follows:

$$GSF = \frac{0.4}{0.135} = 2.96 \geq 2 \quad \checkmark$$

This means that the resistance with respect to this load scenario is sufficiently large. The minimum design thickness is found for a safety-factor of 2, resulting in a minimal design thickness of $t=0.27\text{m}$.

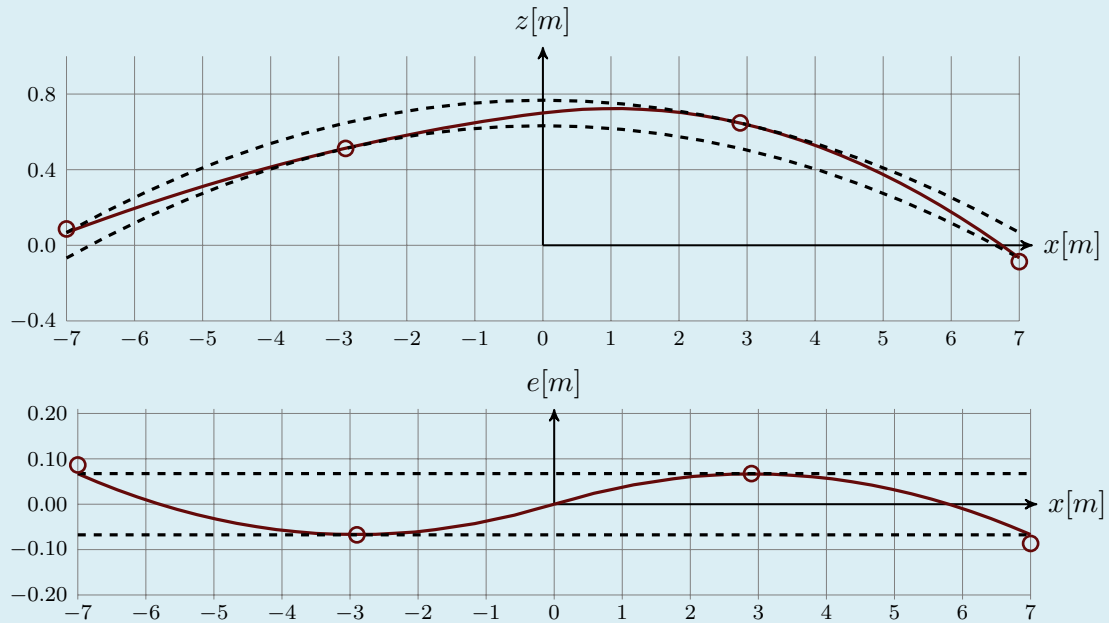


Figure 6.26: Line of trust using plastic hinges at supports, for the thickness where four-hinges occur and thus a mechanism; (top)Line of trust in global coordinate system; (bottom)Line of trust relative to the centroidal axis;

Load scenario 2 (vehicle)

Now the resistance for scenario 2 in Figure 6.18b is determined, in which an incidental service vehicle is present. First the procedure will be demonstrated for a vehicle with axle-loads at $x_{Q1} = 3$ and $x_{Q2} = 6$. Subsequently the most critical position for the vehicle is investigated. For this global stability analysis, the axle-loads will be distributed over the width of the bridge. The following loads result from the NEN-EN 1991, see Appendix B.1 (Governing load combination is LC2):

$$\begin{aligned} Q_{SV1} &= \frac{80}{2.4} = 33.33\text{kN} \\ Q_{SV2} &= \frac{40}{2.4} = 16.67\text{kN} \\ q_A &= 0.9q_G - 0.45q_W = 22.5\text{t} - 0.225\text{kN/m}^2 \\ q_B &= 0.9q_G + 0.45q_W = 22.5\text{t} + 0.225\text{kN/m}^2 \end{aligned}$$

Similar as was done for load scenario 1, the elastic position for the line of thrust is determined for a variable thickness. When reducing the thickness, intersection points between the geometry and the line of thrust are found. At these locations the boundary conditions will be adjusted, such that a plastic hinge is formed at these locations. A step by step analysis of hinge formation is shown in Figure 6.27. For every moment that a hinge is formed, the line of thrust is given in Figure 6.28.

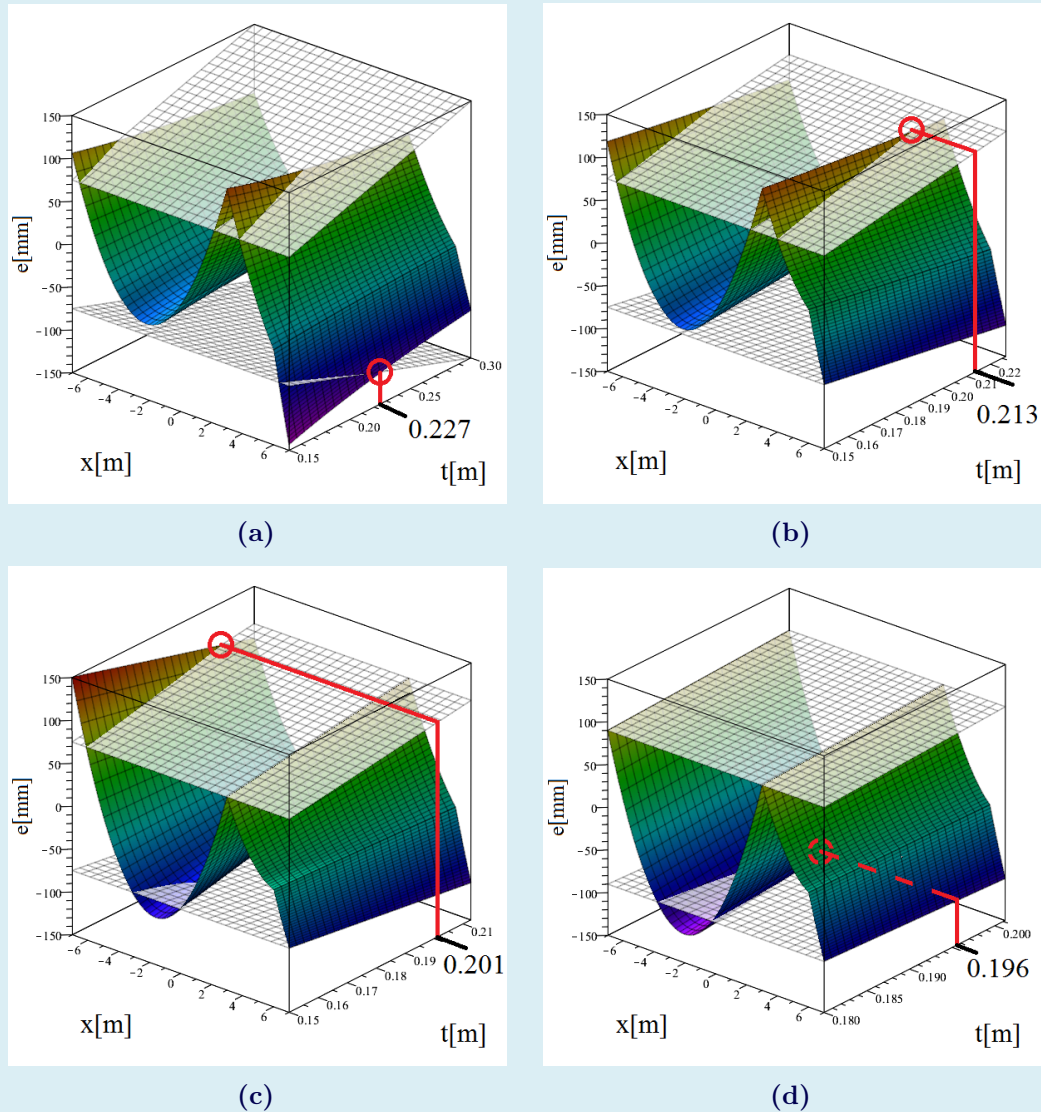


Figure 6.27: Eccentricity line of thrust for a varying arch-thickness. Note different scales for t -axis; (a) Intersection showing first hinge position at right support, whose position will now be fixed; (b) Second hinge at the location of the highest point load; (c) Third hinge at left support; (d) Intersection point providing the fourth hinge location \rightarrow minimal arch thickness is 0.196m;

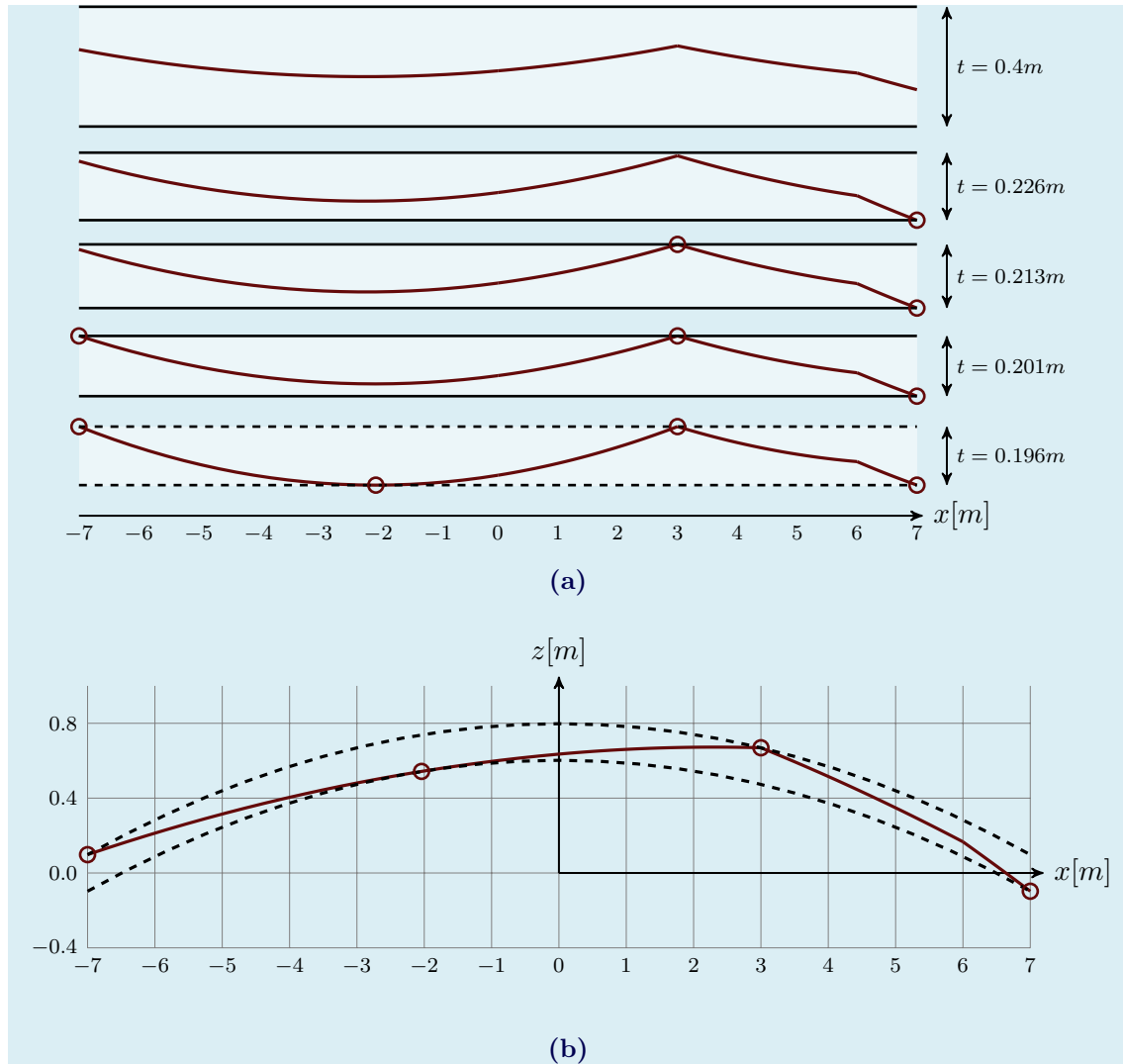


Figure 6.28: (a) Step by step reduction of thickness, showing the formation of plastic hinges until minimal thickness is obtained; (b) Minimal arch;

The minimal thickness resulting from the analysis is $t = 0.196$ (For $x_{Q1} = 3$). This analysis is now done for several positions of the vehicle. The result is provided by Figure 6.29. A slight discontinuity/dip can be observed for $x_{Q1} = 4$. At this location one of the axle-loads leaves/enters the bridge. The most critical position of the service vehicle is for $x_{Q1} = 4.5$. Note that only one axle load is present at this point. The geometrical safety factor that follows from the governing minimal thickness is:

$$t_{\text{minimal}} = 0.203m$$

$$GSF = \frac{0.4}{0.20} = 2.0 \geq 2 \quad \checkmark$$

The minimal safety factor is just reached.

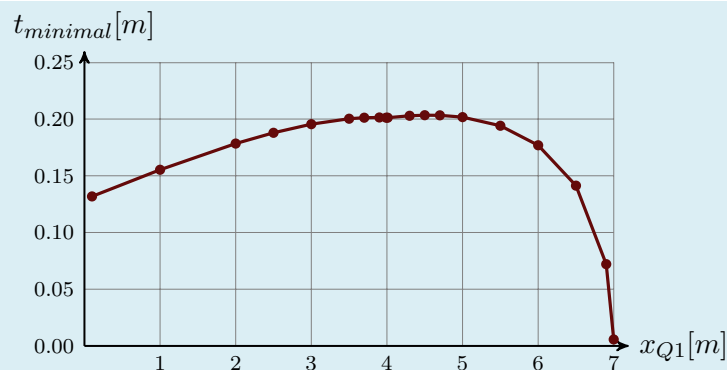


Figure 6.29: Minimal arch thickness as a function of the vehicle location (location highest axle-load (x_{Q1}));

Although the minimal safety is reached for load scenario 2, it is significantly lower than the safety factor for load scenario 1. In order to maintain the level of safety found for scenario 1, several measures could be taken:

- Increase thickness to $0.61m$
- Change max allowable axle-loads to $Q_{SV1} = 26kN$ and $Q_{SV2} = 13kN$
- Increase the width of the bridge to $3.6m$
- Apply obstacle to prevent entrance of a maintenance vehicle

Note that the axle-loads were distributed over the full width of the bridge, which is valid when assessing the global stability. Since the loads are transferred through the contact areas of the tires an additional local analysis is required, which depends on the shape and dimensions of the bricks. This aspect is not further investigated in this report.

6.3.5 Thickness design graph

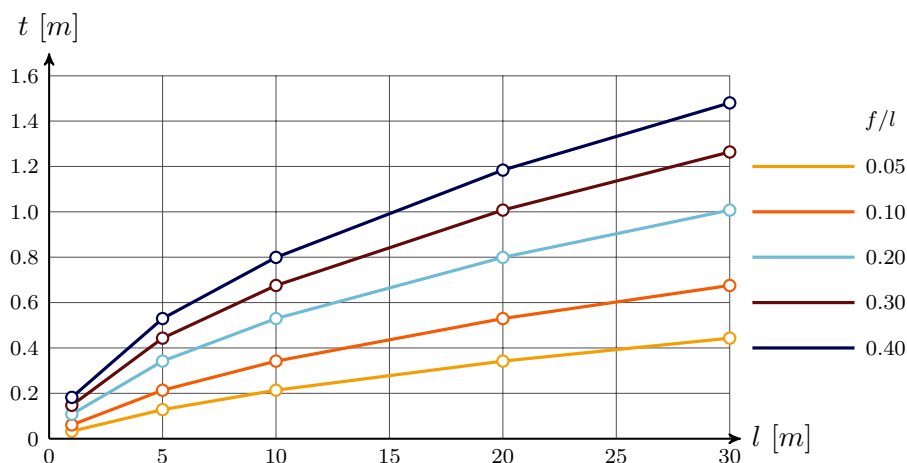


Figure 6.30: Required deck thickness as a function of the span, for several f/l -ratios; Based on a geometrical safety factor of 2 and an asymmetrical crowd-load in accordance with the NEN-EN 1991;

For design purposes it would be valuable if an estimation of the required deck-thickness could be made. Therefore for several spans and f/l -ratios, the thickness corresponding to a geometrical safety factor of 2 is computed. This is done for an asymmetrical crowd load in accordance with the NEN-EN 1991. The result is provided in Figure 6.30. For larger spans than presented in the figure, the bridge thickness becomes so thick that this support system becomes inefficient.

6.4 Results and Conclusions

6.4.1 Design diagrams

The geometrical parameters (the rise f , the thickness t and the span l), affect the stability of the arch. In order to make a well-grounded design choice for these parameters, design diagrams have been constructed.

With respect to *support settlements*, the highest stability for a certain volume of glass is achieved when the ratios t/l and f/l are chosen around the orange curve presented in Figure 6.10.

If the geometrical parameters are chosen based on different considerations, this diagram can be used to estimate the settlements for which it becomes unstable. Thereby a minimal support stiffness or maximal horizontal displacement can be formulated.

In order to determine the thickness that is required for sufficient stability under an *asymmetrical crowd load*, Figure 6.30 can be used. The loads are in accordance with the NEN-EN 1991. For spans larger than $30m$, the bridge thickness becomes so thick that the arched support system is no longer efficient.

Resulting from the geometrical parameters several categories may be distinguished, as shown in Figure 6.1 and Table 6.1. The green area indicates arches for which instability due to support-settlements is unlikely. The blue area indicates arches for which instability due to an asymmetrical load configuration is not possible. This figure can be used to assess which instability-cause(s) should be further investigated.

6.4.2 Case study analysis

For the case study both an analysis of instability due to settlements and due to an asymmetric load configuration was required. From the analysis concerning settlements, the following can be concluded:

- Instability will occur if the load increases to $69.3kN$ or if the total of the support displacements increases to $148mm$.
- The stability is sufficient, as follows from the following unity checks:

$$\frac{q_d}{q_{crit}} = \frac{19.0}{69.3} = 0.27 \leq 1 \quad \checkmark \quad \frac{u_{tot,d}}{u_{tot,collapse}} = \frac{21}{148} = 0.14 \leq 1 \quad \checkmark$$

From the analysis concerning the asymmetrical crowd- and vehicle load scenarios, the following can be concluded:

- Concerning an asymmetrical crowd load, the geometrical safety-factor is $2.96 \geq 2$, which is sufficient.
- This means that based on this scenario, the thickness could be reduced from $0.4m$ to $0.27m$.
- Concerning an asymmetrical vehicle load, the geometrical safety-factor is $2.0 \geq 2$, which is just sufficient.

Although the unity checks are sufficient, the safety for scenario 2 is significantly lower. It is recommended to apply an obstacle that prevents entrance of a maintenance vehicle, to increase the safety. This has the additional benefit that the risk that a too heavy vehicle can enter the bridge is avoided.

7 Numerical Stability Analysis

7.1 Introduction

In Chapter 6 the instability of a masonry arch was investigated, which resulted from either horizontal support movements or from an asymmetrical load configuration. However, the combination has not been investigated yet. For the case study several finite element analysis will be executed to investigate this combination. For the analytical analysis, it was assumed that the glass bricks are fully rigid, which meant that the hinges were formed at the outer boundaries of the arch (bi-linear M, κ -diagram). In reality the bricks may slightly deform, thereby distributing the opening/crack over several interfaces, rather than at the positions of the hinges only. The finite element model may thus behave slightly different, but this will presumably not have a significant effect on stability.

For the case study finite element analysis will be executed and compared to the analytical ones. Thereby the analytical methods will be validated by the FEM and vice versa. The finite element program *Diana 9.6* is used, with *midas FX+ for Diana* as a pre- and post-processor.

First a general explanation about the model and the applied procedures is provided by Section 7.2. A description of the applied elements is given, the types of non-linearity are discussed and the iterative procedure is briefly explained. In Section 7.3 the displacements that occur in the symmetrical load scenario (including support settlements) will be compared. In this section the support-settlements will then be increased until divergence occurs. Divergence could mean either instability or inadequate modeling. It is investigated which iterative method and load-step sizes are adequate to assure that divergence corresponds to instability. In Section 7.4 the line of thrusts for the asymmetrical load scenario resulting from the analytical and FEM-analysis will be compared, thereby validating one another.

Now that the adequate functioning of the finite element model is established, a *combination* of an asymmetrical load scenario with support settlements is made in Section 7.5. Note that for this combination no analytical solution is available.

For local stress reduction it may be necessary to apply a resilient intermediate material between the glass bricks, as will be elaborated upon in Chapter 8. This would also affect the stiffness and thus stability. In Section 7.6 it is investigated what the *minimal stiffness of the interlayer* should be to guarantee its stability.

7.2 General model description

This section briefly describes the model and the elements that were used. Subsequently it is explained which types of non-linearity were taken into account, how this was done and why.

7.2.1 Model overview

Figure 7.1 shows the mesh that serves as a base for all the analysis in this chapter. As indicated, four components can be distinguished. Both the glass and the stiff support block are modeled using plane stress elements (with different material properties). To model the force transfer from brick to brick, interface elements are applied every $0.1m$. At the glass-to-support transition, an interface is applied as well.

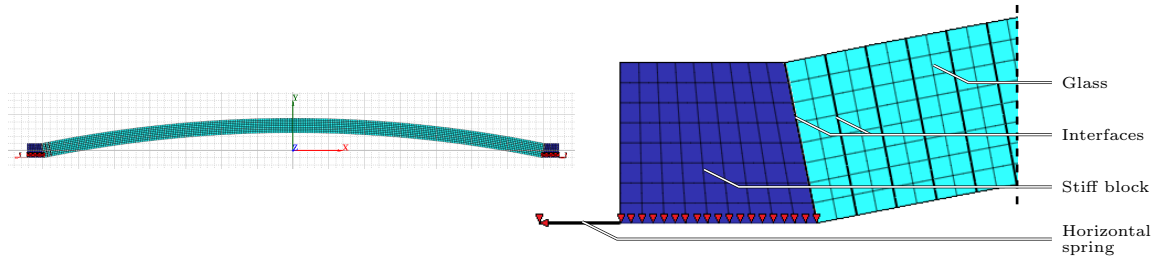


Figure 7.1: Overview of the finite element model, showing the mesh and the components that were used; The mesh-size is $0.05m \times 0.05m$; The red arrows indicate the direction in which the nodes are constraint;

The horizontal support reactions will lead to support movements depending on the abutment-soil interaction. This effect is implemented using translational springs with a stiffness that is based on the response of the abutments ($k = 4.8 \cdot 10^4 kN/m$). The material properties that were assigned are provided by Table 7.1.

Table 7.1: Material properties used in the FEM;

	Unit	Glass	Stiff material
Young's modulus	GPa	70	70000
Poisson's ratio	—	0.2	0.2
Thermal expansion coefficient	$10^{-6} K^{-1}$	9.0	0.0
Mass density	$kN/m^3/g$	2.5	10^{-6}

	Unit	Interface
Normal stiffness modulus	kN/m^3	$7 \cdot 10^{11}$
Shear stiffness modulus	kN/m^3	$7 \cdot 10^{11}$
Tensile strength	kN/m^2	10^{-8}
Interface non-linearities		Discrete cracking
Mode-I Model		Brittle
Mode-II Model		Brittle

An overview of the elements that were used is presented in Figure 7.2. Since non-linear analyses will be executed, higher order elements are used. Linearly interpolated elements would be more susceptible for the occurrence of spurious kinematic modes.

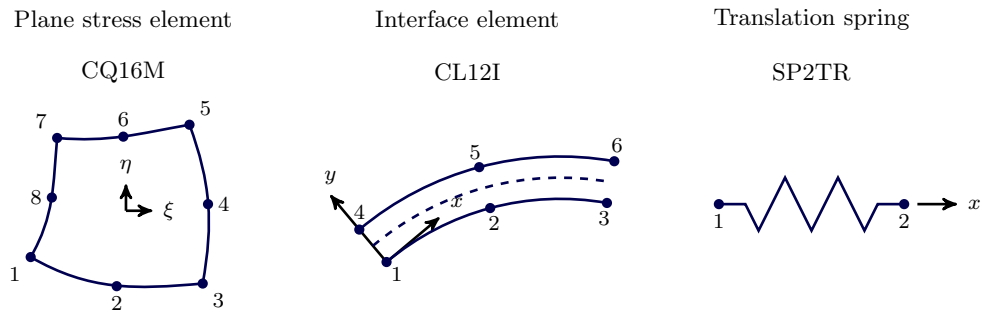


Figure 7.2: Topology of the elements used in the finite element models, taken from Diana user's manual;

7.2.2 Non-linearity

Physically non-linear

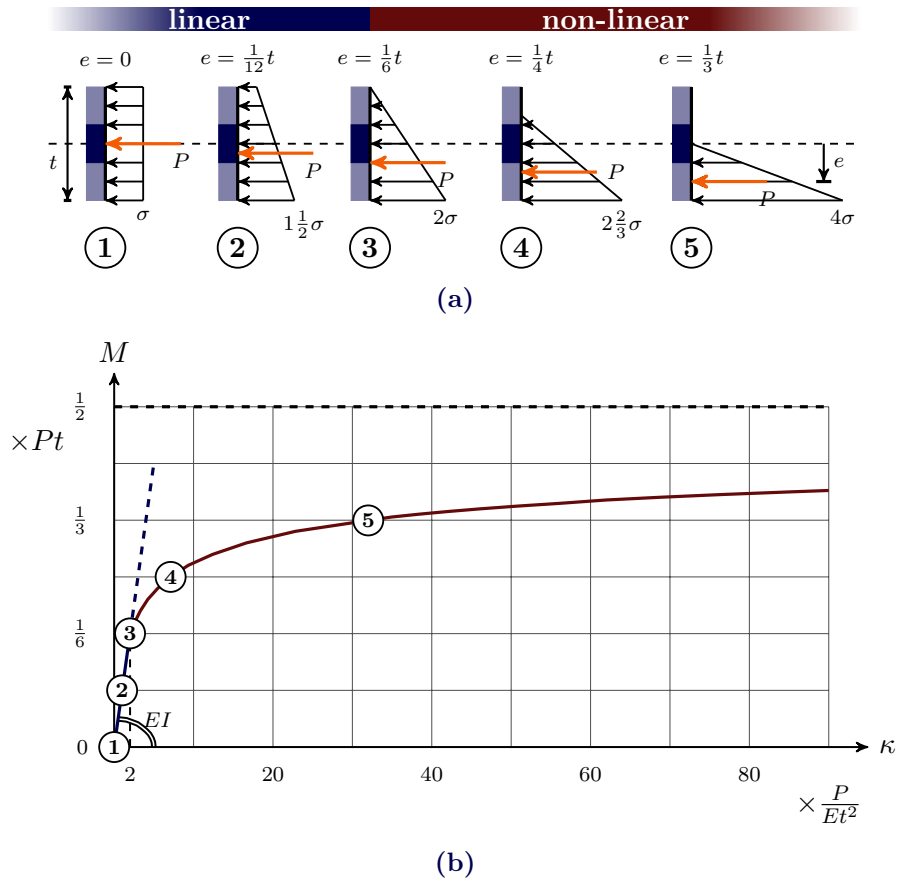


Figure 7.3: (a) Stress distribution as a result of the zero tension brittle diagram; (b) Corresponding M, κ -diagram;

Since the masonry arch is only able to transfer compressive stresses, the interface between two bricks behaves physically non-linear. This effect is implemented in the model by assigning *brittle* behavior to Mode-I (opening mode), meaning that no stresses can be

transferred once the tensile strength is exceeded (neither normal stresses nor shear). Since there is no tensile capacity, the tensile capacity is zero. A value that approximates zero is chosen $f_t = 1.0 \cdot 10^{-11} N/mm^2$, to assure that the interface remains intact if no stress is present yet.

Due to the zero tension brittle behavior, the stress distribution presented in Figure 7.3a can be expected. For the non-linear part, the moment of inertia has a reduced height. The following expression can be derived:

$$I_{nonlin} = \frac{1}{12} b \left[3 \left(\frac{1}{2} t - |e| \right) \right]^3 \quad \text{for} \quad e \in \left[-\frac{1}{2} t, -\frac{1}{6} t \right] \text{ and } \left[\frac{1}{6} t, \frac{1}{2} t \right]$$

Using this expression, the relation between the curvature and the moment can be derived:

$$\kappa_{nonlin} = \frac{M_{nonlin}}{EI_{nonlin}} = \left(\frac{e}{\frac{1}{12} (3(\frac{1}{2} - e))^3} \right) \frac{P}{Et^2}$$

This expression is used to construct the M, κ -diagram, presented in Figure 7.3b.

Geometrically non-linear

Without considering the geometrical non-linear behavior, the capacity of a flat arch may be seriously overestimated. Support settlements decrease the rise of the arch, which increases the horizontal support reactions. Since the support movements are load-dependent, a softening behavior can be expected. For a certain critical load, a snap-through failure will occur. Through application of the horizontal springs, the load-dependent behavior is incorporated. The stiffness results from the abutment-soil system. Axial deformations amplify the geometrical non-linear behavior.

Iterative procedure for non-linear behavior

For the non-linear analyses, the regular Newton Raphson method is used, which is illustrated in Figure 7.4. For every iteration a new stiffness matrix is set up. Therefore only a few iterations will be necessary to converge to the solution. However, every iteration is relatively time-consuming.

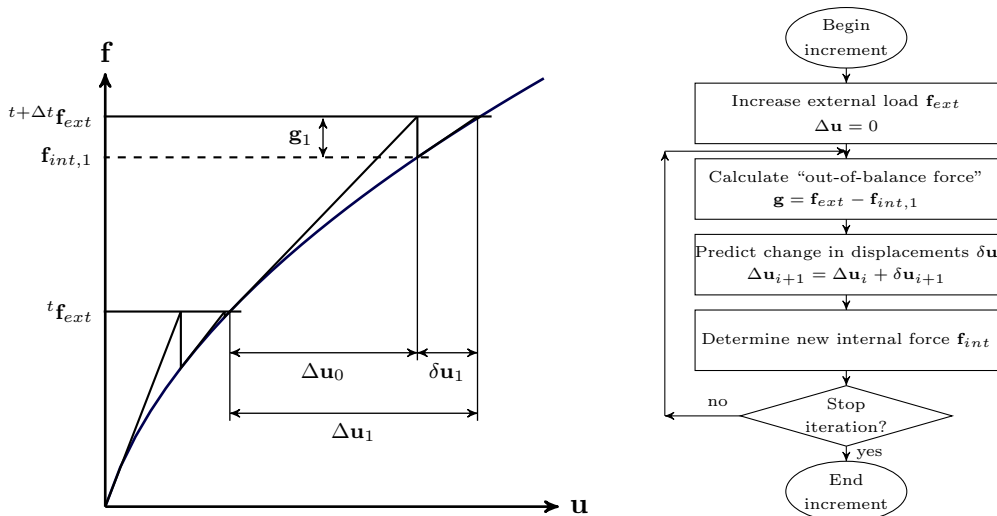


Figure 7.4: Regular Newton Raphson method, taken from Diana user's manual;

To perform the non-linear analysis, step-sizes are defined to apply the load. The size of the *load*-steps is 10% of the total load. This holds for the gravity, traffic and wind-load. To apply the temperature load, a time-dependent temperature function has to be defined. Over a period of 10 seconds the total temperature load is applied using *time*-steps of 1 second.

7.3 Support displacements

7.3.1 Symmetrical load scenario

For the symmetrical load scenario, the result of the geometrically- and physically non-linear FEM analysis is presented in Figure 7.5. The stress distribution that can be observed, is in line with the expected position of the line of thrust.

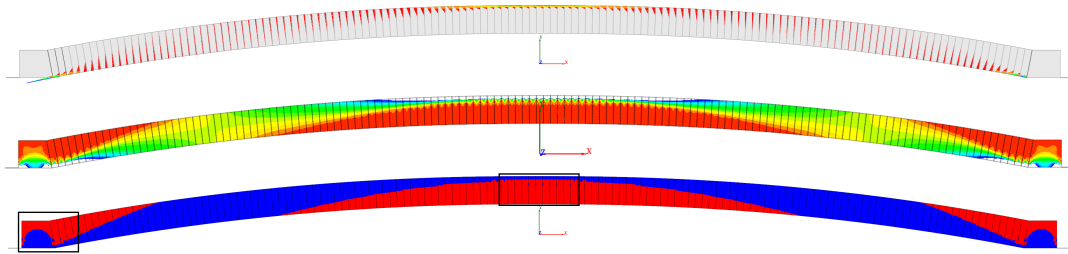


Figure 7.5: Result of non-linear finite element analysis, for the symmetrical load scenario ($q_d = 19.0 \text{ kN/m}^2$ and $\Delta T_N = -12.15^\circ \text{C}$); (top) Stress perpendicular to interface; (middle) Contour plot of principal compressive stresses between 0 and -5 N/mm^2 ; In the white areas the compressive stresses are bigger; (bottom) Stress in x-direction, where blue is compression and red is inactive;

It is expected that hinges are formed at the supports and in the top middle. At these positions a crack or opening between the bricks is expected. A slightly different behavior follows from the finite element analysis, as presented in Figure 7.6.

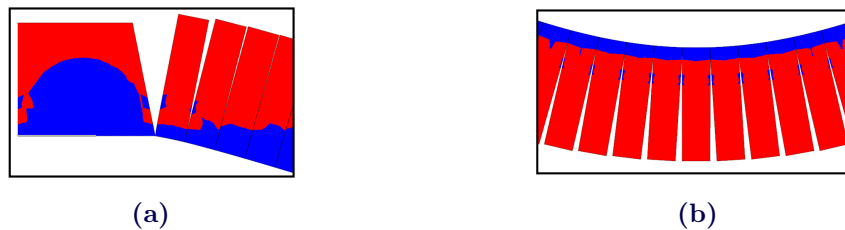


Figure 7.6: Details showing the crack distribution [deformations exaggerated by a factor 50]; (a) At the support; (b) At midspan;

The ‘crack’ distribution can be explained through the position of the line of thrust and the M, κ -diagram, as illustrated in Figure 7.7. The stiffness of the bricks is high but not infinite, therefore the bricks will deform as the line of thrust approaches the outer geometry. In the top of the arch, the line of thrust is tangent to the outer geometry and therefore the eccentricity at the surrounding bricks is about the same. This results in a number of consecutive openings with approximately the same rotation. At the supports this does

not hold. Since the line of thrust ‘departs’ under an angle, there is a large difference in eccentricity when comparing to adjacent interfaces. Therefore the rotation is mainly concentrated in the first opening.

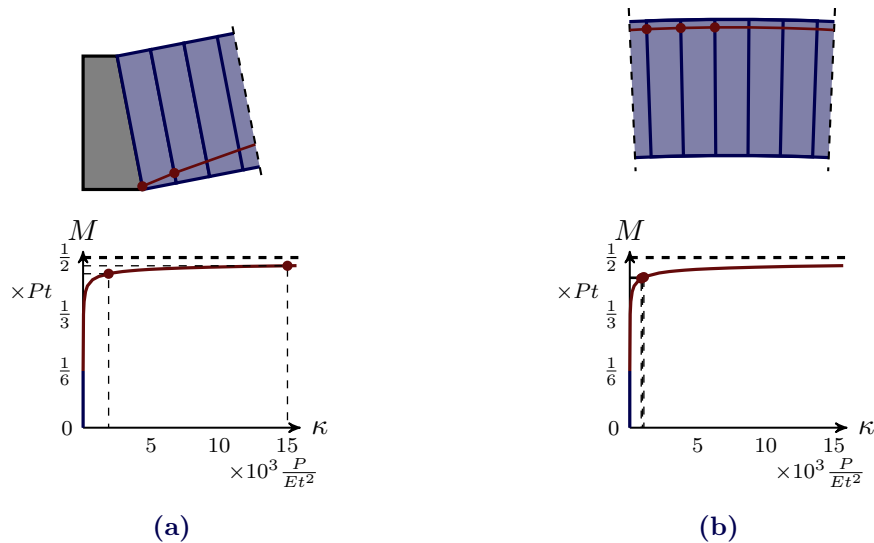


Figure 7.7: Explanation of the crack-distribution; (a)At the support; (b)At midspan; Note: The M, κ -diagram was derived in Section 7.2;

In the finite element model the sag of the top is 66.4mm , where analytically 69.6mm is found. The finite element model behaves slightly less stiff (larger deflection). Most likely this can be attributed to a higher axial deformation, as a result of the reduced contact area. This was not implemented in the analytical model. However, the difference is less than 5%, which means that the analytical- and numerical-analysis sufficiently correlate.

7.3.2 Imposed displacements at instability

Since the non-linear analysis converged to a solution, given the assumed boundary conditions, the structure can be considered stable for this load-scenario. However to investigate how susceptible the stability is to additional linear-imposed displacements, additional support-displacements are applied, until the analysis diverges. If divergence occurs, this does not necessarily mean that the structure is unstable. It could also be that the load steps are too high or the used iterative method is not adequate. To assure that divergence occurs because of instability and not due to an improper analysis, the solution for various load-steps is compared to the analytical solution found in Chapter 6 (Figure 6.16). The result is presented in Figure 7.8. At the supports, the interfaces are practically completely opened before additional support displacements are applied. To reduce the complexity of the model, in these analyses, the horizontal springs and vertical constraints are directly applied onto the bottom of the outer glass bricks.

It follows that for load steps of 2mm , the non-linear analysis does not provide an adequate result, in particular when the applied loads are low. For a load step of 0.2mm , the FEM-solution follows the trend of the analytical solution. Reducing the load-steps to 0.02mm does not significantly affect the result. Although the trend of the analytical solution is followed, the total displacement at collapse is underestimated by approximately 20%. This can most likely be attributed to the softening of the structure’s response, which becomes

too high as the critical displacement is approached. Different iterative procedures (i.e. Modified Newton Raphson and Quasi-Newton) have been tried as well, but these provided worse results.

For the considered symmetrical load scenario, where $q_d = 19kN/m$, a linear displacement (permanent settlement) of $93mm$ can occur before the arch will become unstable. The allowed linear displacement is lower, since a certain safety factor should be applied. This is in addition to expected non-linear displacement resulting from the support stiffness.

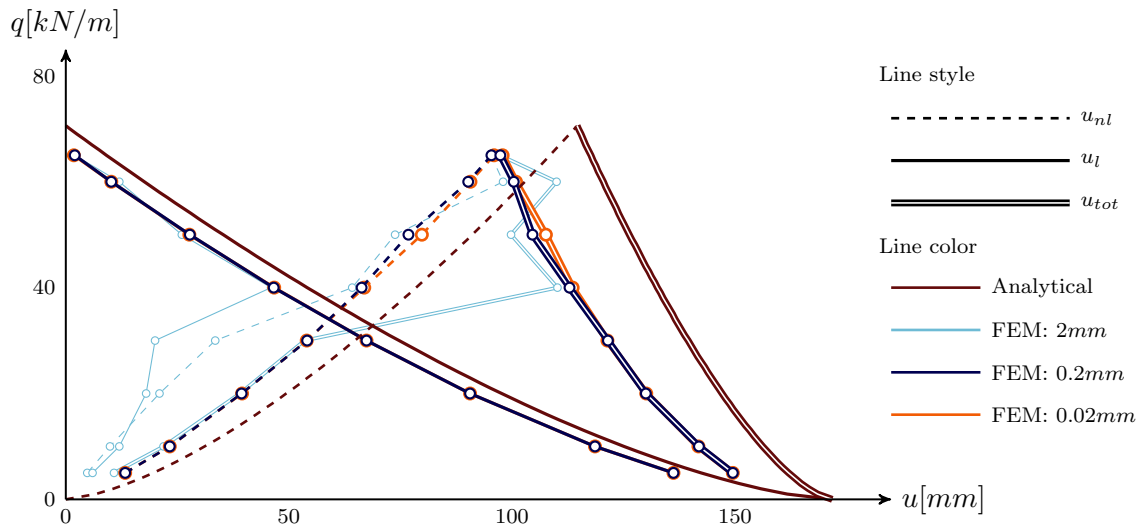


Figure 7.8: Displacements at the boundary of instability, comparing the analytical solution to the numerical one, for different load steps: 2mm, 0.2mm and 0.02mm; Note: For each combination of the 3 load-steps and the eight values for q_d a FEM-analysis has been executed. Each analysis provides 3 point in this diagram: One for each graph (i.e. the graphs of u_l , u_{nl} and u_{tot});

For the asymmetrical load scenario, there is no analytical solution available to provide the total displacement at the moment of collapse. This value will be approached using the Regular Newton Raphson method with load steps of $0.2mm$. From the above analysis it follows that this will provide accurate results. Smaller load-steps do not provide a significantly better result and have a significantly larger computational time. Considering $0.2mm$ versus $0.02mm$, the computational time is approximately 6 minutes versus 1 hour respectively.

7.4 Asymmetric load scenario

Before performing the non-linear analysis for the asymmetrical load scenario, a structurally linear analysis is performed. This linear analysis can be compared to the elastic solution which was found analytically. To assess the effect of the asymmetrical load only, displacements and axial deformations were excluded in the analytical analysis. In order to do the same in the finite element model, a support displacement is applied to compensate for the axial shortening. Note that the axial deformation must be excluded without affecting the bending stiffness, therefore it is not possible to manipulate the variables E or A . The total support displacement that is applied on each side was determined using the following expression:

$$u = \frac{Hl}{EA} \quad \text{where} \quad H = \frac{ql^2}{8f}$$

In Figure 7.9 it can be observed that after compensation of the axial shortening the stress distribution shown in the cross sections are approximately constant. This means there is no eccentricity of the line of thrust, as would result from an analytical analysis in which the axial shortening is excluded.

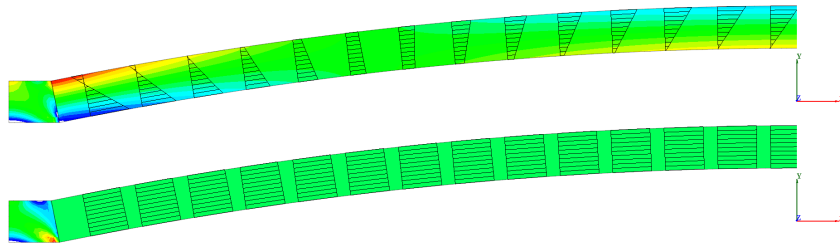


Figure 7.9: Stress distribution (σ_{xx}) under a gravity load; (top) With axial deformation; (bottom) Including a support displacement to compensate for the axial deformation;

For scenario 1, in which an asymmetric crowd load is present, the same procedure is executed. The expression for the horizontal support reaction corresponding to this load scenario is used:

$$H = \frac{(q_A + q_B)l^2}{16f} \quad \rightarrow \quad H = 433kN \quad \rightarrow \quad u = 0.216mm$$

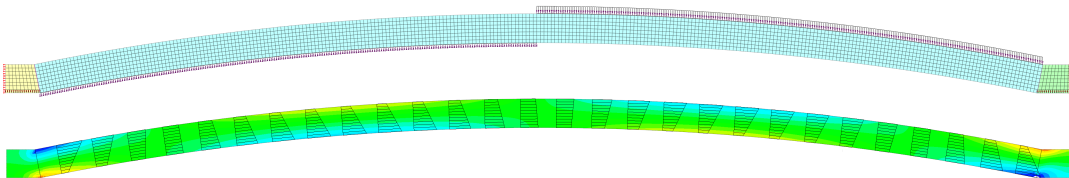


Figure 7.10: Principal compression stress distribution for the asymmetric load scenario, in which the axial shortening is compensated by a support displacement;

The stress distribution following from this analysis is shown in Figure 7.10. In order to extract the line of thrust from the results, the data from the top and bottom nodes is post processed, using Figure 7.11 and the following equations:

$$\begin{aligned}
 x &= \frac{x_{top} + x_{bot}}{2} \\
 y &= \frac{y_{top} + y_{bot}}{2} \\
 \sigma_{avg} &= \frac{\sigma_{top} + \sigma_{bot}}{2} \\
 \sigma_m &= \sigma_{top} - \sigma_{avg} \\
 e &= \frac{M}{P} = \frac{\sigma_m \cdot W}{\sigma_{avg} \cdot A} = \frac{\sigma_m}{\sigma_{avg}} \frac{t}{6}
 \end{aligned}$$

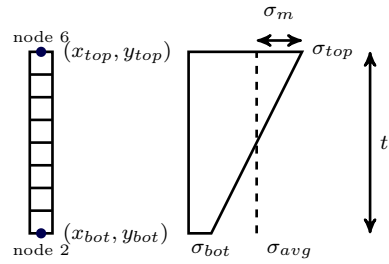
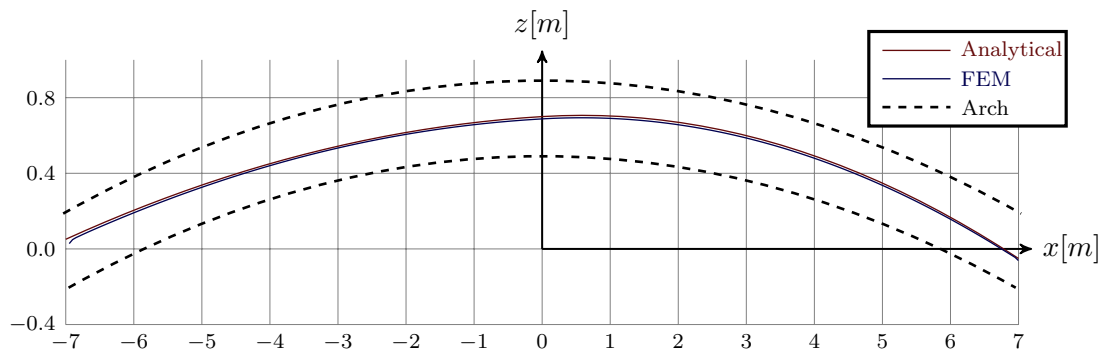
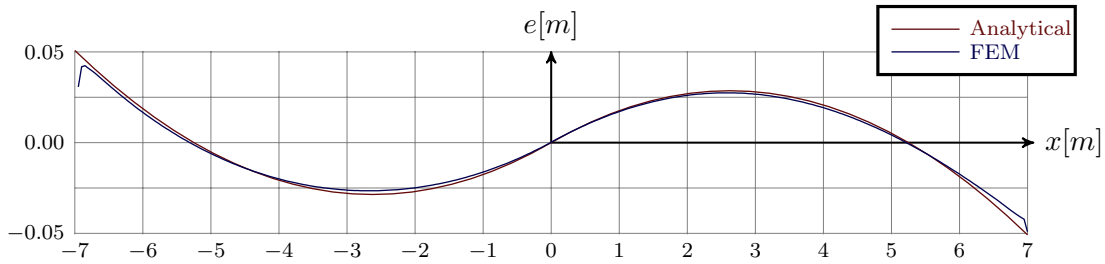


Figure 7.11: Post processing: stress distribution → line of thrust;

In Figure 7.12 it can be observed that the lines of thrust highly correlate. Therefore the finite element model functions adequately and a non-linear analysis can now be executed.



(a)



(b)

Figure 7.12: Line of thrust; (a)Line of thrust in global coordinate system; (b)Line of thrust relative to the centroidal axis;

7.5 Combination: Asymmetric and support displacements

It has now been established that the response of the finite element model to the asymmetrical load scenario corresponds to the analytical prediction, when *excluding* support movements and axial deformations. The next step is to determine the behavior when these aspects are *included*. Therefore a non-linear analysis is executed for load scenario 1. The result is presented in Figure 7.13. Since the analysis converged, it can be stated that the structure is stable. The stress distribution indicates the position of the line of thrust. The location where the line of thrust is closest to the extrados, has shifted towards the side on which the crowd load is applied.

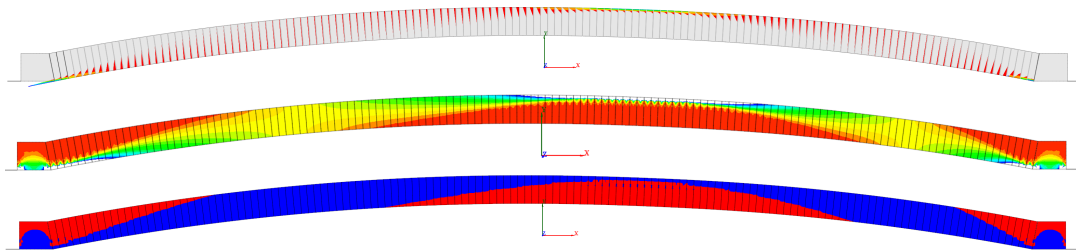


Figure 7.13: Result of non-linear finite element analysis, for asymmetrical load scenario 1, in which the horizontal support stiffness is implemented; (top) Stress perpendicular to interface; (middle) Contour plot of principal compressive stresses between 0 and -5N/mm^2 ; In the white areas the compressive stresses are bigger; (bottom) Stress in x-direction, where blue is compression and red is inactive;

The total displacement of the supports is 15.3mm . Additional displacements are now applied until the analysis diverges and the structure becomes unstable. The additional displacement is applied in steps of 0.2mm , as was decided in section 7.3. However, after a total displacement of 26.4mm the analysis diverges, which is lower than expected. Therefore a second analysis is done, in which the smaller load-steps of 0.02mm are applied. The total displacement when the model diverges is now 71.4mm , which most likely approaches the value for which the arch becomes unstable.

7.6 Reduced interface stiffness

In Chapter 8, it is proposed to limit the stress concentrations in the glass bricks, by application of a resilient intermediate material. In anticipation of this chapter, the effect of this measure on the stability is assessed. To do so it is investigated how the deflection develops, as the interface-stiffness reduces. Figure 7.14 shows the increasing deflection for both the symmetrical and asymmetrical load scenario.

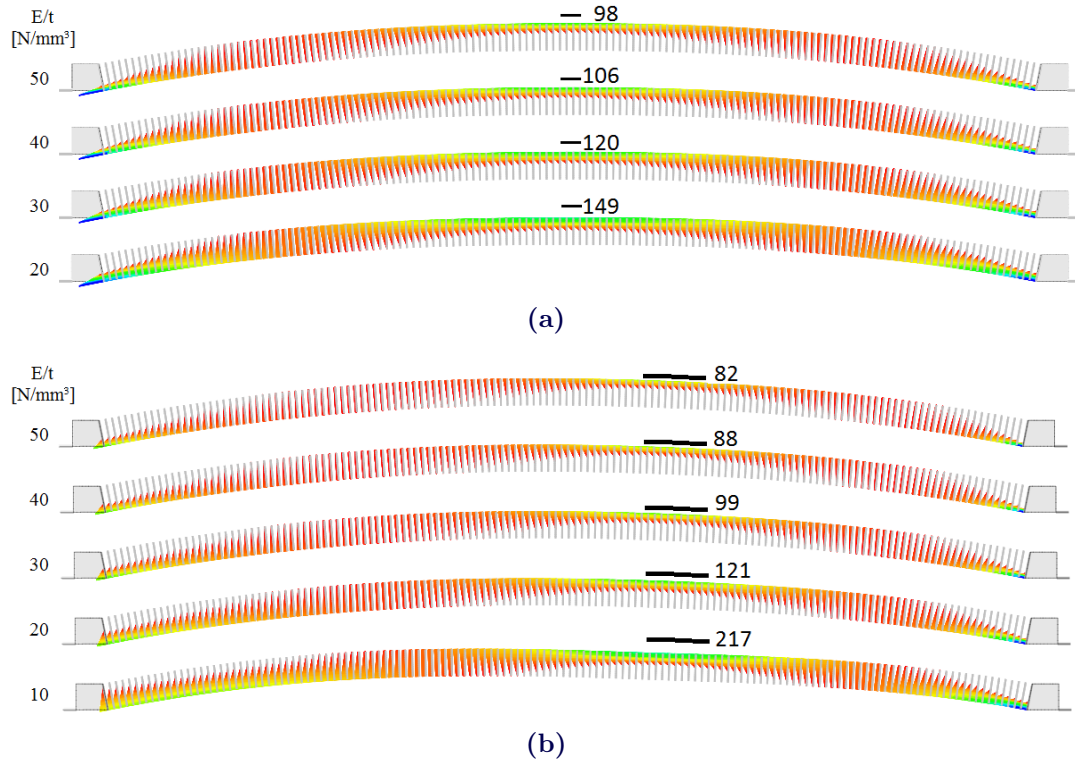


Figure 7.14: Effect of a reduced interface stiffness: The stress is distributed better (see triangular stress distribution at the support), but vertical deflections increase and the stability decreases; Note: color-scale is different for each model; Deflections in mm (a) Symmetrical load scenario; (b) Asymmetrical load scenario;

In Figure 7.15 it can be observed that for the considered load scenarios, the arch becomes unstable around $E_{int}/t_{int} = 10 N/mm^3$. For the arch to be sufficiently stable, it is proposed to limit the vertical deflections to two times the deflection that could be expected for an infinitely stiff interface. This results in a minimal interface-stiffness of $26 N/mm^3$. The symmetrical load scenario is governing in this case, which can be attributed to a higher total applied load, resulting in larger support movements.

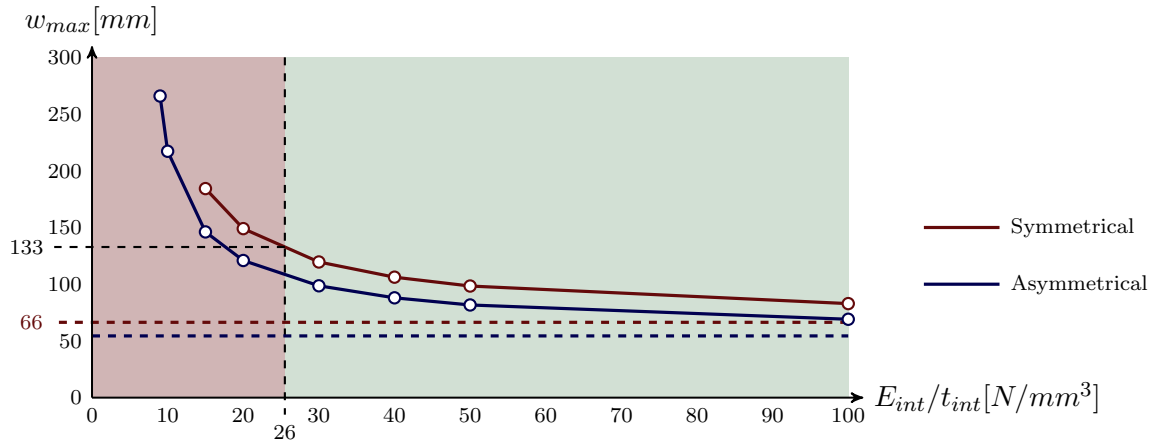


Figure 7.15: Maximum deflection depending on the interface-stiffness (dashed lines indicate vertical deflections for $E_{int}/t_{int} \Rightarrow \infty$);

For completion it is investigated how the interface stiffness reduction affects the maximum occurring stresses and the eccentricity of the line of thrust. In order to obtain accurate results, the mesh has been refined at the locations where the maximum stress occurs, as shown in Figure 7.16. The results are provided by Table 7.2.

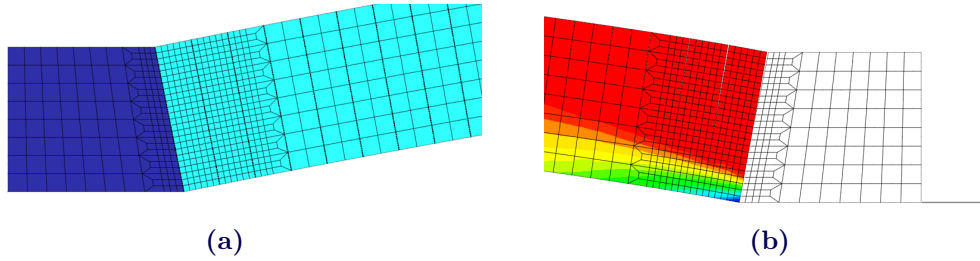


Figure 7.16: (a) Mesh-refinement at the location where the highest stresses occur; (b) Principle compressive stress plot for asymmetrical scenario and $E_{int}/t_{int} = 20 \text{ N/mm}^3$;

Table 7.2: The maxima of the deflection, eccentricity, compressive stress in interface and principal compressive stress in the glass;

Interface stiffness E_{int}/t_{int} [N/mm^3]	w_{max} [mm]		e/t [-]		$\sigma_{int,max}$ [N/mm^2]		$\sigma_{princ,comp,max}$ [N/mm^2]	
	Sym.	Asym.	Sym.	Asym.	Sym.	Asym.	Sym.	Asym.
$\rightarrow \infty$	66	54	-	-	-	-	-	-
200	75	62	0.478	0.479	35.8	37.0	36.2	36.9
100	83	69	0.465	0.472	24.4	26.4	24.2	26.3
50	98	82	0.449	0.464	16.5	18.9	16.5	18.7
40	106	88	0.442	0.458	14.6	16.9	14.5	16.8
30	120	99	0.431	0.453	12.5	14.8	12.4	14.7
20	149	121	0.408	0.439	10.1	12.5	10.1	12.3
15	184	146	0.389	0.430	8.7	11.2	8.7	11.1
10	-	217	-	0.414	-	10.0	-	9.9
9	-	266	-	0.403	-	9.9	-	9.8

It follows that the maximum principal compressive stress corresponds to the maximum stress in the interface. Figure 7.17 shows that for a lower interface-stiffness the maximum stress is lower as well, which can be attributed to a better stress-distribution. If the interface stiffness becomes too high, so will the stresses. Establishing a maximum stiffness however is rather difficult, since glass typically fails in tension and not in compression. Chapter 8 will elaborate on this topic, in order to find a maximum for the interface stiffness, which ensures that the capacity will not be exceeded.

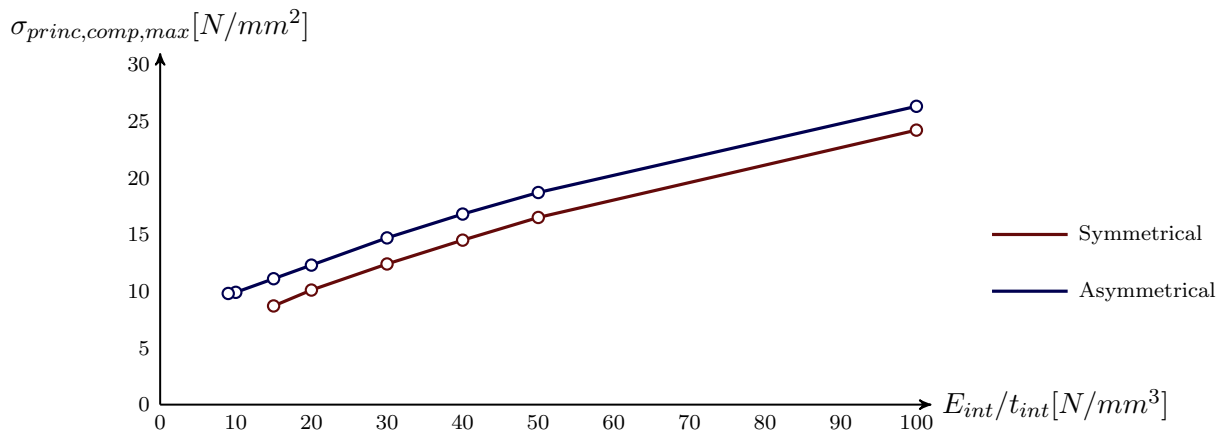


Figure 7.17: Maximum principal compression strength depending on the interface-stiffness;

7.7 Conclusions

7.7.1 On Validation

From the *non-linear* FEM-analysis it follows that the maximum sag is 66.4mm for the *symmetrical load scenario*, where analytically 69.6mm is found. The difference is less than 5%, which means that the analytical and FEM-analysis sufficiently correlate. An additional linear displacement (permanent settlement) of 93mm can be applied before instability occurs, which approaches the 100mm that was found analytically. Most likely the numerical procedure is unable to follow the significantly softening response of the structure as the instability-boundary is approached. Therefore a slightly lower value is found.

The lines of thrust that are found for the *linear* analysis of the *asymmetrical load* scenario almost perfectly correlate, which establishes that the model functions adequately.

7.7.2 Non-linear analysis method

For a non-linear analysis in which instability is approached, the Regular Newton-Raphson method with load steps of 0.2mm is best to be used. Smaller load-steps do not provide a significantly more accurate result, whereas the analysis-time significantly increases.

7.7.3 Combination

For the non-linear analysis of the asymmetrical load scenario (for which no analytical solution is available) an additional linear displacement (permanent settlement) of 71.4mm can be applied before instability occurs. This means that this it is more critical than the symmetrical load scenario.

7.7.4 Interlayer-stiffness

When applying a resilient intermediate material between the glass bricks, the stability reduces. In order to assure sufficient stability, the interface stiffness E_{int}/t_{int} , should be higher than $26\text{N}/\text{mm}^3$. In this case the symmetrical load scenario is governing, which can be attributed to the higher axial force that causes larger interlayer deformations.

7.7.5 General conclusions

For the finite element models in this chapter, the geometry and boundary conditions of TU Delft's glass masonry bridge were used. Although these models can not be used for other designs, they confirm the validity of the analytical methods provided in Chapter 6. The formulated minimal interlayer-stiffness does not hold in general. For other designs this value may be different, dependent on the geometry, boundary condition and number of interlayers (i.e. for bigger brick sizes, the number of interlayers will be less).

IV Analytical and Experimental Stress Analysis

8	Glass in compression	103
8.1	Introduction	103
8.2	Tensile stress due to global effect 105	
8.3	Tensile stress due to local effect	109
8.4	Interlayer-material selection ..	110
8.5	Conclusions	111
9	Experimental research	113
9.1	Introduction	113
9.2	Stacked glass-interlayer system	114
9.3	Glass arch scale test	123

8 Glass in compression

8.1 Introduction

8.1.1 Introduction

As was shown in Chapter 5, the compressive strength of glass far exceeds the flaw-reduced tensile strength. Therefore when a sheet of glass is loaded in bending, failure will always be due to an exceeded tensile strength around a defect. But how does a non-slender glass brick fail when in compression? Figure 8.1 shows a glass brick that is uni-axially loaded by an evenly distributed compressive stress. No lateral stresses are introduced, and thus no tensile stresses will occur. At some point the brick will fail, which implies that the compression strength may be exceeded. However in practice tensile stresses will always be introduced due to (slight) imperfect conditions. Therefore the glass will always fail due to a tensile stress, even when loaded in compression.

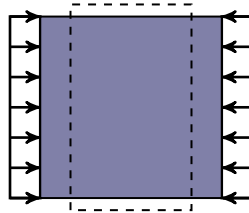


Figure 8.1: Glass brick in compression; Lateral strain but no tensile stresses;

For a glass brick within an arched masonry bridge configuration, tensile stresses will mainly result from two effects:

Global effect: Discontinuous stress-distribution due to eccentricity of the line of thrust.

Local effect: Peak stresses due to imperfect flatness glass.

In conventional stone masonry arches, stability is deemed to be the governing structural criteria. The strength criteria is usually met, since the expected *average stresses* are low compared to the ultimate strength (as was explained in Chapter 4). Local cracking can occur, but this does not necessarily result in total collapse of the structure.

Even though residual capacity may still be present after cracking, it will have a negative effect on the capacity. Too many cracked bricks compromise the safety of the bridge. Hence it is best to prevent cracking. The importance of crack-prevention is amplified by considering the aesthetics and the user-experienced safety, that is related to transparent constructions. In order to prevent cracking both the global effect and local effect are investigated. It is shown how an interlayer can be used to limit these effects.

8.1.2 Global effect

The global effect is that the eccentricity of the line of thrust causes a triangular stress distribution on a part of the brick, as shown in Figure 8.2. In Section 8.2 it is examined how the maximum occurring tensile stress relates to this effect. It answers the following question: *How does the maximum tensile stress relate to the brick dimensions and the eccentricity of the line of thrust?*

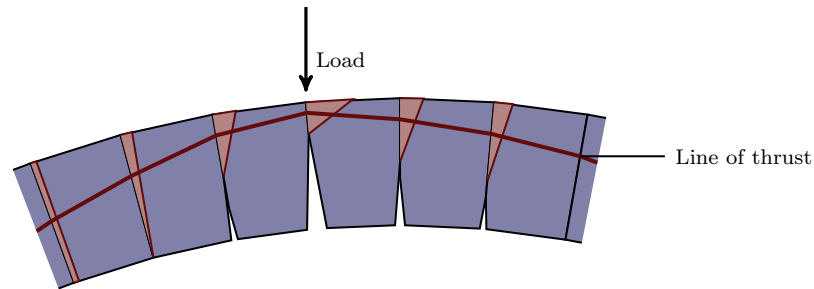


Figure 8.2: Stress concentrations due to global effect: eccentricity of the line of thrust;

8.1.3 Local effect

The local effect concerns a limited contact area between bricks due to imperfections, as illustrated in Figure 8.3. Since the bricks are rather stiff, the contact area may be limited to a few points only. This results into relatively high stresses and possible cracking. Traditionally this problem is solved by application of a mortar. Due to the mortar the full area is in contact, assuring that the stresses are distributed.

Application of a mortar is not always necessary. A so-called ‘dry stack’ can be made if the average stresses and thus the stress concentrations are sufficiently small. Quantifying the stress concentrations that occur in a dry stack is rather hard. It depends on small scale brick-imperfections, which may be distributed randomly and vary in magnitude. Therefore the limitations for a dry stack can only be accurately determined experimentally.

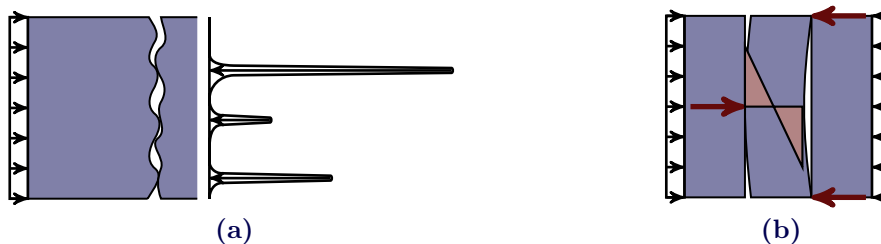


Figure 8.3: Stress concentrations due to local phenomenon; (a) Peak stresses due to random irregularities; (b) Stress concentration due to overall brick imperfection;

Section 8.3 addresses the local effect. A mortar or resilient interlayer redistributes the stresses. In this section a method is proposed that establishes the maximum stiffness of a resilient interlayer in order to distribute the peak stresses due to random irregularities adequately. The overall brick imperfection is not regarded, since it can be prevented (e.g. by post-processing of the bricks). It answers the following question: *How to formulate the maximum interlayer-stiffness, to assure adequate stress transfer between bricks?*

8.2 Tensile stress due to global effect

A brick within a masonry arched support system is loaded by compression only. If the line of thrust has a certain eccentricity, the typical triangular stress distribution shown in Figure 8.4 will introduce tensile stresses. The maximum occurring principal tensile stress depends on the axial force P , the eccentricity of the line of thrust e and the brick dimensions t and T . The following research questions are formulated:

- For which aspect-ratio of the bricks (T/t) is the occurring tensile stress the lowest?
- Given the maximum axial force, brick dimensions and maximum allowable tensile stress, what is the maximum allowable eccentricity?

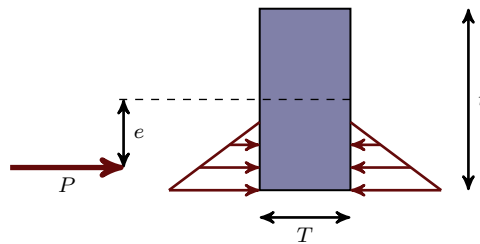


Figure 8.4: Variables on which the maximum principal tensile stress is dependent;

In order to answer these questions, structural-linear finite element analysis are executed for the dimensions shown in Figure 8.5a. The axial force P , is kept constant at $100kN$ per meter width. Due to structural linearity, the maximum principal tensile stress varies linearly with P . For all brick dimensions the eccentricity is varied from $e = t/6$ to $e/t = 11t/24$ as shown in Figure 8.5b.

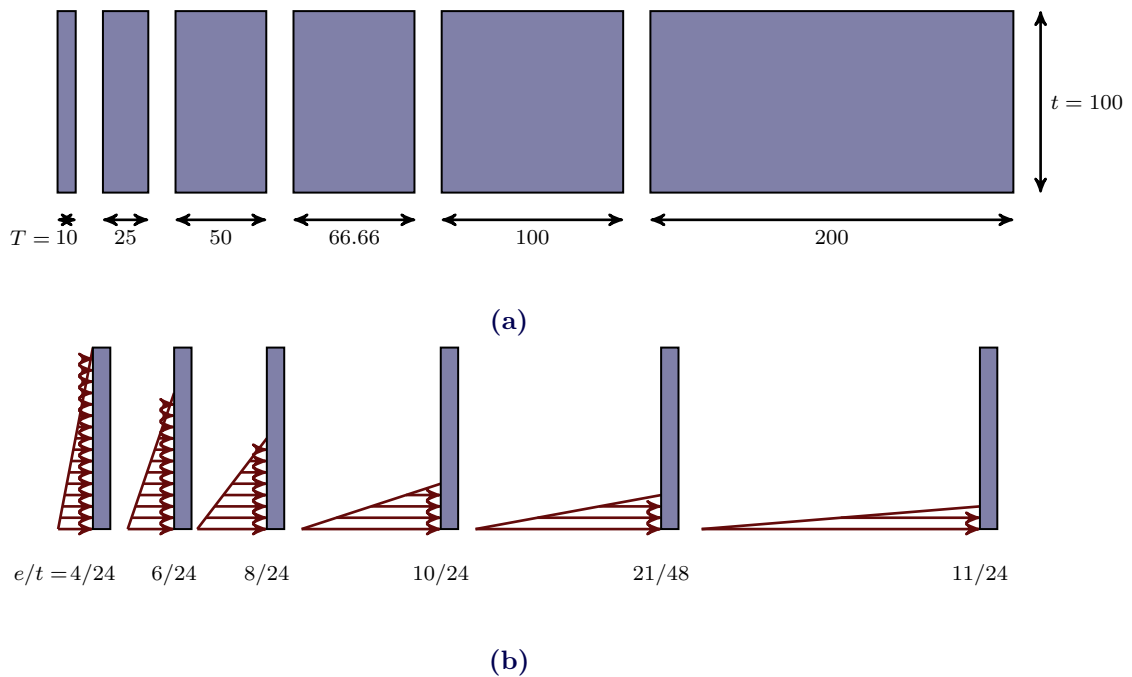


Figure 8.5: (a) Investigated dimensions in mm ; (b) Applied triangular stress distributions and corresponding eccentricities;

The glass is modeled by plain strain elements, similar to the models in Chapter 7. A mesh-size of $0.5 \times 0.5\text{mm}$ was used. Since the model is symmetrical, only half of the bricks were modeled and horizontally constraint at one side. For the brick with an T/t ratio of 0.5 the principal stress contour plots are shown in Figure 8.6. For $e/t = 4/24$ the applied triangular stress distribution starts at the top. No tensile stresses are present in this case. When the eccentricity increases, a part of the side of the brick is not loaded, whereas the load on the remaining part increases. The bottom part of the brick wants to deform, but the top does not. This introduces vertical tensile stresses, which are maximum at the location where the applied triangular stress distribution starts/ends. For all investigated brick-dimensions, the principal tensile stress as a function of the eccentricity is provided by Figure 8.7. For $e \leq 4t/24$ no tensile stresses will occur. As the eccentricity approaches the outer boundary ($0.5t$) the tensile stress rapidly increases.

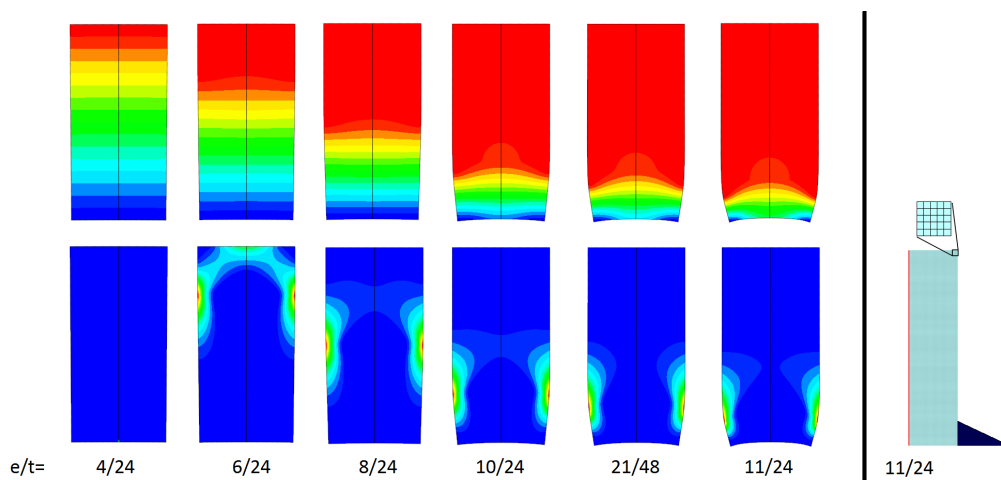


Figure 8.6: Contour plots principal stresses for several eccentricities; (top) compression (bottom) tension; Deformations $\times 1000$; $T/t = 0.5$; Mesh and applied stress distribution for $e/t = 11/24$ shown at the right, left side is axis of symmetry (constraint horizontally);

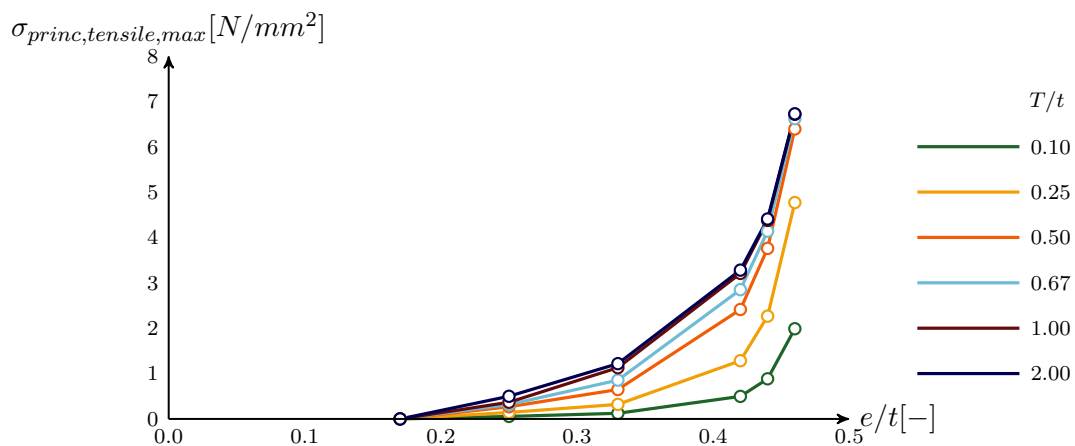


Figure 8.7: Principal tensile stress as a function of the eccentricity, for several aspect ratios of the brick; [Based on $P = 100\text{kN}$ and $t = 100\text{mm}$];

From Figure 8.8 it follows that the tensile stress reduces as the aspect ratio of the brick is reduced. This can be explained by considering that the difference in deformation between the loaded and unloaded part of the brick becomes bigger as T increases.

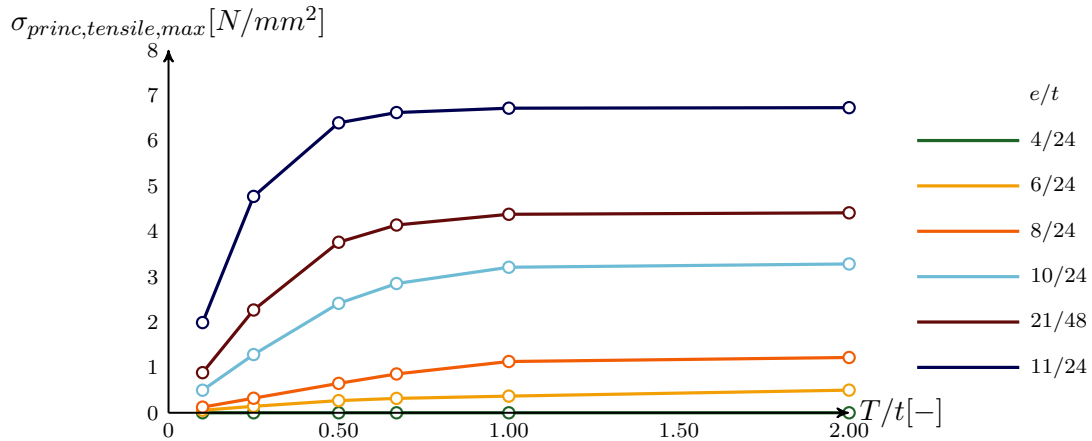


Figure 8.8: Principal tensile stress as a function of the brick's aspect ratio, for several eccentricities; [Based on $P = 100kN$ and $t = 100mm$];

If the eccentricity of the line of thrust becomes too big, the tensile strength of the glass will be exceeded. One way to limit the eccentricity of the line of thrust is by application of a resilient interlayer. To demonstrate how Figure 8.7 can be used to formulate a stiffness for this interlayer, the case study is regarded.

Case study: Maximum interlayer stiffness

The maximum tensile stress that occurs, results from the axial force, the dimensions of the brick and the eccentricity. The eccentricity that occurs is depended on the stiffness of the interlayer that is applied. To limit the eccentricity a maximum interlayer stiffness is formulated. This is done by executing the following steps:

- Compute the expected axial force P (per meter width):

$$P = \sqrt{\left(\frac{1}{8} \frac{ql^2}{f}\right)^2 + \left(\frac{ql}{2}\right)^2} = \sqrt{\left(\frac{1}{8} \frac{19 \cdot 14^2}{0.7}\right)^2 + \left(\frac{19 \cdot 14}{2}\right)^2} = 678kN$$

- Choose brick dimensions T and t and compute T/t :

$$\begin{aligned} T &= 100mm \\ t &= 400mm \\ T/t &= 0.25 \end{aligned}$$

- Compute the maximum allowable tensile stress in the glass (e.g. by using the NEN 2608:2014):

$$f_{mt;u;d} = \frac{1 \cdot 1 \cdot 0.29 \cdot 0.8 \cdot 45}{1.8} = 5.8MPa \quad (\text{See Appendix A})$$

- *Compute correction for size and load:*

The design graph is based on $P = 100kN$ and $t = 100mm$. In order to use it, a correction is made for the values on the y-axis (the tensile stress):

$$1N/mm^2 \equiv 1 \cdot \frac{P}{100} \cdot \frac{100}{t} = 1 \cdot \frac{678}{100} \cdot \frac{100}{400} = 1.7N/mm^2$$

- *Determine the corresponding maximum eccentricity:*

From Figure 8.9 it follows that e/t should be lower than or equal to 0.449.

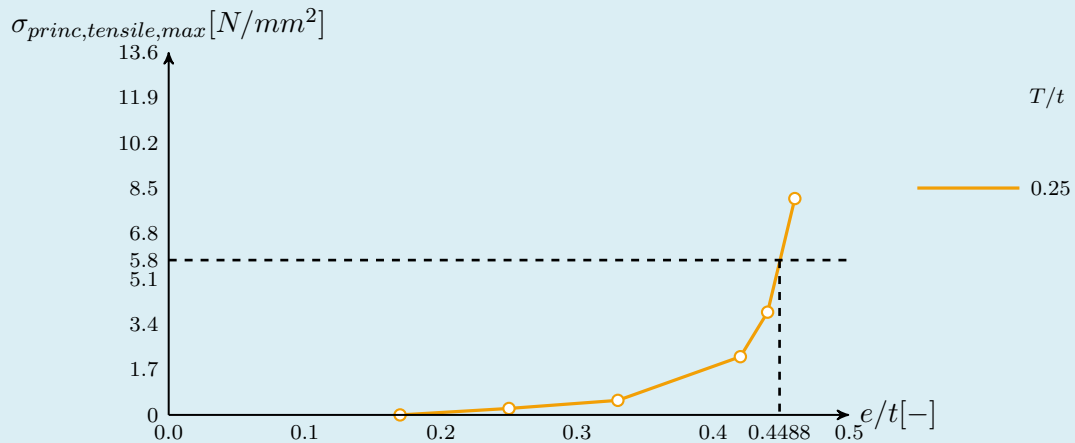


Figure 8.9: Principal tensile stress as a function of the eccentricity;

- *Determine the maximum allowable interlayer-stiffness that corresponds to the maximum allowable eccentricity:*

The relation between the interlayer-stiffness and the eccentricity follows from Table 7.2 in Chapter 7 and is presented in Figure 8.10.

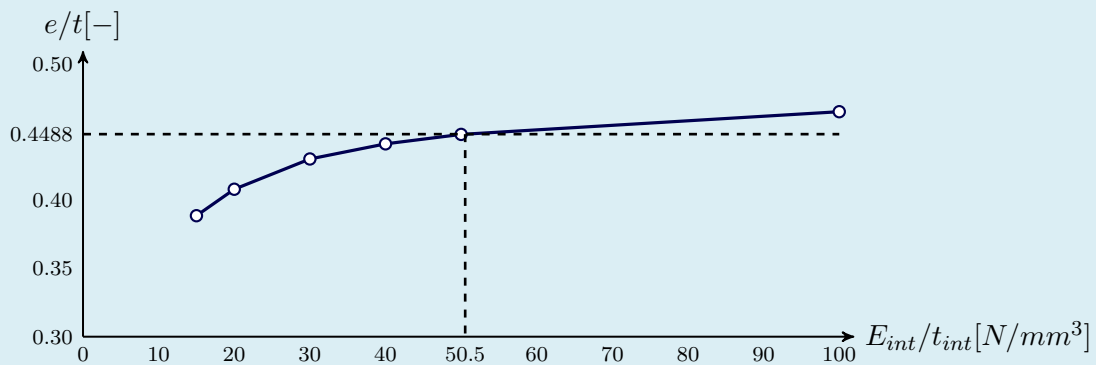


Figure 8.10: Relation interlayer stiffness and eccentricity of the line of thrust;

It follows that the maximum allowable stiffness of the interlayer is $50.5N/mm^3$.

8.3 Tensile stress due to local effect

8.3.1 Introduction

The surface of glass is not perfectly flat and glass is very stiff. Therefore if a dry stack of glass bricks is loaded in compression, stress concentrations will occur at the points of contact. Due to these stress concentrations, tensile stresses will occur as shown in Figure 8.11a, which may lead to failure. By application of a resilient interlayer this problem can be overcome. Since the interlayer is resilient it can accommodate for flatness imperfections and thereby reducing the stresses as shown in Figure 8.11b. The imperfect surface flatness results from the production method that is used, of which some background is provided in Appendix E.1.

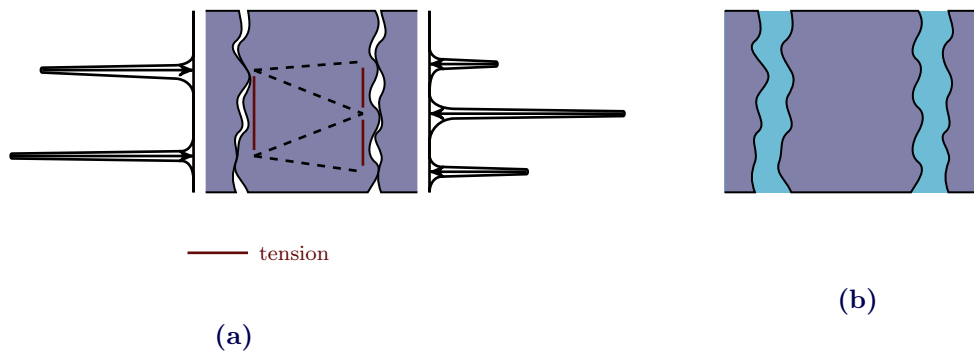


Figure 8.11: (a) Tensile stresses due to stress concentrations; (b) Redistribution by resilient interlayer;

But how can one establish if an interlayer will function properly? If the interlayer is too stiff or thin, the imperfections cannot be accommodated. In this section a method is proposed to ‘design’ the stiffness/thickness-ratio of such an interlayer. It is based on an elastic interlayer-behavior and lateral deformations are not taken into account. However it may serve as a starting point, to select certain materials. Experimental validation of the proper functioning is required.

8.3.2 Interlayer-stiffness design

The resilient interlayer that is applied between two glass surfaces, should accommodate for the imperfect surface flatness. The surfaces should be in contact before too high tensile stresses can develop. The average compressive stress that corresponds to this moment, is taken from the experimental research conducted by Oikonomopoulou et al. (2014). Glass bricks ($210 \times 210 \times 65 \text{ mm}$) would fail at an average compressive stress of $20 - 30 \text{ MPa}$ when *not* applying an interlayer. For interlayer-design it is taken as a starting point that the surfaces should be in full contact before reaching an average compressive stress of 20 MPa . After that, additional loads will be distributed over the full surface and not introduce additional tensile stresses. Thus:

$$\sigma_{\text{contact}} \leq 20 \text{ MPa} \quad (8.1)$$

To determine the maximum stress that can develop before there is full contact, only one variable is required as input: the maximum deviation Δ . Since both surfaces have this

deviation, there will be full contact between all surfaces after a displacement of 2Δ . Imagine that a displacement of 2Δ is now applied, as shown in Figure 8.12. Using Hook's law, it follows that the highest stress that can develop during this displacement can be obtained using the following formula:

$$\sigma_{contact} = E_{int} \cdot \frac{2\Delta}{t_{int}} \quad (8.2)$$

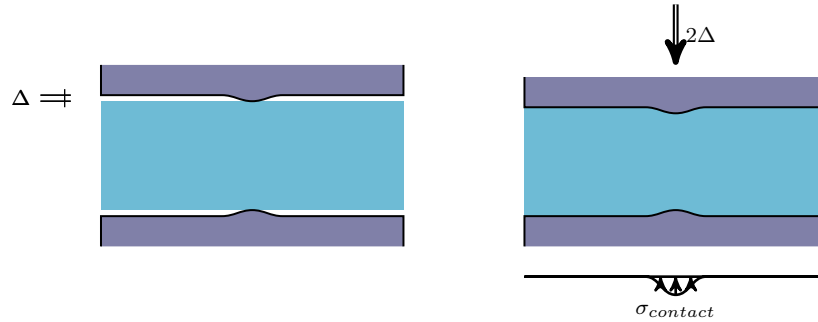


Figure 8.12: Stress when the surfaces are just in contact;

For this equation, it is assumed that the glass is significantly stiffer than the interlayer and all deformations will be in the interlayer. From (8.1) and (8.2) the maximum interlayer stiffness now follows:

$$\frac{E_{int}}{t_{int}} \leq \frac{20}{2\Delta} \quad (8.3)$$

Using equation (8.3) the maximum stiffness/thickness ratio for an elastic interlayer can be formulated. This maximum will assure full surface contact before too high tensile stresses can develop. Note that this equation is only valid if the thickness is sufficient to absorb the expected deformations:

$$t_{int} \geq u_{exp} = \frac{\sigma_{avg}}{E_{int}} \cdot t_{int} + 2\Delta \quad \rightarrow \quad t_{int} \geq \frac{2\Delta}{1 - \frac{\sigma_{avg}}{E_{int}}}$$

8.4 Interlayer-material selection

Case study: Interlayer specification

The analysis from both this chapter and Chapter 7, enables the formulation of a stiffness-interval in which a suitable interlayer should lie within. From Figure 7.15 it followed that, to assure *stability*, the minimal interlayer stiffness should be:

$$\frac{E_{int}}{t_{int}} \geq 26N/mm^3$$

In Section 8.2 a limit for the eccentricity of the line of thrust was formulated, to *not* exceed the maximum allowable tensile strength. The maximum interlayer stiffness for

which this can be achieved is:

$$\frac{E_{int}}{t_{int}} \leq 50.5N/mm^3$$

In Section 8.3 the local effect was addressed. From (8.3) and a maximum surface deviation of $\Delta = 0.25mm$, it follows that the local effect will not be problematic if the following requirement is met:

$$\frac{E_{int}}{t_{int}} \leq 40N/mm^3$$

This provides the stiffness-interval $26 \leq E_{int}/t_{int} \leq 40N/mm^3$.

Limiting the interlayer thickness from 1 to 8mm, results in an interval for the modulus of elasticity: $0.03GPa \leq E_{int} \leq 0.3GPa$. The interlayer-material should have a stiffness within this interval and satisfy additional requirements:

- Mechanical: $0.03GPa \leq E_{int} \leq 0.3GPa$
- Transparency: Optical quality/transparent/translucent
- Durability UV-light: Fair/good/excellent
- Compressive strength $\geq 25MPa$
- Maximum service temperature: $\geq 50^\circ C$

These requirements served as input for the material database *CES2016*, which resulted in the materials provided by Table 8.1.

Table 8.1: Suitable materials that fulfill the requirements for the interlayer, selected using material database CES2016;

Material	$\sigma_{c;u;d}$ [MPa]	Transparency	UV resistance
PEBA	41	Transparent	Fair
PU	48	Transparent	Fair
PVC	25	Transparent	Fair
PVDC	39	Transparent	Good
SEBS	37	Transparent	Fair
TPU	61	Optical quality	Fair

8.5 Conclusions

Even when a brick is loaded in compression only, tensile stresses will always be introduced due to (slight) imperfect conditions. For a glass brick located within an arched masonry bridge, tensile stresses will mainly result from two effects:

Global effect: Discontinuous stress-distribution due to eccentricity of the line of thrust.

Local effect: Peak stresses due to imperfect flatness glass.

The global effect refers to the typical triangular stress distribution that results from the eccentricity of the line of thrust. The brick dimensions are denoted as T and t , in which the latter one is the length of the side that is in contact. It can be concluded that the lower

the ratio T/t , the lower the maximum tensile stress that occurs. This can be explained by considering that the tensile stress is a result of a restrained difference in deformation between the loaded and unloaded part. As the thickness reduces, this difference becomes less.

The local effect refers to an imperfect surface-flatness, which introduces tensile stresses. This can be resolved by application of a resilient interlayer. The surfaces should be in contact before too high tensile stresses can develop. As a starting point, a maximum interlayer-stiffness is formulated that assures full contact at an applied average stress of $\sigma_{contact} = 20MPa$. The formula is based on an elastic interlayer-behavior and disregards lateral deformations. It depends on the maximum deviation Δ of the glass-surface. To assure full contact of all surfaces, before a too high tensile stress can develop the following requirement should be met:

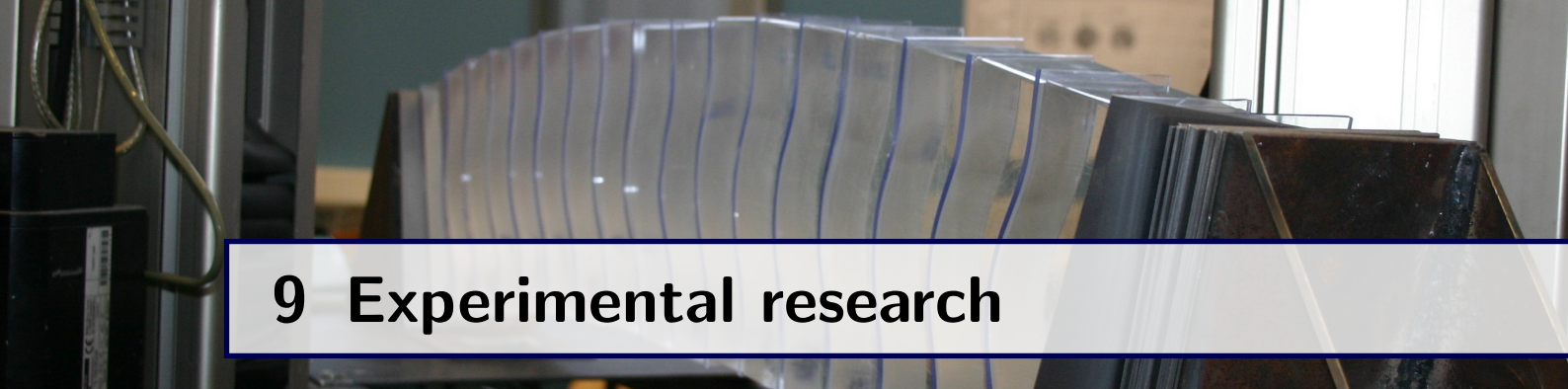
$$\frac{E_{int}}{t_{int}} \leq \frac{\sigma_{contact}}{2\Delta}$$

This equation is only valid if the thickness is sufficient to absorb the expected deformations:

$$t_{int} \geq \frac{2\Delta}{1 - \frac{\sigma_{avg}}{E_{int}}}$$

Case study: Interlayer

In order to limit the eccentricity of the line of thrust such that the the maximum allowable tensile strength is not exceeded (global effect), it must hold that: $E_{int}/t_{int} \leq 50.5N/mm^3$. In order to assure full contact of all surfaces, before a too high tensile stress can develop (local effect), it must hold that: $E_{int}/t_{int} \leq 40N/mm^3$. For sufficient stability it followed from Chapter 7 that: $E_{int}/t_{int} \geq 26N/mm^3$. Limiting the interlayer thickness from 1 to 8mm, results in an interval for the modulus of elasticity: $0.03GPa \leq E_{int} \leq 0.3GPa$. By formulating additional requirements on transparency, durability, strength and service temperature, the following possibly suitable materials were selected: PEBA, PU, PVC, PVDC, SEBS and TPU. PVC and PU can be supplied in sheet form and will be further investigated in Chapter 9.



9 Experimental research

9.1 Introduction

In this chapter two experiments will be discussed. In the first experiment a stacked glass-interlayer system is investigated, to establish the behavior of the interlayer-materials that were selected in Chapter 8, i.e. PVC, PU70, and PU90. In the second experiment, a 1m-span glass arch was tested, to investigate the deflections, stress distribution and failure behavior.

9.2 Stacked glass-interlayer system

9.2.1 Introduction

In order to assure a distributed stress-transfer between bricks, several suitable interlayer-materials have been selected. The stiffness of the brick-interlayer system mainly results from the deformation of the interlayer. This deformation relates to the elasticity of the interlayer, which is time and temperature dependent. However, the deformation is partly opposed by the friction between the surface of the glass and the interlayer. In order to establish the behavior of certain interlayer materials within the glass-interlayer system, experiments are conducted in which this behavior is investigated. Due to friction, the results may depend on the ratio between the contact area and volume of the interlayer. Therefore the elasticity of the interlayer is expected to be dependent on the thickness.

The following objectives are formulated:

- Determine the modulus of elasticity for the interlayer-materials within the glass-interlayer configuration
- Determine the significance of time-dependent behavior (creep)
- Investigate the relation between the modulus of elasticity and the sheet thickness

In this experiment, the materials PVC, PU70 and PU90 are investigated as interlayer, for thicknesses of 1, 2, 3 and 4mm. To limit the scope, the temperature dependency is not investigated.

9.2.2 Description of the experimental setup

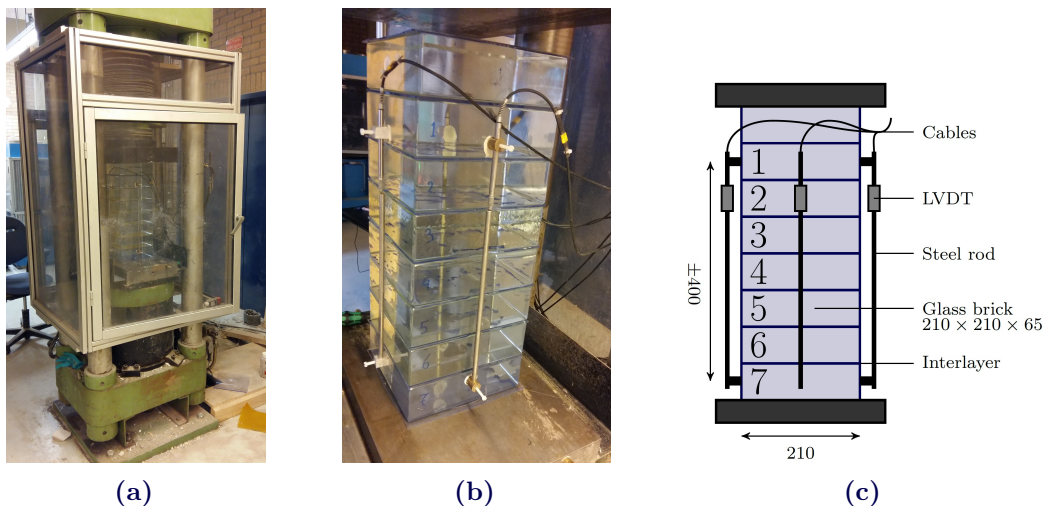


Figure 9.1: Experimental setup; (a)Hydraulic press; (b)Glass-interlayer specimen with LVDTs; (c)Schematic illustration, dimensions in *mm*;

The setup that is used for this experiment is shown in Figure 9.1. In 48 seconds each specimen is loaded up to 480kN, after which the load is maintained for about half an

hour (force control). During the test the displacements are measured. A high accuracy is required since the expected deformations are low. Therefore it is chosen to apply Linear Variable Differential Transformers (i.e. LVDTs), with an accuracy of $\pm 0.001\text{mm}$. At each side of the specimen such an LVDT is applied, to avoid measurement errors due to rotations.

As can be observed in Figure 9.1c, the LVDTs are situated such that the deformation of the six interlayers between brick 1 and 7 is measured. The deformation of the glass bricks themselves is only a fraction of the expected interlayer deformation (i.e. about 3%) and is neglected. An additional numberless brick is applied on top of the stack to make room for the wires connected to the LVDTs. Figure 9.2 shows the measurement system in which the LVDTs are situated. Pleximon is used to glue the connection elements onto the bricks, resulting in a rigid connection within minutes. Steel rods are situated in the connection elements at the bottom and can be adjusted in height. The LVDTs are situated in those at the top.

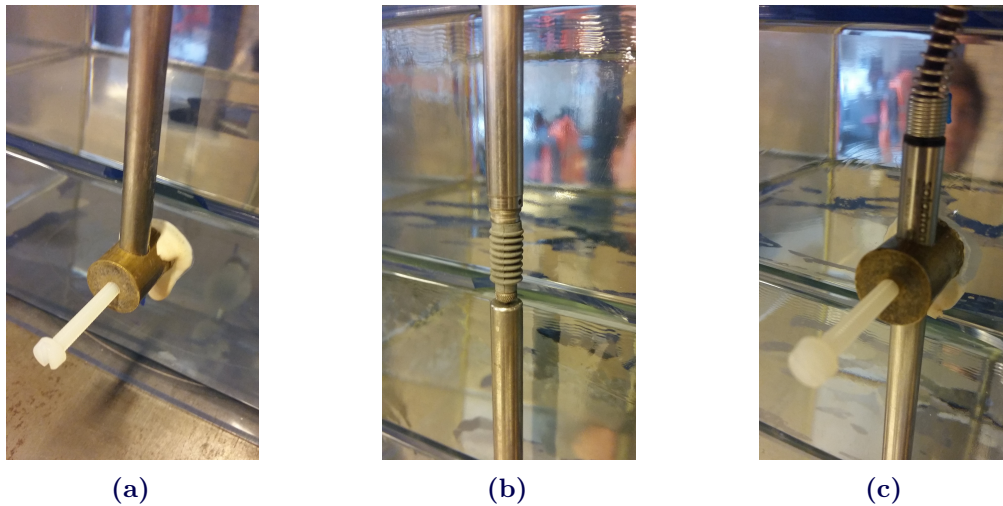


Figure 9.2: LVDT measurement system; (a)Adjustable steel rod to glass connection at the bottom; (b)The deformable part of the LVDT that touches the steel rod and measures the displacement; (c)The adjustable LVDT to glass connection at the top;

9.2.3 Results

Visual observations

Typically it can be observed that for all interlayers the contact pattern is random when no load is applied. This results from an imperfect flatness with random locations at which it is thicker. When a load is applied, the observed contact area will typically develop from the center as the load increases, as shown in Figure 9.3. For PVC this contact area develops more or less consistent: A circle-like pattern, that is bigger as the interlayer-thickness increases. This pattern can be explained considering the lateral deformation of the interlayer and the friction between the glass and interlayer. This will enclose the material in the middle, which is why the stresses will be higher there. For PU70 this behavior is somewhat less consistent, since it is stiffer the imperfect surface flatness still has an impact. For PU90, which is the stiffest material, no thickness-consistency is observed at all.

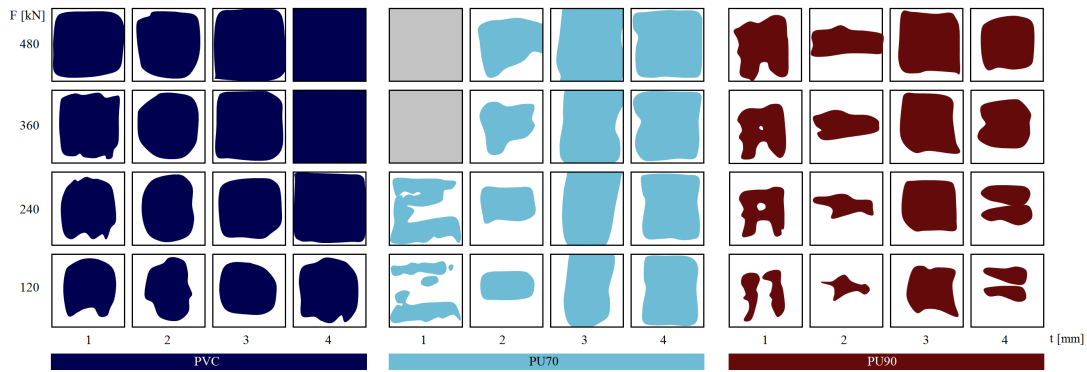
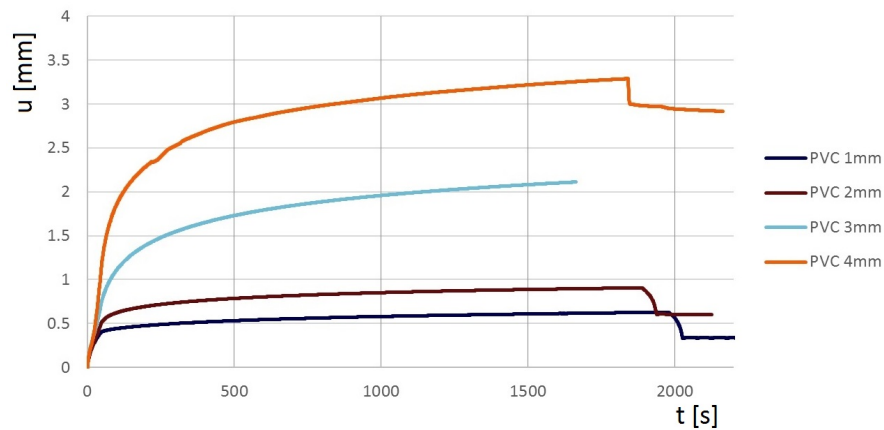
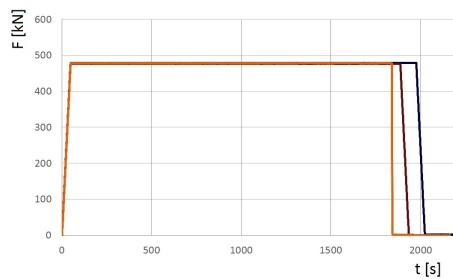


Figure 9.3: Approximate contact areas between brick 4 and 5, for an increasing load and an increasing interlayer thickness; (left)PVC; (middle)PU70; (right)PU90;

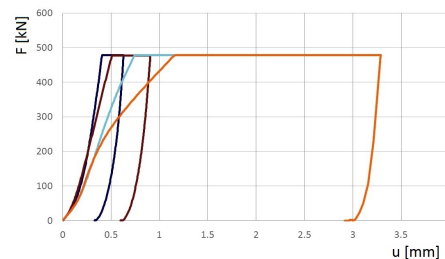
Discussion raw test-results



(a)



(b)



(c)

Figure 9.4: Test results for PVC interlayer (a) Displacement in time [u, t -diagram]; (b) Applied load program [F, t -diagram]; (c) [F, u -diagram];

Figure 9.4 shows the raw test-results for the PVC-inlayer. These results are in line with the expectations: For thicker interlayers the deformation is bigger; There is a substantial time-dependent deformation. Figure 9.4a shows that after load-removal a significant portion of the deformation remains. The negative slope after load-removal suggest that this deformation is non-permanent and that the system will approach its original configuration after sufficient time. Due to time-limitations this has not been verified. The measurement

during the 3mm-PVC-test was accidentally aborted just before unloading, which is why the post-load trajectory is not present. During application of the load the F, u -diagram in Figure 9.4c initially shows strengthening of the system, followed by softening. The strengthening can be explained by an increased contact area during loading. Apparently at this load-speed the creep of the PVC is so large that during load application the strengthening changes into a softening trend.

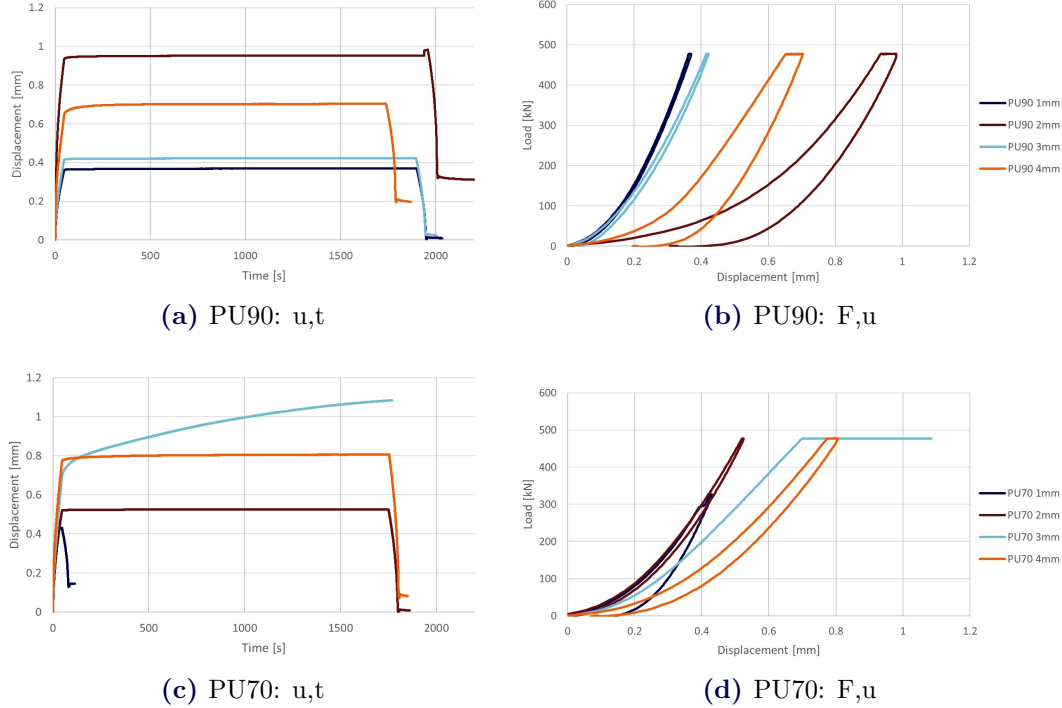


Figure 9.5: Test results for the PU interlayers;

For PU70 and PU90 the results are presented in Figure 9.5. In general the time-dependent behavior of the PU is minimal. The 3mm thick PU70 deviates from this typical behavior, since a significant time-dependent deformation is observed. The test for the 1mm thick PU70 interlayer was aborted due to the fracture of a glass brick. In contrast to the PVC there seems to be no logical trend between the displacement and the interlayer thickness. A possible explanation is the less predictable contact-pattern. Another possibility is an inconsistent composition of the supplied material. This explanation seems likely when considering that a (semi-)permanent deformation remains for 2mm and 4mm PU90, but not for 1mm and 3mm. Additionally there is the inconsistent time-dependent behavior of the 3mm PU70 layer, which was mentioned earlier.

Table 9.1: Measured sheet thicknesses: Mean and standard deviation;

PVC		PU90		PU70	
$t_{int,avg}[mm]$	$\sigma_{\bar{t}}[mm]$	$t_{int,avg}[mm]$	$\sigma_{\bar{t}}[mm]$	$t_{int,avg}[mm]$	$\sigma_{\bar{t}}[mm]$
1.06	0.05	1.10	0.00	0.88	0.09
1.89	0.03	2.33	0.21	2.02	0.08
2.97	0.11	3.28	0.08	3.37	0.12
3.85	0.14	4.27	0.17	4.00	0.10

The thicknesses of all sheets were measured at two opposite corners. Table 9.1 shows the averages and the standard deviation of the measured thicknesses. These are used for post-processing.

Elasticity and time-dependency

In order to compare the time-dependent elasticities of the different interlayer-materials, the E_{int}, t -diagrams are derived by the following procedure:

- The relation between the *displacement* and the *time* is approximated by a natural logarithm, as shown in Appendix C.3.
- To obtain the time-dependent *strain*, the result is divided by the total thickness of the 6 interlayers: $\epsilon(t) = u(t)/(6t_{int,avg})$
- The time-dependent effective *young's modulus* of the applied interlayer, then follows when the result is divided by the average stress: $E_{int,eff}(t) = \epsilon(t)/\sigma_{avg}$, where $\sigma_{avg} = F/A = 480 \cdot 10^3/210^2 = 10.9N/mm^2$

The E_{int}, t -diagrams resulting from this procedure are presented in Figure 9.6. The trends resulting from the 30-minute tests have been extrapolated to obtain these diagrams. They estimate how the effective modulus of elasticity will decrease over a period of 50 years. For estimations this extrapolation is sufficiently accurate, since the natural logarithm regression line highly correlates to the measured data. The high correlation can be concluded from the coefficients of determination, which are at least 0.98 for each individual test (1 means perfect correlation). Before practical application of the diagrams it should be verified whether the extrapolation is indeed accurate (e.g. by performing tests for longer durations).

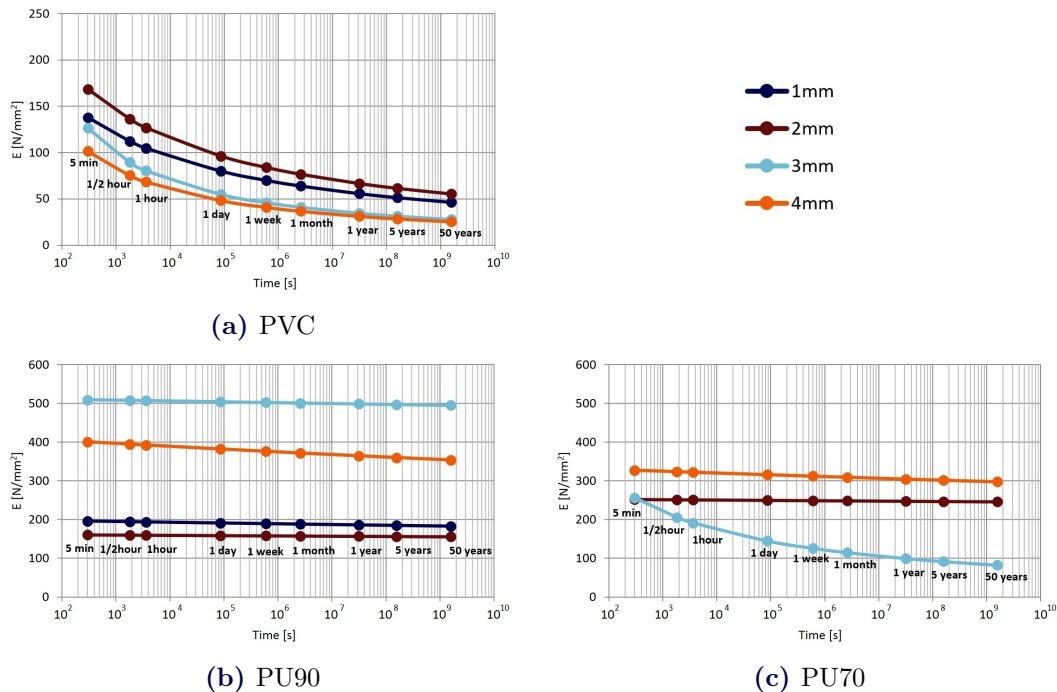


Figure 9.6: Time-depended modulus of elasticity of an interlayer, under an average stress of $\sigma_{avg} = 10.9N/mm^2$;

The modulus of elasticity of PVC shows a significant decrease over time. It is estimated that the effective modulus of elasticity found after 5 minutes could reduce by 80% in 50 years. This is based on an average load of $\sigma = 10.9N/mm^2$. The time dependent behavior for both PU70 and PU90 is minimal. The reduction is no more than 15% when comparing the effective moduli of elasticity after 5 minutes and after 50 years. The 3mm PU70 interlayer seems to be an exception to this rule. This can most likely be attributed to a material-inconsistency in the supplied sheets. It must be noted that the brick dimensions may influence the modulus of elasticity. This influence however, is not expected to be significant: As the brick surface increases, so does the length over which friction stresses can develop, therefore the contact area increases as well. This will presumably result in approximately the same modulus of elasticity.

Elasticity-thickness relation

For the PU70 interlayer, Figure 9.7 shows a clear relation between the thickness and the modulus of elasticity: A bigger thickness corresponds to a bigger modulus of elasticity. As the thickness increases, the slope reduces. This can be explained by regarding the contact patterns. As the thickness increases, the contact area increases (at the same load) and thereby it behaves stiffer. As full contact is approached, the rate at which the modulus of elasticity increases will reduce. The PVC interlayers show a similar behavior, except that they show a reduction at the end. This can be attributed to the creep that occurred during load-application, as was established from Figure 9.4c. The PU90-results are inconsistent.

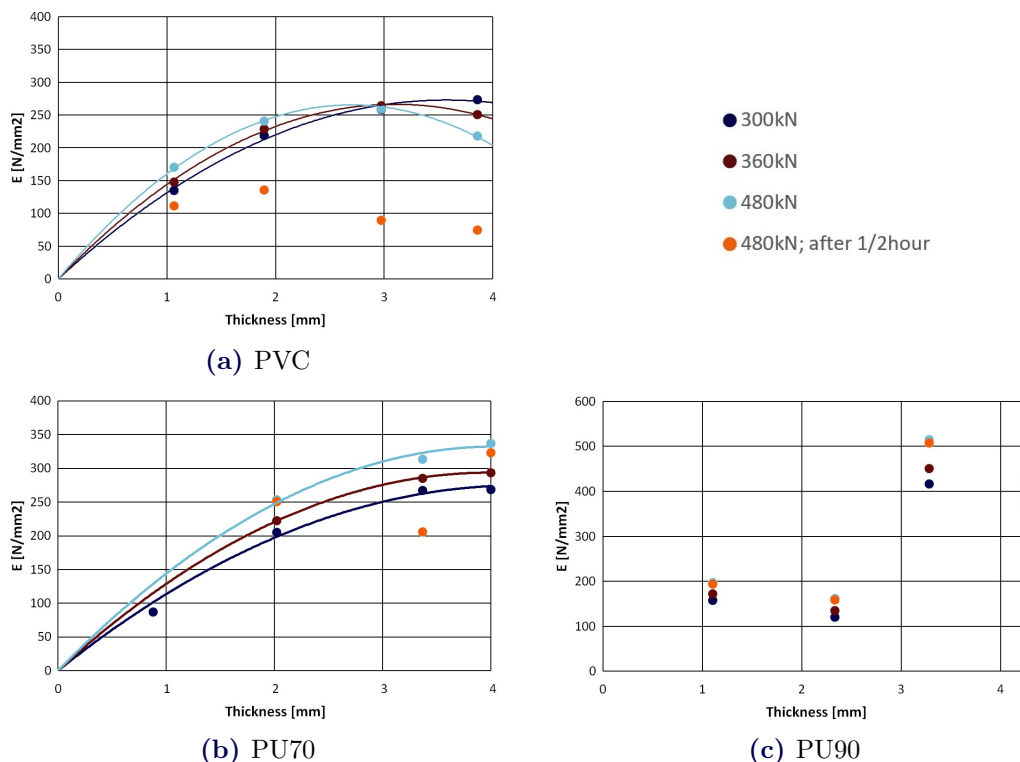


Figure 9.7: Thickness-depended effective modulus of elasticity of the interlayers;

Fractured bricks

Considering the *average* compressive stress of $11N/mm^2$ which was applied during this experiment, breakage was not expected. Oikonomopoulou et al. (2014) has previously conducted experiments on these bricks, in which failure would occur between 20 and 30MPa, when compressed without resilient interlayers (5 tests compressed between thick steel plates).

The first brick broke during the experiment in which the 2mm-PU90 interlayer was applied. Contrary as to what one might expect, this breakage occurred not during application of the load, but after the full $480kN$ had been present for approximately half an hour. The fractured brick is shown in Figure 9.8. In the 1mm-PU70 experiment a second brick fractured, but this time during load application at $326kN$.

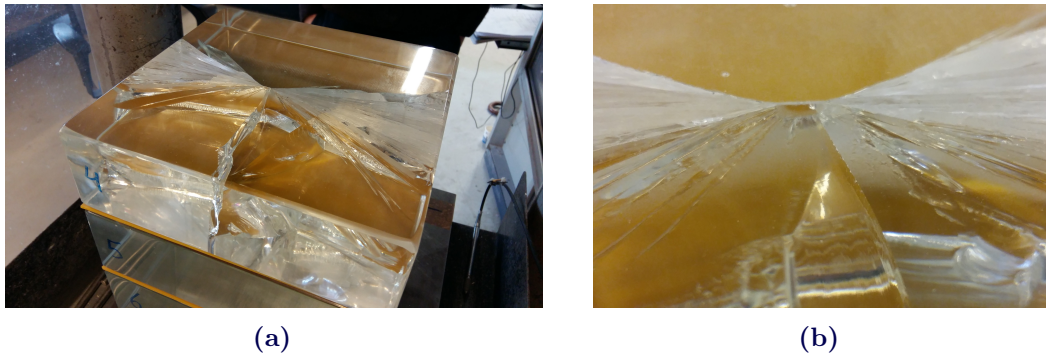


Figure 9.8: (a)Fractured brick during the experiment with the 2mm-PU90 interlayer; (b)Close up origin of fracture;

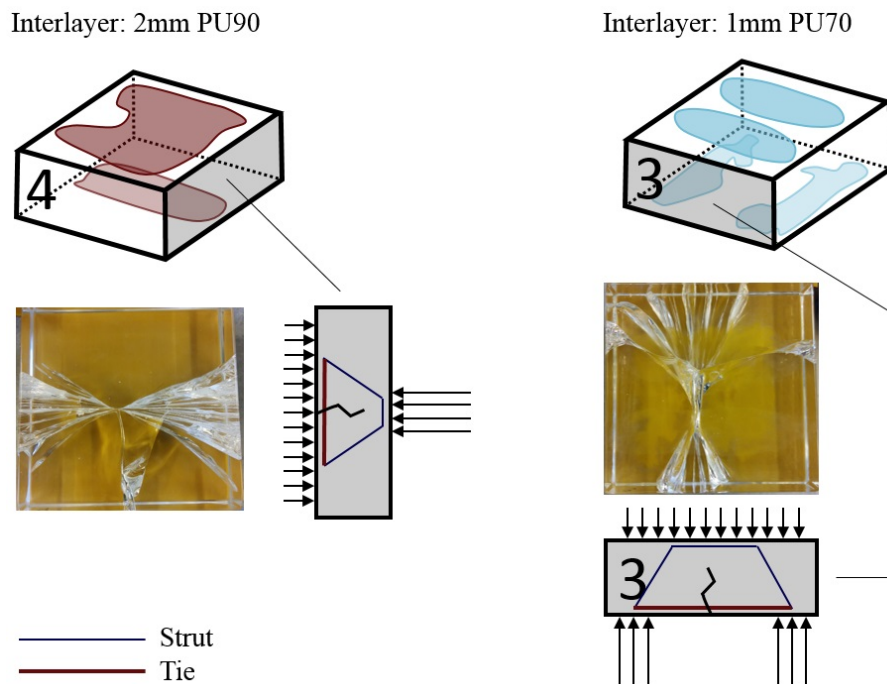


Figure 9.9: Strut and tie diagrams resulting from the contact-areas, explaining the observed fracture;

When comparing the contact areas at the top and bottom of the bricks, it seems that they are unfavorably located with respect to one another. As indicated by the strut- and tie diagrams in Figure 9.9, this has most likely introduced tensile stresses. These diagrams are in line with the observed origin- and direction of the fractures. Based on the strut and tie models, using an effective width of 20mm , the tensile stresses at failure are estimated to be about 82N/mm^2 and 70N/mm^2 respectively. Even though these bricks were post processed by CNC-milling, and thus no overall imperfection was expected, unlucky areas of contact still resulted in a failure comparable to what one might expect from an overall brick imperfection, such as shown in Figure 8.3b in Chapter 9.

In the first fractured brick (number 4) there was contact between the interlayer and the glass at the origin of fracture. This suggest that additionally to the tensile stresses introduced by unfortunate locations of contact, there may have been tensile stresses resulting from the friction between the interlayer and the glass. The friction is caused by lateral expansion of the interlayer, which may have (slightly) increased over time. This would explain why the glass broke after the load had been present for half an hour already.

Case study: Applicability interlayers

An interlayer is suitable to be applied in the case study if it is sufficiently stiff (in time) to assure stability, and adequately distributes the stresses. Therefore if all criteria in Table 9.2 are satisfied, the interlayer can be applied. It shows that 1- and 2mm-PVC can be applied, but thicker sheets are insufficiently stiff over time. The 3- and 4mm-PU70 sheets can be applied as well but thinner sheets may cause fracture. For PU90 the modulus of elasticity is probably sufficient, but due to the large scatter it can not be relied upon.

The 1mm-PVC interlayer is preferred when considering that it is desired to keep the thickness as small as possible. However, a high modulus of elasticity is also desired too increase the stability. Either 1mm-PVC or 4mm-PU70 can be applied. For 1mm-PVC, the time depended behavior should be verified.

Table 9.2: Interlayer applicability;

Material	t_{int} [mm]	Stability $E_{int}/t_{int} > 26\text{N/mm}^3$	Stability after creep $E_{int}/t_{int} > 26\text{N/mm}^3$ after $t = 5\text{years}$	Stiffness reliability	Strength Stress sufficiently distributed
PVC	1	171	51	+	±
	2	121	31	+	±
	3	87	10	+	±
	4	55	7	+	+
PU70	1				–
	2	127	123	±	–
	3	105	31	±	±
	4	84	75	±	+
PU90	1	198	185	–	–
	2	81	78	–	–
	3	172	166	–	+
	4	107	90	–	±

9.2.4 Conclusions and Recommendations

Time-dependency

The modulus of elasticity of PVC shows a significant decrease over time. It is estimated that the effective modulus of elasticity found after 5 minutes could reduce by 80% in 50 years. This is based on an average load of $\sigma = 10.9N/mm^2$. The time dependent behavior for both PU70 and PU90 is minimal. The reduction is no more than 15% when comparing the effective moduli of elasticity after 5 minutes and after 50 years.

Thickness-dependency

For the PU70 interlayer it holds that a bigger thickness corresponds to a bigger modulus of elasticity. As the thickness increases, the slope reduces. This can be explained by regarding the contact patterns. As the thickness increases, the contact area increases and thereby it behaves stiffer. As full contact is approached, the rate at which the modulus of elasticity increases, will reduce. The PVC interlayers show a reduction of the modulus of elasticity between 3 and 4mm. This can be attributed to the creep that occurred during load-application. The PU90-results are inconsistent.

Case study: Advised interlayer

Both the 1mm-PVC and the 4mm-PU interlayer would be suitable. They are sufficiently stiff to assure the stability of the bridge, since they meet the requirement that followed from Figure 7.15 in Chapter 7. Therewith the stresses are adequately distributed. Before the 1mm-PVC interlayer can be applied, the time-dependent behavior should be verified (test for longer durations). For the 4mm-PU70 interlayer the transparent variant should be tested before application. Furthermore the temperature-dependency should be investigated.

9.3 Glass arch scale test

9.3.1 Introduction

Although at this point a good understanding of the structural concept of an arched glass bridge has been obtained, practical applications and experimental data is lacking. Therefore load-tests on a 1m-span mock-up of a glass arch have been carried out, in order to achieve the following objectives:

- Validation of the FEM-analysis by comparison of the displacement field
- Investigate the magnitude and distribution of stresses
- Establish the failure behavior (brittle/ductile)

Proper functioning of the arch in this experiment is highly relevant for establishing the feasibility of TU-Delft's glass masonry bridge. The shear-resisting geometry of the glass bricks that will be used there, has therefore been applied in this experiment as well. This resulted from a study towards a brick-geometry that is both shear-resisting and suitable for a cast-glass production method. The preparations for this experiment have been executed in association with Ate Snijder.

9.3.2 Description mock-up construction

The shear-resisting brick geometry has been obtained by water-jet cutting several square soda-lime silica glass bricks, such as used in the column experiment in section 9.2. This provided the result shown in Figure 9.10, in which some protruding (blue-marked) imperfections were still present.

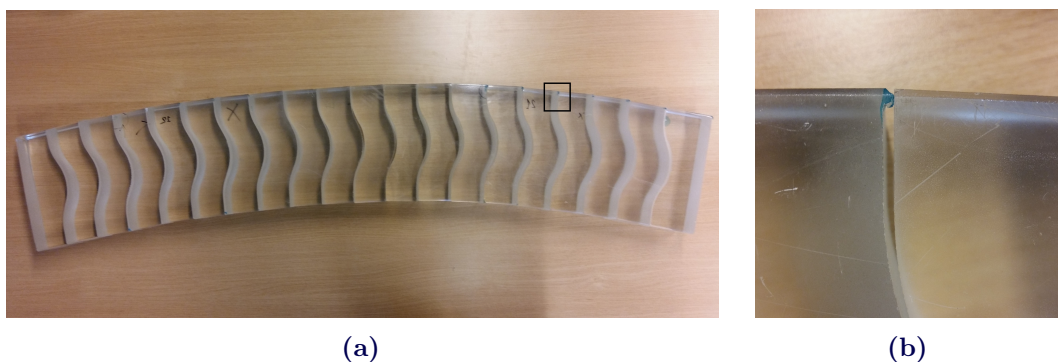


Figure 9.10: Water-jet cut soda-lime-silica glass bricks; (a) In configuration; (b) Showing problematic protruding imperfections;

Figure 9.11 shows the grinding of the glass in order to remove the protruding ‘bumps’ and to smoothen the ‘waviness’-surface that resulted from the water-jet process. The construction of the mock-up is shown in Figure 9.12.

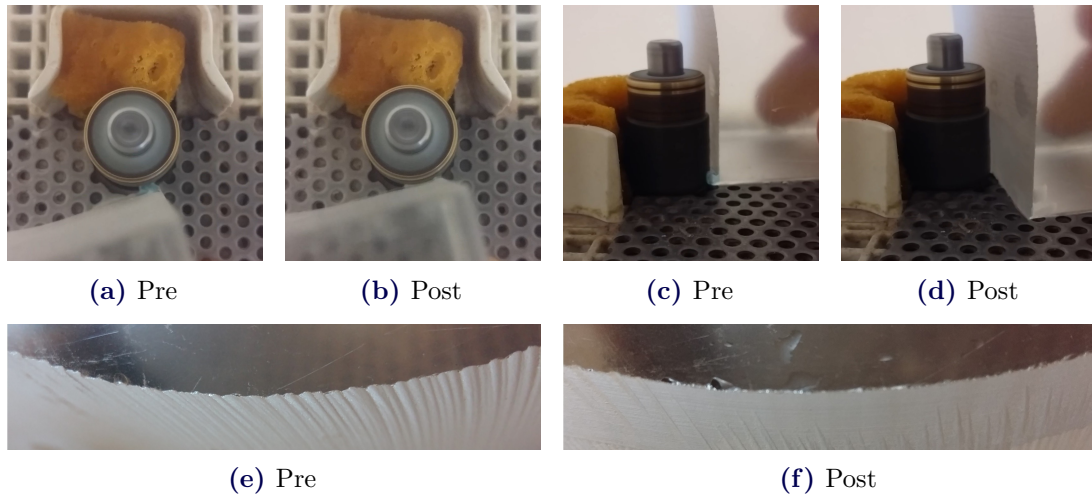


Figure 9.11: Grinding;



(a) Construct glass arch within steel frame;



(b) Remove temporary support;



(c) Apply lateral (torsional) buckling supports;



(d) Remove lateral positioners;

Figure 9.12: Construction mock-up;

9.3.3 Photographic displacement measurements

Experimental setup

For validation of the finite element model, the displacement field of the arch is measured. When the displacements are big, a better comparison between the experiment and the model can be made, therefore a soft interlayer is used in this experiment: 4mm-PVC. A load of 20kN is applied, for a duration of 30 minutes. The 30-minute modulus of elasticity of $75N/mm^2$ resulting from Figure 9.6 is used as input for the finite element model.

The displacement-field is obtained using a photographic measurement method, which measures the displacement of several dots. Figure 9.13a shows the dots applied onto both the glass bricks and the steel frame. The steel frame is only supported in the middle and will deflect as well. By measuring these displacements as well, the actual deflection of the glass arch can later be derived. It is chosen to surround the green dots by a pink area, which will result in a better contrast making the method more accurate.

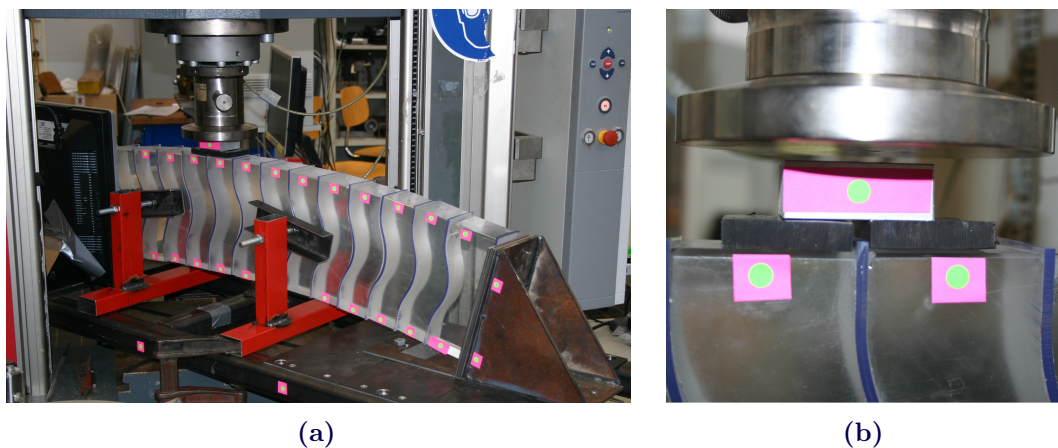


Figure 9.13: (a)Experimental setup for photographic displacement measurements; (b)Load-introduction;

Analysis of the results



Figure 9.14: Photographic displacement measurements; (a)Unloaded; (b)Loaded by 20kN for 30 minutes;

Figure 9.14 shows the arch pre-loading and after a load of 20kN has been present for half an hour. These images are edited such that only the dots are visible, as shown in Figure 9.15a. Subsequently these dots are identified by the software *Ocv3*, as shown in Figure 9.15b. The software then provides these dots' coordinates in pixels as output. The pixels are then converted to millimeters. Note that 2 different scales are used, since the dots applied on the steel frame are closer to the camera than those onto the bricks. The computed vertical deflections are presented in Figure 9.16. A correction has been made for the deflection of the steel frame.



Figure 9.15: Photographic displacement measurements;

Results

The measured displacement field correlates to the result of the finite element analysis, as shown in Figure 9.16. The finite element model of the experiment is shown in Figure 9.17. The correlation validates the finite element analysis in Chapter 7. Additional validations for larger spans are recommended. Without accurately modeling the deformations of the steel frame, this high correlation could not be achieved. Hence, establishing a reliable support stiffness is of vital importance in order to make an accurate prediction of the displacements.

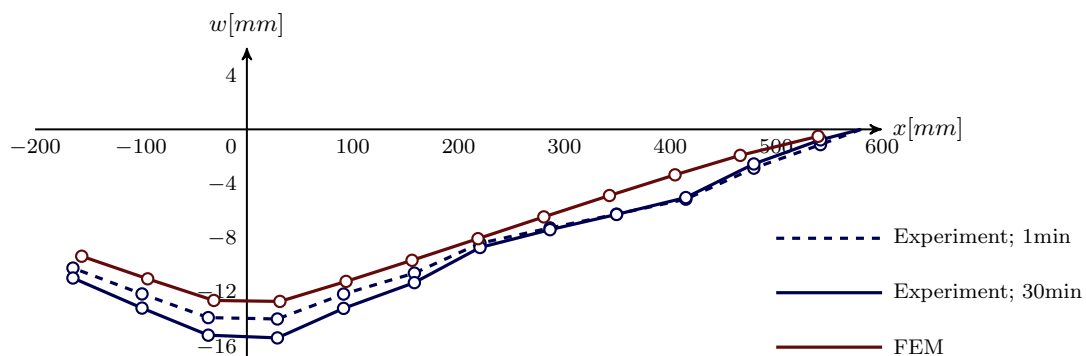


Figure 9.16: Displacement field for both the experimental- and FEM analysis;

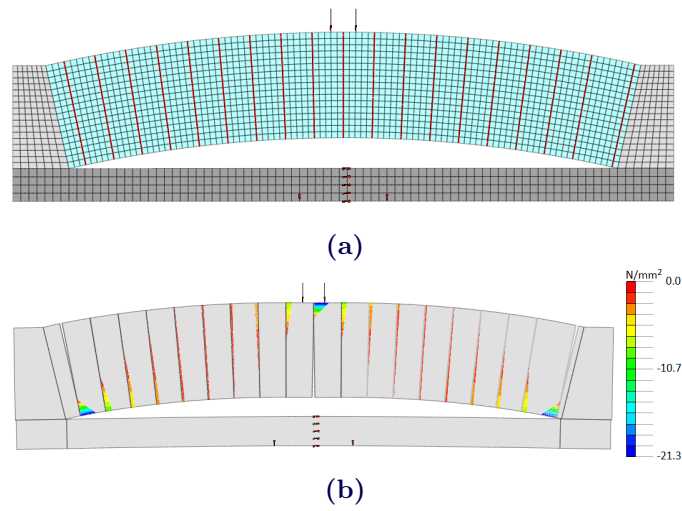


Figure 9.17: Finite element model for experiment; (a) Mesh, constraints and location of loads; (b) Deformed model for 20kN load, also showing compressive stresses in the interface;

9.3.4 Photo-elastic stress measurements

Background theory on photo-elasticity

To understand the method that is used in this experiment, a brief explanation about optical stress measurement in glass is given, based on McKenzie and Hand (1999).

Light travels in the form of a wave, with a certain wavelength and amplitude. The wavelength corresponds to a certain color. The amplitude relates to the brightness. Another property of light is the *orientation of the oscillation*. Normal white light (e.g. sunlight) consists of many waves that vary in amplitude, wavelength and in orientation.

A photo-elastic analysis requires the light to be *polarized*, which means that the geometrical orientation of the oscillation is specified. (Sun-)light can be polarized by applying a polaroid filter. The functioning of this filter is based on selective absorption and absorbs the light that oscillates in all orientations except for one. LCD-screens already emit polarized light by it self (without using an additional filter).

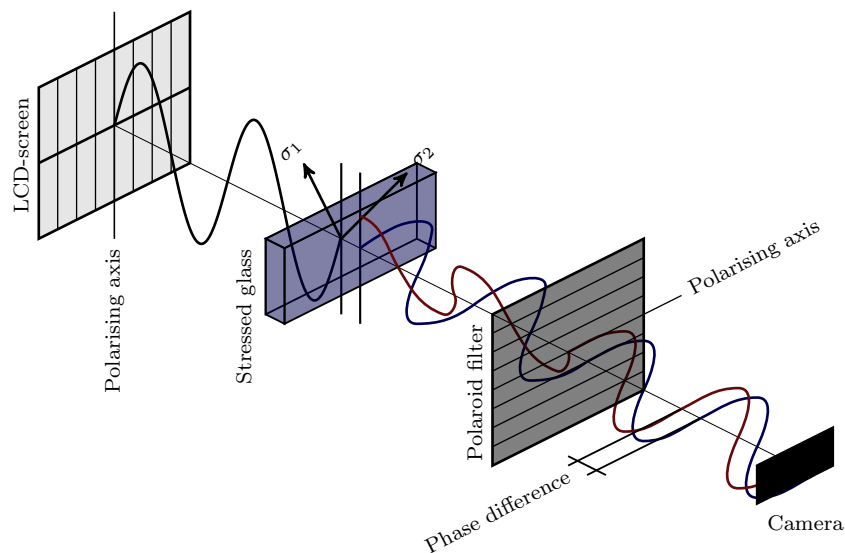


Figure 9.18: A plane polariscope arrangement, consisting of a polarized light source, a (glass) specimen, an analyzer (polaroid filter) and a view screen (camera); Based on McKenzie and Hand (1999);

Birefringe materials have a refractive index that depends on the polarization of the light. Isotropic materials (such as glass) do not show birefringe. However, when the glass is stressed, birefringe is developed. In a photo-elastic analysis the effects of (stress-)birefringe are interpreted and measured. To do so a plane polariscope arrangement may be used, as shown in Figure 9.18. A polarized beam of light emitted from the screen, will split into *two* components when entering glass that is subjected to a loading. The orientation of these components corresponds to the principal stress directions. These components will then propagate through the glass at different velocities. Therefore, when emerging from the glass, a phase difference will be present.

To visualize the effects of the stress-birefringence, an analyzer (e.g. a polaroid filter) is required to recombine the components onto one plane. Due to phase difference certain wavelengths (colors) are extinguished while others are intensified, which produces an *interference pattern*. The results can be interpreted by investigating the so called fringes that can be observed. Two different type of fringes can be distinguished:

Isoclinics are observed as black fringes, and have the same principal stress direction as the direction of the polarized light entering the specimen. Note that black areas may also indicate a stress-free area.

Isochromatics are the loci of all points that have the same color, meaning that at these points the *principal stress differences* are equal. The principal stress differences can be quantified using the stress-optic law:

$$(\sigma_1 - \sigma_2) = \frac{N\lambda}{Ct} \quad (9.1)$$

In this formula N is the isochromatic fringe order, λ is the wavelength of the extinguished colors, C is the optical stress coefficient ($2.72 \cdot 10^{-6} \text{mm}/N$ for float glass) and t is the thickness of the specimen. This formula holds when the stresses do not vary over the thickness. Note that this formula does not provide absolute stresses, unless the quantity of one of the principal stresses is known or known to be zero.

Experimental setup

The plane polariscope arrangement that is used, is shown in Figure 9.19. A polaroid filter is present in front of the lens of the camera. Without this analyzer the interference pattern can not be observed.



Figure 9.19: Plane polariscope setup for optical stress measurements: LCD-screen, glass arch, polaroid filter, camera;

Analysis of the results

The stress optic law is used to produce the legend shown in Figure 9.20, which holds *for this case specifically* (i.e. $t = 65\text{mm}$ and $C = 2.72 \cdot 10^{-6}\text{mm}/N$).

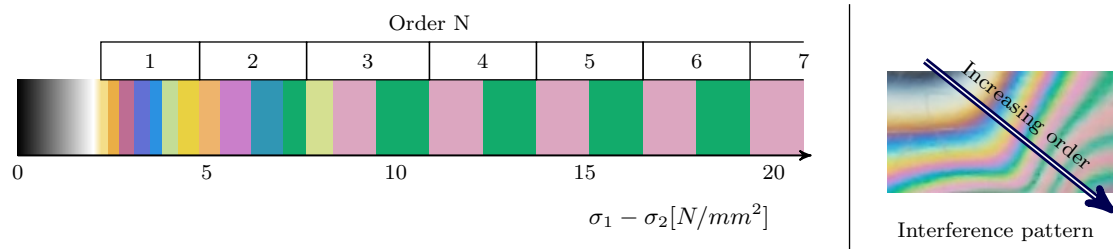


Figure 9.20: Color legend that holds for this experiment specifically ($t = 65\text{mm}$ and $C = 2.72 \cdot 10^{-6}\text{mm/N}$); Depending on the order, a certain color relates to a certain difference of the principal stresses;

Results

The interference pattern that occurs at a load of 20kN is shown in Figure 9.21a. The line of thrust corresponding to the load case, consist of two straight lines that run from the bottom of the supports, to the top in the middle. The interference pattern in the stones directly at the supports, is as expected from the finite element model shown in Figure 9.21b. The highest stress is reached at the bottom. Using the legend show in Figure 9.20, the maximum principal stress difference that occurs near the support, is estimated to be about 19N/mm^2 . This value is in accordance with the principal compressive stress of 20N/mm^2 , that occurs at the support in the finite element model shown in Figure 9.21b.

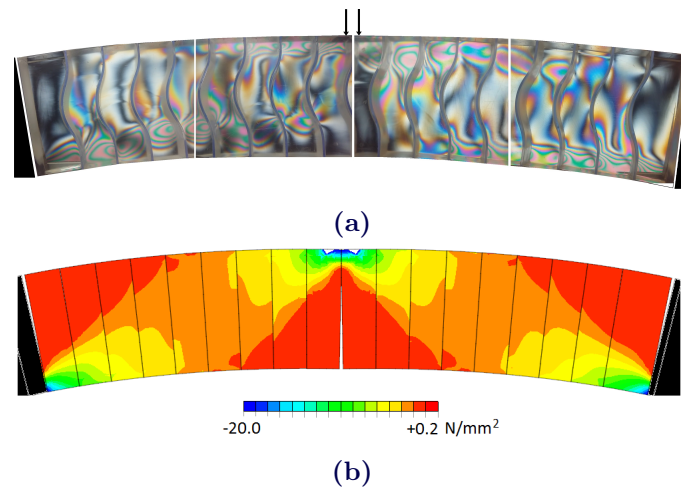


Figure 9.21: (a)Polaroid interference pattern at a load of 20kN; Composed from 4 separate tests, to show the interference pattern for the full length of the arch; (b)Principal compressive stress plot of the finite element model;

The rest of the observed interference pattern is highly affected by the brick-shape, which does not make contact in the middle half. Therefore the load is transferred through a contact point at the bottom and at the top. Roughly speaking, as the line of thrust goes from the bottom to the top, the stresses transferred at the contact points at the top increase, while the stresses at the bottom decrease.

An asymmetrical trend can be observed as well, since the shear resisting bricks all ‘point’ into the same direction. On the left side the shear component is therefore transferred at the bottom and at the right side it is transferred at the top. The right side transfers the

stresses more gradually, thus this configuration ('belly' facing the middle) is preferred if the bricks would be placed symmetrically using a key-stone.

In Figure 9.22 a comparison is made between the stiff 1mm-PU interlayer and the soft 4mm-PVC interlayer, the maximum occurring principal stress differences are about $16N/mm^2$ and $22N/mm^2$ respectively. As expected the stresses are distributed better for a softer interlayer, resulting in lower principal stress differences.



Figure 9.22: Polaroid interference pattern at a load of 20kN; (left) 4mm-PVC interlayer; (right) 1mm-PU interlayer;

9.3.5 Failure behavior

To establish whether the failure behavior of a glass arch is brittle or ductile, destructive displacement-control tests have been executed. A 1mm-PU interlayer was applied in this experiment. This stiff and thin interlayer assures that the glass-failure occurs before the bottom touches the steel frame.

Results

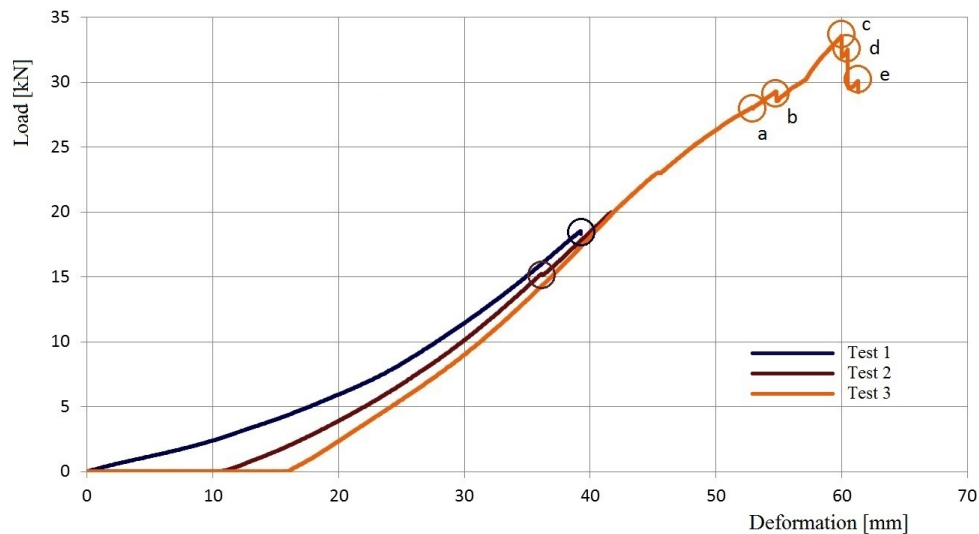


Figure 9.23: F,u-diagram for the three subsequent tests in which the failure behavior was investigated; The same specimen has been used for these test and was thus partially damaged at the start of the second and third test;

Three destructive tests have been executed, as shown in Figure 9.23. The circles indicate the moments at which fracture occurred. The first test was aborted when a piece of the left support broke off, which is shown in Figure 9.24. During the second test a piece of the right support broke of, as shown in Figure 9.25. After breakage, the resistance of the arch was able to increase, which corresponds to a **ductile** failure-behavior. At 20kN the test was aborted.

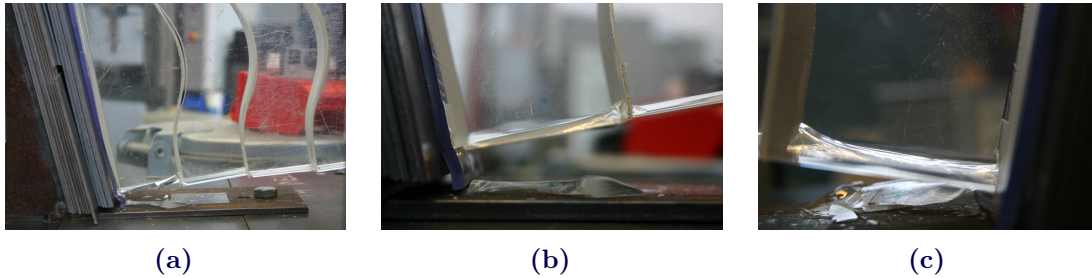


Figure 9.24: Failure test 1; (a) Left support fracture; (b) Close-up (c) Close-up backview;

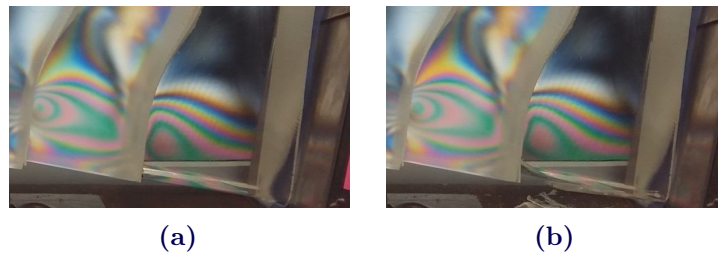


Figure 9.25: Failure test 2: Right support fracture (a) No crack; (b) Cracked;

During the third test multiple fractures occurred, as shown in Figure 9.23 and Figure 9.26. The first fracture occurred in the brick onto which the load was applied. Subsequently a second crack occurred in this brick, simultaneous with a crack in a brick nearby. After both of these fracture the resistance of the arch was able to increase up to a higher point after breakage, which corresponds to a **ductile** behavior. After reaching a load of 33.5kN multiple fractures occurred in a short period of time. Judging from Figure 9.23, the resistance of the arch will probably not further increase after this point and thus the maximum resistance has most likely been reached. To keep the remaining bricks intact, the test was aborted.

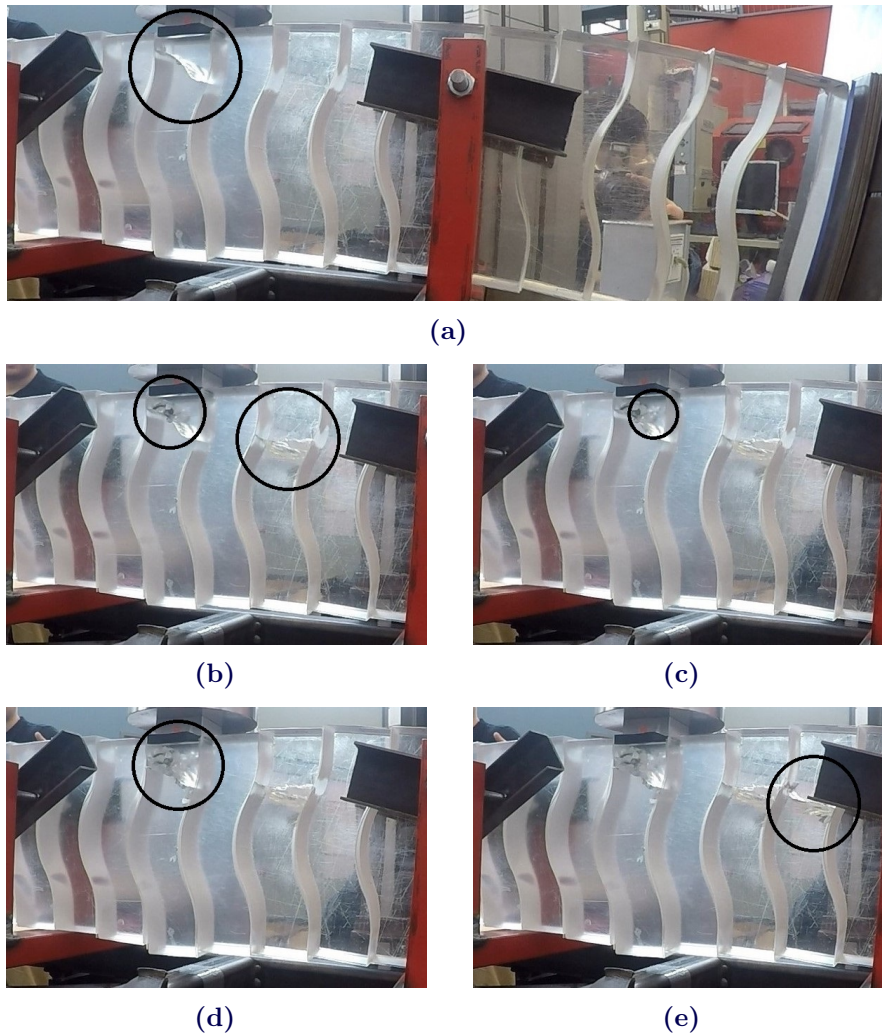


Figure 9.26: Failure test 3; Letters a,b,c,d and e correspond to indicated peaks in Figure 9.23;

9.3.6 Conclusions and Recommendations

Photographic displacement measurements

The measured displacement field correlates to the finite element analysis, which validates the analysis in Chapter 7. Additional validations for larger spans are recommended. Establishing a reliable support stiffness is of vital importance in order to make an accurate prediction of the displacement field.

Photo-elastic stress measurements

In the bricks directly adjacent to the supports, the interference pattern is as may be expected from the triangular stress distribution that corresponds to the position of the line of thrust. The middle two bricks show a similar pattern. The maximum principal stress difference is about $19N/mm^2$.

The interference pattern for other bricks is highly affected by the brick-shape, which does not make contact in the middle half. The load is transferred through two contact points: at the bottom and at the top. Roughly speaking, as the line of thrust goes from the bottom to

the top, the stresses transferred at the contact points at the top increase, while the stresses at the bottom decrease.

An asymmetrical trend can be observed, since the shear resisting bricks all ‘point’ into the same direction. On the left side the shear component is therefore transferred at the bottom and at the right side it is transferred at the top. The configuration in which the ‘belly’ is facing the middle is preferred since it transfers the stresses more gradually. This configuration is recommended if the bricks are placed symmetrically using a key-stone.

Failure behavior

During increment of the load fracture occurred at the left support, followed by the right support. In both cases a slice of the bottom broke off. The resistance was able to increase, which establishes a *ductile* failure-behavior.

Further incrementing the load then caused the brick onto which the load was applied to break, followed by a nearby brick. The resistance was still able to increase, emphasizing the *ductile* failure-behavior. After several other fractures, an increase of the resistance was not expected. The maximum applied load was $33.5kN$.

Fracture of a glass arch may be expected at the supports, where the highest compressive stress concentrations occur. Some fractured bricks do not affect the safety of the bridge. Replacement is recommended when several adjacent bricks are cracked, which means that it can no longer be guaranteed that they remain in place.

V Conclusions and Recommendations

10	Conclusions and Recommendations	137
	10.1 Introduction	137
	10.2 General results and conclusions	137
	10.3 Conclusions and recommendations for case study	138
	10.4 Recommendations for future re- search	139

10 Conclusions and Recommendations

10.1 Introduction

The objective of this research is to understand the structural behavior of an arched glass masonry bridge, which enables making a reliable safety assessment and well-grounded design choices. First the results and conclusions concerning arched glass masonry bridges in general are provided. Subsequently the conclusions and recommendation that hold specifically for TU Delft's glass masonry bridge design are presented. Finally, several recommendations for future research are given.

10.2 General results and conclusions

Instability of an arch can occur either due to an asymmetric load configuration, or due to support movements. To which instability-cause a circular arch is susceptible, depends on its geometry. A diagram derived in this report, can be used to distinguish four geometry-categories. These categories show whether a certain geometry is susceptible to support movements, an asymmetrical load scenario, neither of these or both.

A second design diagram has been derived in this report, which enables optimizing the stability under support movements. Given a certain span and a certain volume of glass, the rise and thickness corresponding to the maximum stability can be obtained.

From the investigation concerning the stability under an asymmetrical crowd load, a third design-diagram resulted. Given the rise and span, it provides the minimal required thickness related to sufficient stability under an asymmetrical crowd load.

After investigating the stability related failure, the strength-related failure was investigated. A glass element will typically fail in tension and not in compression. Although a glass brick in an arched masonry bridge is loaded in compression, tensile stresses will always be introduced due to imperfect conditions. A *local* effect occurs due to the imperfect flatness of the glass surfaces will result in peak stresses at the positions of contact. Due to the orientation of these peak stresses with respect to one-another, tensile stresses will be introduced. A *global* effect results from a certain eccentricity in the position of the line of thrust of the arch. This will result in a discontinuous stress distribution, which will introduce tensile stresses.

The typical triangular stress distribution that results from the eccentricity of the line of thrust (*global effect*), will cause a tensile stress if the eccentricity is bigger than $1/6$ of the arch its thickness. If the eccentricity becomes higher, the triangular stress distribution will act on a part of the brick only. Due to this discontinuous loading, tensile stresses are introduced perpendicular to the loaded direction. The aspect ratio of the bricks will affect the tensile stresses that occur. The tensile stress that occurs increases from zero to approximately its maximum value, as the width/height-ratio increases from zero to one. The maximum tensile stress is also depended on the eccentricity of the line of trust. As

the eccentricity approaches the boundary of the arch the tensile stresses rapidly increase. By application of an interlayer the eccentricity and thus the occurring maximum tensile stress can be limited.

Application of a sufficiently resilient interlayer can assure an adequate stress transfer between bricks, thereby resolving the problem caused by the *local effect*. To achieve this, the surfaces should be in contact before too high tensile stresses can develop. To formulate a maximum interface-stiffness that resolves the local problem, the following formula was derived:

$$\frac{E_{int}}{t_{int}} \leq \frac{\sigma_{contact}}{2\Delta} \quad \text{provided that} \quad t_{int} \geq \frac{2\Delta}{1 - \frac{\sigma_{avg}}{E_{int}}}$$

In this formula the maximum ratio for the material's young's modulus E_{int} and the interlayer's thickness t_{int} depends on the maximum deviation of the surface Δ and the compressive stress for which there should be full contact $\sigma_{contact}$, which is set to $20N/mm^2$. The ratio is only valid provided that the interlayer is sufficiently thick to accommodate for the expected deformations for the applied load σ_{avg} . In deriving the maximum-stiffness requirement, lateral expansion of the interlayer was disregarded. Therefore this formula may serve as a starting point for interlayer selection, but cannot be used for strength verifications.

From the experimental research in which a 1m glass arch was loaded till failure, a ductile failure behavior could be concluded. The resistance was able to increase after several fractures. Fracture of a flat glass arch may be expected at the supports, where the highest (compressive) stresses occur. It may be wise to apply a less stiff interlayer at the supports, thereby allowing for some rotations. This will decrease the eccentricity of the line of thrust at this point, which will reduce the stresses.

10.3 Conclusions and recommendations for case study

TU Delft's glass masonry bridge belongs to the geometry-category for which an analysis for both instability-causes is required, i.e. for support movements as well as for an asymmetrical load configuration. From the analytical analyses, it followed that the stability with respect to settlements is sufficient. The stability for both investigated asymmetrical load scenarios (i.e. an asymmetrical crowd load and an asymmetrical service-vehicle load) is sufficient as well. Although the stability with respect to the service vehicle may be sufficient, it is significantly lower than for the crowd load. To reduce the complexity of the project and to increase the safety of the bridge, it is recommended to place an obstacle that prevents a vehicle from entering the bridge.

The previous conclusions were validated by the numerical research. From the numerical research a sufficient stability of the bridge under a combination of an asymmetric load and support movements was concluded as well. Thus far it was assumed that the arch consists of solid glass bricks only. Since application of a resilient interlayer may be desired considering the strength, it is investigated how this affects the stability. It can be concluded that the design remains sufficiently stable if the stiffness of the interlayer E_{int}/t_{int} is higher than $26N/mm^3$. The numerical method was validated experimentally for a 1m-span glass arch. It is recommended to execute additional validations for larger spans. The obtained results highly depend on the validity of the boundary conditions. It is therefore highly recommended to monitor the support displacements frequently during

the bridge its lifetime.

To sufficiently limit the tensile stresses that can be introduced by the global and local effect, a maximum interlayer-stiffness of $40N/mm^3$ is formulated. The stiffness-interval, and several other (practical) requirements, provided a list of suitable materials. From this list, PVC, PU70 and PU90, were selected to be further investigated.

As interlayer, both 1mm-PVC as well as 4mm-PU70 are deemed suitable. They are both sufficiently stiff over time and adequately distribute the applied stresses. Before they can be applied, additional research is required to validate the long term behavior, which was estimated in this report. Therewith the effect of the non-orthogonal brick shape must be investigated, since the 1m-mock up showed that it may have a significant impact on the stress distribution.

The design for the case study is most likely feasible, since there exist interlayers for which a distributed stress transfer is provided, while maintaining sufficient stability. Before the safety of this design can be guaranteed, it should be verified that the interlayers function adequately for the full scale bricks and the system can resist the expected axial forces. Additionally the influence of the shear resiting brick-shape should be assessed, since in this report a orthogonal shape was regarded. For the interlayers, the long term time-dependent behavior should be verified and the temperature-dependency should be investigated.

10.4 Recommendations for future research

The proposed formula to define a maximum interface-stiffness, is based on 1D elastic behavior and a maximum surface deviation. It is recommended to improve this model, by investigating how the effect of lateral expansion of the interlayer and the accompanying friction can be incorporated. Additionally the model might be improved by implementing the stochastically defined surface profile rather than a maximum surface deviation. This could be done by making numerical models, which can than be validated by experiments.

It is expected that an arched glass masonry bridge in which an interlayer is applied will result in a higher load-capacity compared to a dry stack. In order to make a quantitative comparison, it is recommended to experimentally assess the capacity and span-limitations of both concept.

In this report an orthogonal brick shape was assumed for all analyses. It is recommended to investigate how a different (shear-resiting) shape affects the stress distribution. It would be valuable to determine how tensile stresses are developed in such shapes and where the maximum tensile stresses occur.

With respect to the interlayers, it is recommended to further investigate the time-dependent young's modulus of the PVC and PU when applied as interlayer. Additionally it is recommended to investigate how this is related to the temperature and the brick dimensions. This could be done by performing similar experiments as in this report, but for longer durations, at different temperatures and for different brick dimensions.

In this research lateral effects where not investigated. It is recommended to investigate the lateral cooperation of the bricks in the masonry pattern and investigate if the safety concept is adequate: If a brick fractures the loads should be accommodated by the surrounding bricks.

A	Tensile strength NEN 2608:2014	143
A.1	Strength assumption glass brick	143
B	Actions on a pedestrian bridge	145
B.1	Load cases	145
B.2	Load combinations	149
B.3	Load Scenarios	151
C	Derivations	153
C.1	Derivation l,f,t-notation of the boundary AB	153
C.2	Extraction and conversion of results regarding the span increase till collapse	153
C.3	Time-dependent stiffness derivation (Experiment)	155
C.4	Derivation differential equation of a cable	156
D	Assumptions and accuracy	157
D.1	Load distribution	157
D.2	Deviation of the line of thrust	158
D.3	Circle expression	160
E	Background information	161
E.1	Scale levels of imperfections	161
E.2	Fine and Kinney	162

A Tensile strength NEN 2608:2014

A.1 Strength assumption glass brick

The tensile strength of glass can be obtained from the 'NEN 2608:2014'. Although this code is based on float glass, it may be a good starting point to formulate an assumption for the tensile strength of cast glass bricks. The design value for the strength is provided by the following expression:

$$f_{mt;u;d} = \frac{k_a \cdot k_e \cdot k_{mod} \cdot k_{sp} \cdot f_{g;k}}{\gamma_{m;A}} \quad (\text{A.1})$$

The factors in this expression are quantified as follows:

- k_a takes into account the area over which a concentrated load is distributed. Since concentrated loads do not apply and the surface area of a brick is rather small compared to float glass panes, it can be assumed that $k_a = 1$.
- k_e represents the influence of the edge quality. It varies from 0.8 to 1. For annealed float glass it is 0.8 and for treated glass it is 1. It is expected that this effect does not apply on glass bricks, since the edges are not slender. They can be considered as polished surfaces rather than edges. Therefore a value of 1.0 is assumed.
- $k_{mod} = (\frac{5}{t})^{\frac{1}{c}}$ and represents the modification factor. It takes into account the duration of the load, using the load duration t , and the corrosion constant c . For outside conditions it holds that $c = 16$. When the main load of a bridge is permanent, it follows that for its reference period $k_{mod} = 0.29$.
- k_{sp} takes into account the surface-structure of the glass. For float glass it is 1.0 and for figure glass it is 0.8. The casting process is assumed to be less accurate than the float process. As a result, it is assumed that $k_{sp} = 0.8$.
- $f_{g;k}$ is the characteristic tensile bending strength. For annealed glass it holds that $f_{g;k} = 45\text{MPa}$.
- $\gamma_{m;A}$ is the material factor. It is equal to 1.6 if the wind is the governing variable load. For other situations it is equal to 1.8. The pedestrian traffic is expected to be the governing variable load. As a result, it is assumed that $\gamma_{m;A} = 1.8$.

Application of these factors in (A.1), provides the following design tensile strength:

$$f_{mt;u;d} = \frac{1 \cdot 1 \cdot 0.29 \cdot 0.8 \cdot 45}{1.8} = 5.8\text{MPa} \quad (\text{A.2})$$

The maximum principal tensile stress that occurs, will be checked against this design strength.

B Actions on a pedestrian bridge

B.1 Load cases

For the analysis of a glass pedestrian bridge, the loads stated in Table B.1 will be regarded. The corresponding Dutch Eurocodes that will be used are listed accordingly.

Table B.1: Loads and corresponding codes;

Load	code
Permanent load	-
Traffic load	NEN-EN 1991-2 (+NB)
Wind load	NEN-EN 1991-1-4+A1+C2:2011 (+NB)
Temperature load	NEN-EN 1991-1-5+C1:2011 (+NB)

B.1.1 Permanent load

The only permanent loading that has to be considered is the self-weight of the bridge. The parapets' structure is presumed to be independent is therefore not considered. No additional layer is applied on top of the glass arch. The self-weight is therefore based on the density of glass:

$$\rho_{glass} = 2500 \text{kg/m}^3 \equiv 25 \text{kN/m}^3$$

This can be converted to a surface-load, by multiplication with the thickness of the deck, t :

$$q_P = 25 \cdot t \quad \text{kN/m}^2$$

B.1.2 Traffic load

The NEN-EN 1991-2 formulates the following three possibilities for traffic loading on a pedestrian bridge:

- A distributed load, corresponding to a crowd of people, applied at unfavorable locations:

$$q_T = 5 \text{kN/m}^2$$

At the same time, a horizontal load corresponding to 10% of the vertical load occurs:

$$q_{T,hor} = 5 \cdot 0.10 = 0.5 \text{kN/m}^2$$

- A characteristic concentrated load applied at an area of $0.1 \text{m} \times 0.1 \text{m}$.

$$Q_{characteristic} = 10 \text{kN}$$

This load only has to be regarded for local effects.

- Loading caused by a service vehicle. If information about possible service vehicles is lacking, the configuration illustrated in Figure B.1 may be considered. The axle-loadings in this figure are:

$$Q_{SV1} = 80kN$$

$$Q_{SV2} = 40kN$$

At the same time, a horizontal load occurs, corresponding to 60% of the vertical load. Loading due to a service vehicle may be disregarded, if access is permanently prevented (e.g. by an obstacle).

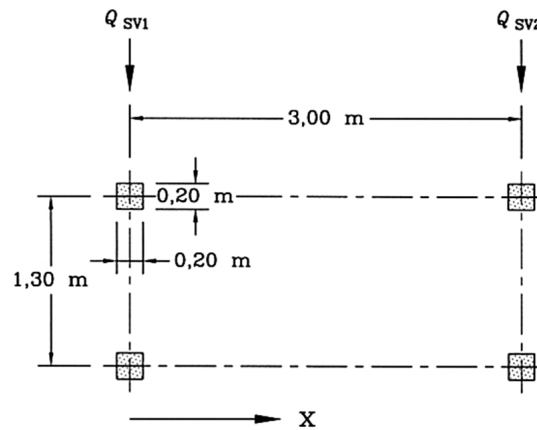


Figure B.1: Loading configuration due to service vehicle, taken from 'NEN-EN 1991-2+C1:2011';

The three traffic-loadings exclude one-another from occurring at the same time. If loading due to a service vehicle is considered, the characteristic vertical load does not have to be considered at all.

B.1.3 Wind load

The calculation of the wind load is based on the NEN-EN 1991-1-4+A1+C2:2011 and the corresponding national appendix. The location of the site is assumed to be in *wind region II* and in a *cultivated area*. The maximum bridge-height is assumed to be *lower than 7m*.

The following equation can be used to determine the wind load in direction i :

$$F_{w,i} = \frac{1}{2} \cdot \rho \cdot v_b^2 \cdot C_i \cdot A_{ref,i} \quad (\text{B.1})$$

where

$$\rho = \text{density of air } (1.25kg/m^3)$$

$$v_b = \text{the basic wind speed}$$

$$C_i = \text{the wind load factor in direction } i$$

$$A_{ref,i} = \text{the reference area in direction } i$$

The basic wind speed v_b , can be obtained from:

$$v_b = c_{dir} \cdot c_{season} \cdot v_{b,0} \quad (\text{B.2})$$

where

$$\begin{aligned} c_{dir} &= 1 && \text{(direction occurrence factor)} \\ c_{season} &= 1 && \text{(seasonfactor)} \\ v_{b,0} &= 27.0 \text{ m/s} && \text{for wind region II} \end{aligned}$$

The wind load factor C_i , can be obtained from:

$$C_i = c_e \cdot c_{f,i} \quad (\text{B.3})$$

where

$$\begin{aligned} c_e(z) &= \frac{q_p(z)}{q_b} && \text{(exposure factor)} \\ c_{f,i} &= \begin{cases} 1.3 & \text{for horizontal loads perpendicular to the deck} \\ 0.4 \cdot 1.3 & \text{for horizontal loads parallel to the deck} \\ \pm 0.8 & \text{for vertical loads} \end{cases} \end{aligned}$$

The factor for vertical loads $c_{f,ver}$, is based on the occurrence of turbulence, causing a deviation from the horizontal wind direction.

The exposure factor c_e , can be determined using Table NB.5 of the ‘NEN-EN 1991-1-4+A1+C2:2011’. For a height lower than 7m ($z \leq 7$) and for a site located in a cultivated area in wind region II, it holds that:

$$\begin{aligned} q_p(z \leq 7) &= 580 \text{ N/m}^2 \\ q_b &= \frac{1}{2} \cdot \rho \cdot v_b^2 \end{aligned}$$

Equation (B.1) can be rewritten as:

$$\begin{aligned} F_{w,i} &= q_{w,i} \cdot A_{ref,i} \\ \text{with} \\ q_{w,i} &= \frac{1}{2} \cdot \rho \cdot v_b^2 \cdot C_i \end{aligned} \quad (\text{B.4})$$

Equation (B.4) can be simplified using equations (B.3) till (B.4):

$$q_{w,i} = q_p(\leq 7) \cdot c_{f,i}$$

For different directions, the distributed wind loads are listed in Table B.2. In addition the corresponding reference area is stated.

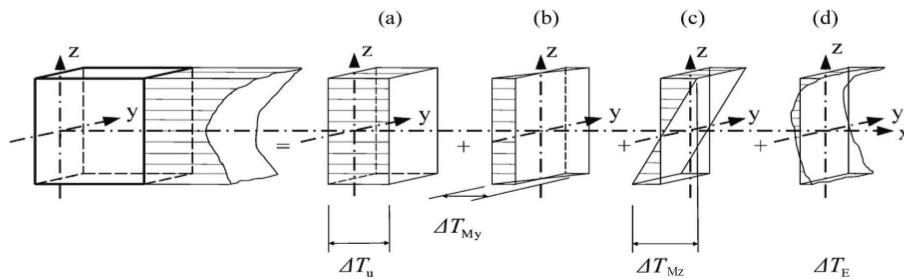
B.1.4 Temperature load

The calculation of the temperature load is based on the NEN-EN 1991-1-5+C1:2011 and the corresponding national appendix. Figure B.2 shows the essential components of temperature loading. The following four components are distinguished:

Table B.2: Distributed wind load;

Direction, i	$q_{w,i}$ [kN/m^2]	$A_{ref,i}$ [m^2]
Horizontal (\perp)	0.754	$Length \cdot thickness$
Horizontal (\parallel)	0.302	$Length \cdot thickness$
Vertical	± 0.464	$Length \cdot width$

- (a) An evenly distributed temperature component, ΔT_u
- (b) A linear variable temperature component around the z-axis, ΔT_{My}
- (c) A linear variable temperature component around the y-axis, ΔT_{Mz}
- (d) A non-linear temperature component, ΔT_E , which is in equilibrium with itself (No net loads as a result)

**Figure B.2:** Components of temperature loading, based on ‘NEN-EN 1991-1-5+C1:2011’;

The lateral effect caused by the component shown in Figure B.2(b) is neglected. It is assumed that the deck of the bridge is sufficiently wide to prevent lateral instability. In addition, this temperature component will most likely not be able to extend throughout the entire width of the deck. This can be attributed to the relatively low thermal conductivity of glass (compared to steel) and the relatively large deck width (compared to the deck height).

The evenly distributed component ΔT_u , is the result of varying temperatures throughout the seasons. In the Netherlands, the prescribed minimum and maximum temperatures of the atmosphere (in the shadow) are:

$$T_{min} = -25^{\circ}\text{C} \quad (\text{B.5})$$

$$T_{max} = +30^{\circ}\text{C} \quad (\text{B.6})$$

There is a difference between the temperature of the atmosphere and the temperature in the bridge deck. This difference depends on the thermal conductivity of the material that is used. A concrete deck corresponds to ‘deck type 3’. This deck type can be selected for glass as well, since the thermal coefficients of the materials are comparable:

$$\lambda_{glass} = 1\text{W/mK} \quad (\text{Table 5.3 in Chapter 5})$$

$$\lambda_{concrete} = 1.16 - 1.71\text{W/mK} \quad (\text{NEN-EN 1991-1-5+C1:2011})$$

The thermal conductivity of concrete is slightly bigger, which means this assumption is

slightly conservative. For ‘deck type 3’, the following equations apply:

$$T_{e,min} = T_{min} + 8 \quad (\text{B.7})$$

$$T_{e,max} = T_{e,max} + 2 \quad (\text{B.8})$$

To obtain the temperature decrease/increase, causing shortening/expansion, the following equations may be used:

$$\Delta T_{N,shortening} = T_0 - T_{e,min} \quad (\text{B.9})$$

$$\Delta T_{N,expansion} = T_{e,max} - T_0 \quad (\text{B.10})$$

where the initial temperature is

$$T_0 = 10^\circ\text{C} \quad (\text{B.11})$$

Combine (B.5), (B.7), (B.9) and (B.11), as well as (B.6), (B.8), (B.10) and (B.11). As a result, it holds that:

$$\Delta T_{N,shortening} = 27^\circ\text{C}$$

$$\Delta T_{N,expansion} = 22^\circ\text{C}$$

There may be a difference in sunlight exposure regarding the top and the bottom of the deck. Therefore a temperature gradient may occur, with respect to the height of the deck. Therefore a linear variable temperature component in vertical direction is taken into account (ΔT_{Mz}). This is in addition to the evenly distributed component.

For a concrete girder or plate, without an additional wearing layer, it holds that:

$$\Delta T_{M,heat} = 0.8 \cdot 15 = 12$$

$$\Delta T_{M,cool} = 1.1 \cdot 8 = 8.8$$

For a combination of ΔT_N and ΔT_M the following equations may be used:

$$\begin{aligned} \Delta T_M + \omega_N \cdot \Delta T_N \\ \omega_M \cdot \Delta T_M + \Delta T_N \end{aligned}$$

where

$$\omega_N = 0.35$$

$$\omega_M = 0.75$$

B.2 Load combinations

The calculation of the load combinations is based on the NEN-EN 1990+A1+A1/C2:2011 and the corresponding national appendix. To account for the possibility that the characteristic loads are exceeded, partial factors are introduced for ultimate limit state calculations. In this manner sufficient safety is provided in the ultimate limit state. It is unlikely that the extreme situation of all load cases occurs at the same time. For this reason combination factors are introduced. Using the partial- and combination factors, the following load

combinations are formulated:

$$\gamma_{P,sub} \cdot P \quad + \quad \gamma_{Q,i} \cdot \psi_{0,i} \cdot Q_i \quad (B.12)$$

$$\eta \cdot \gamma_{P,sub} \cdot P \quad + \quad \gamma_{Q,1} \cdot \psi \cdot Q_1 \quad + \quad \gamma_{Q,i} \cdot \psi_{0,i} \cdot Q_i \quad (B.13)$$

In expression (B.12) the permanent loading is the leading load case. In expression (B.13) one of the variable load cases is leading (Q_1 , with $\psi = 1.0$). Since three variable load cases are distinguished (i.e. traffic load, wind load and temperature load), this expression provides three load combinations. In case that the permanent load has a positive effect, $\eta \cdot \gamma_{P,sub}$ in expression (B.13) is replaced by $\gamma_{P,inf}$.

B.2.1 Partial factors

The partial factors depend on the consequence class of the structure. The consequences regarding loss of human life are considered to be *average*. Collapse of an innovative glass structure might result in bad publicity and resistance towards such structures. Therefore the economic consequences are considered *severe*. As a result, the structure is classified in *consequence class CC2*. This corresponds to a reliability index $\beta = 3.8$. The partial factors corresponding to this reliability index are given in Table B.3.

Table B.3: Partial factors γ ;

Load type	Permanent		Traffic	Wind	Temperature	
Symbol	$\gamma_{P,sup}$	$\eta \cdot \gamma_{P,sup}$	$\gamma_{P,inf}$	$\gamma_{Q,T}$	$\gamma_{Q,W}$	$\gamma_{Q,Te}$
Partial factor	1.30	1.20	0.9	1.35	1.5	1.5

B.2.2 Combination factors

As mentioned, it is unlikely that the extreme situation of all load cases occurs at the same time. Therefore the combination factors given in Table B.4 may be used.

Table B.4: Combination factors ψ_0 ;

Load type	Traffic	Wind	Temperature
Symbol	$\psi_{0,T}$	$\psi_{0,W}$	$\psi_{0,Te}$
Partial factor	0.4	0.3	0.3

B.2.3 Load combinations

Application of the factors partial factors (Table B.3) and combination factors (Table B.4) in expression (B.12) and (B.13), provides the factors given in Table B.5. Four combinations can be distinguished. In case that the permanent load has an advantageous effect, the corresponding factors are replaced by 0.90.

Table B.5: Load combinations;

	Leading load case	Permanent	Traffic	Wind	Temperature
1	Permanent	1.30	1.35 · 0.4	1.5 · 0.3	1.5 · 0.3
2	Traffic	1.20	1.35 · 1.0	1.5 · 0.3	1.5 · 0.3
3	Wind	1.20	1.35 · 0.4	1.5 · 1.0	1.5 · 0.3
4	Temperature	1.20	1.35 · 0.4	1.5 · 0.3	1.5 · 1.0

B.3 Load Scenarios

B.3.1 Fundamental load configurations

The worst case load scenario is composed by application of the loads at disadvantageous locations only. In order to establish which load configurations could be governing, several fundamental configurations are regarded. In Figure B.3 the axial diagrams of those configurations are shown. The values of some characteristic points are provided by Table B.6.

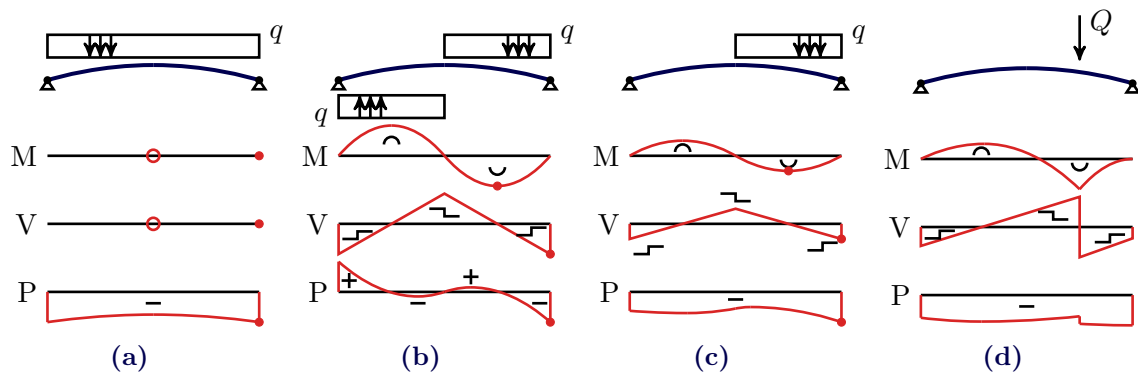


Figure B.3: Axial force diagrams for several fundamental load configurations; (a)Horizontally distributed load; (b)Up- and downward load; (c)Partially loaded [combination of a and b]; (d)A single point load;

Most beneficial would be the configuration illustrated in Figure B.3a, for which no internal moments (nor shear forces) occur. For the asymmetrical load configurations illustrated in Figure B.3b - B.3d, internal moments do occur. These internal moments result in an increase of the eccentricity of the line of thrust, which is disadvantageous regarding the stability.

Table B.6: Internal forces at the characteristic points indicated in Figure B.3; [In this table $\theta = \arctan \frac{4f}{l}$];

	M	V	P
(a)	0	0	$-\frac{1}{2}ql \cdot \frac{1}{\sin \theta}$
(b)	$-\frac{1}{32}ql^2$	$-\frac{1}{2}ql \cdot \cos \theta$	$-\frac{1}{2}ql \cdot \sin \theta$
(c)	$-\frac{1}{64}ql^2$	$-\frac{1}{4}ql \cdot \cos \theta$	$-\frac{1}{4}ql \cdot \left(\frac{1}{\sin \theta} + \sin \theta\right)$

B.3.2 Load scenarios

Stability

The worst case load scenario for the stability of an arched masonry structure, corresponds to the scenario where the highest eccentricity occurs. The eccentricity of the line of thrust follows from the following formula:

$$e(x) = \frac{M}{P}$$

Thus a high eccentricity is the result of a high internal moment and a low axial force. From the fundamental load configurations shown in Figure B.3, the worst case load scenario can be derived. The wind load may be directed in both ways and is thus configured as shown in Figure B.3b. This configuration causes the largest moment. The traffic load will always be directed downwards and thus the crowd load is configured as shown in Figure B.3c. The self weight has an advantageous effect and can be reduced by application of the appropriate partial factor. This resulted in the scenario illustrated in Figure B.4a (scenario 1). The presence of a vehicle is another possible traffic load and will not occur simultaneously with a crowd load, therefore the scenario illustrated in Figure B.4b is also investigated (scenario 2). One of these scenarios is governing for the stability.

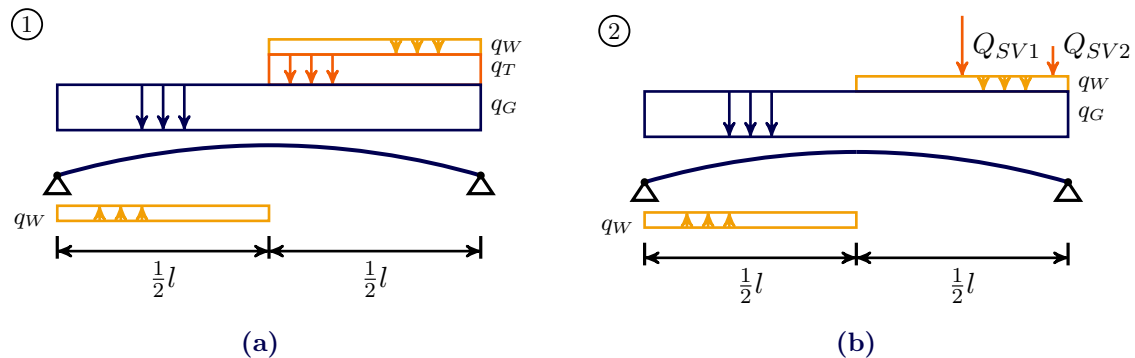


Figure B.4: Worst case load scenarios regarding the stability; (a)Scenario 1: Asymmetrically loaded by crowd; (b)Scenario 2: Asymmetrically loaded by vehicle;

C Derivations

C.1 Derivation l,f,t-notation of the boundary AB

Provided was the following equation in the R,β,t -notation, that expresses the boundary between region A and B in Figure 6.2:

$$\beta = \arccos \left(\frac{1 - \frac{t}{2R}}{1 + \frac{t}{2R}} \right) \quad (\text{C.1})$$

The goal is to rewrite this equation such that the slenderness is expressed in terms of the flatness. Given are the following relations for a circle segment, which follow from simple geometrical considerations:

$$R = \frac{f}{2} + \frac{l^2}{8f} \quad (\text{C.2})$$

$$\sin \beta = \frac{l}{2R} \quad (\text{C.3})$$

Equation (C.1) can be rewritten such that:

$$\frac{t}{R} = \frac{2(1 - \cos \beta)}{1 + \cos \beta} \quad (\text{C.4})$$

Equation (C.3) can be rewritten such that:

$$l = 2R \sin \beta \quad \rightarrow \quad \frac{t}{l} = \frac{t}{R} \cdot \frac{1}{2 \sin \beta} \quad (\text{C.5})$$

Substitution of (C.4) in (C.5), provides the *first part* of the expression:

$$\frac{t}{l} = \frac{2(1 - \cos \beta)}{1 + \cos \beta} \cdot \frac{1}{2 \sin \beta} \quad (\text{C.6})$$

The *second part* is obtained by multiplying (C.2) by $2f/l^2$ and then substituting (C.3) into the result. After some rearrangements, this provides:

$$\beta = \arcsin \left(\frac{\frac{f}{l}}{\left(\frac{f}{l}\right)^2 + \frac{1}{4}} \right) \quad (\text{C.7})$$

C.2 Extraction and conversion of results regarding the span increase till collapse

The contour lines in region C, as shown in Figure 6.2, were derived using Figure C.1. For certain values of the span increase percentage till collapse, points on the curves were extracted, which provided Table C.1.

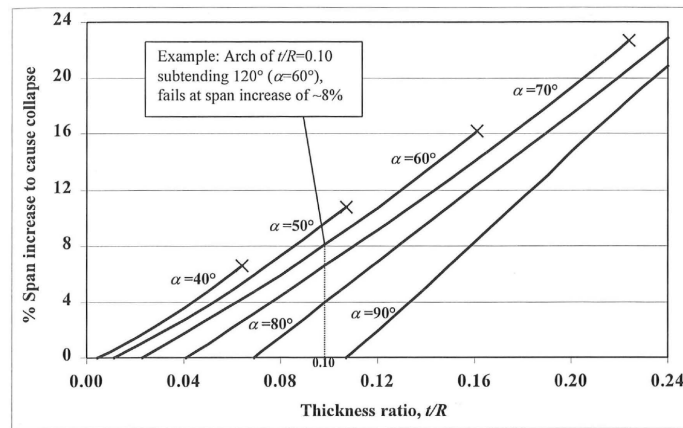


Figure C.1: Settlement analysis, taken from Oschendorf (2002);

Table C.1: Extracted results from Figure C.1;

β [°]	Span increase at collapse [%]					
	0	4	8	12	16	20
	t/R [-]					
40	0.00	0.04				
50	0.01	0.05	0.09			
60	0.02	0.06	0.10	0.13	0.16	
70	0.04	0.08	0.11	0.14	0.18	0.21
80	0.07	0.10	0.13	0.16	0.19	0.22
90	0.11	0.13	0.16	0.18	0.21	0.23

The results are now expressed in terms of the slenderness (t/l) and the flatness (f/l). The slenderness can be obtained from (C.5). The flatness can be obtained after rearranging (C.7) as follows:

$$\frac{f}{l} = \frac{\frac{1}{\sin \beta} - \sqrt{\left(\frac{1}{\sin \beta}\right)^2 - 1}}{2}$$

Through these formulas Table C.2 is obtained. This table is used to plot the contour lines in region C in Figure 6.2.

Table C.2: Span increase at collapse for certain combinations of the relative thickness and relative rise;

	Span increase at collapse [%]											
	0		4		8		12		16		20	
	f/l	t/l	f/l	t/l	f/l	t/l	f/l	t/l	f/l	t/l	f/l	t/l
40	0.18	0.00	0.18	0.03								
50	0.23	0.01	0.23	0.03	0.23	0.06						
60	0.29	0.01	0.29	0.04	0.29	0.06	0.29	0.07	0.29	0.09		
70	0.35	0.02	0.35	0.04	0.35	0.06	0.35	0.08	0.35	0.09	0.35	0.11
80	0.42	0.04	0.42	0.05	0.42	0.07	0.42	0.08	0.42	0.10	0.42	0.11
90	0.50	0.05	0.50	0.07	0.50	0.08	0.50	0.09	0.50	0.10	0.50	0.12

C.3 Time-dependent stiffness derivation (Experiment)

In Chapter 9, the time-dependent stiffness for several interlayers was derived, based on the results from the stacked glass-interlayer experiment. To do so, the relationship between the *displacement* and the *time* is approximated by a natural logarithm, which will be shown here. For PVC the measurements and corresponding trends lines are shown in Figure C.2. The first 48 seconds have not been included, since the load was applied during this period. When observing the measurements on a logarithmic time-scale it can be observed that they are on a straight line, which means that the behavior can indeed be approximated by a logarithmic trend. Initially the measurements show some deviation from the straight line (between 48 and 100sec), which can be attributed to the fact that the load was not immediately applied at $t = 0$ seconds (but over a period of 48seconds). This does however not significantly affect the prediction for longer durations.

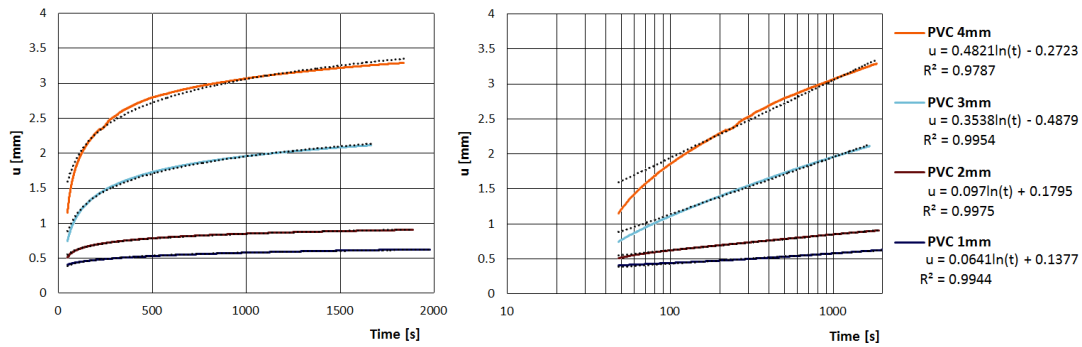


Figure C.2: Displacement in time for PVC interlayers; Trend lines are dashed; (left)Linear scale; (Right)Logarithmic scale;

All obtained constants from the trend lines and all coefficients of determination, are provided by Table C.3.

Table C.3: Constants for the trend lines [$u(t) = A \cdot \ln(t) + B$] and corresponding coefficients of determination [R^2];

Material	t_{int} [mm]	A	B	R^2
PVC	1	0.0641	0.1377	0.994
	2	0.0970	0.1795	0.998
	3	0.3538	-0.4879	0.995
	4	0.4821	-0.2723	0.979
PU70	1	0.0008	0.5192	0.986
	2	0.1166	0.1944	0.966
	3	0.0052	0.7679	0.983
	4	0.0017	0.3569	0.980
PU90	1	0.0019	0.9388	0.945
	2	0.0007	0.4169	0.940
	3	0.0060	0.6615	0.857
	4	0.0017	0.3569	0.980

C.4 Derivation differential equation of a cable

This derivation of the differential equation for a cable, is based on Welleman (2012). It is assumed that the cable has no axial deformation.

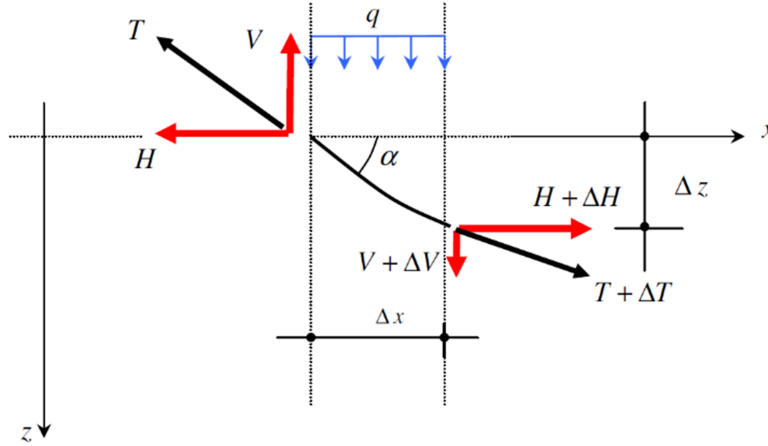


Figure C.3: Cable piece, taken from Welleman (2012);

From Figure C.3, the equilibrium equations are formulated:

$$\begin{aligned} -H + H + \Delta H &= 0 \\ -V + V + \Delta V + q\Delta x &= 0 \\ H\Delta z - V\Delta x + \frac{1}{2}q\Delta x^2 &= 0 \end{aligned}$$

This gives the following results:

$$\begin{aligned} \Delta H = 0 &\rightarrow H = \text{constant} \\ \frac{\Delta V}{\Delta x} &= -q \\ H\frac{\Delta z}{\Delta x} &= V - \frac{1}{2}q\Delta x \end{aligned}$$

For the limit where $\Delta x \rightarrow 0$, the equations become:

$$\begin{aligned} \frac{dV}{dx} &= -q \\ H\frac{dz}{dx} &= V \end{aligned}$$

Combining those equations, provides the differential equation for a cable:

$$H\frac{d^2z}{dx^2} = -q$$

D Assumptions and accuracy

D.1 Load distribution

The position of the line of thrust depends on the distribution of the loading. For a horizontally distributed load, the line of thrust is a parabola. For gravity loads of an arch with the shape of a catenary, the line of thrust is a catenary. For a circular segment with a low sagitta/span-ratio, the permanent loading can be assumed horizontally distributed. In reality this loading is distributed along the curve. To take this into account, the loading is projected on the horizontal by the following equation:

$$q_{P,x} = q_P \cdot \frac{dL}{dx} \quad (\text{D.1})$$

In this equation, L represents the length along the circular segment. This length can be obtained using the general mathematical equation for curve length:

$$L = \int_x \sqrt{1 + (z')^2} dx \quad (\text{D.2})$$

Substitution of expression (D.1) in expression (D.2) provides:

$$\frac{q_{P,x}}{q_P} = \sqrt{1 + (z')^2}$$

In this equation, z represents the function of the position of the arch. For a sagitta/span ratio of 1/20, this function is as follows:

$$z(x) = -\sqrt{\left(\frac{101}{40} \cdot l\right)^2 - \left(x - \frac{1}{2} \cdot l\right)^2} + \frac{99}{40} \cdot l \quad \text{for } x \in [0, l]$$

The derivation of this function can be found in Appendix D.3. For other ratios, this function can be derived in a similar manner.

In Figure D.1 the load distribution for several rise/span-ratios is illustrated.

As the ratio becomes smaller, the load distribution approximates a horizontal distribution. Therefore a horizontal load distribution can be considered an accurate approximation for small sagitta/span-ratios. Thus, for a 1/20-ratio it holds that:

$$q_{P,x} \approx q_P$$

Note that this approximation can be applied for any load-case, where the load is distributed along the curve. So besides self weight, it may be used for traffic and vertical wind loading as well.

The accuracy of this approximation is displayed in Table D.1. In reality, the distributed load has its maximum at the endpoints of the arch. When using the approximation, the load at these locations is underestimated by only 2% (for the 1/20-ratio). The support reactions follow from the total load, which is underestimated by 0.7%. The approximation can be considered appropriate. As a result of this approximation, it can be concluded that the shape of the line of thrust is parabolic.

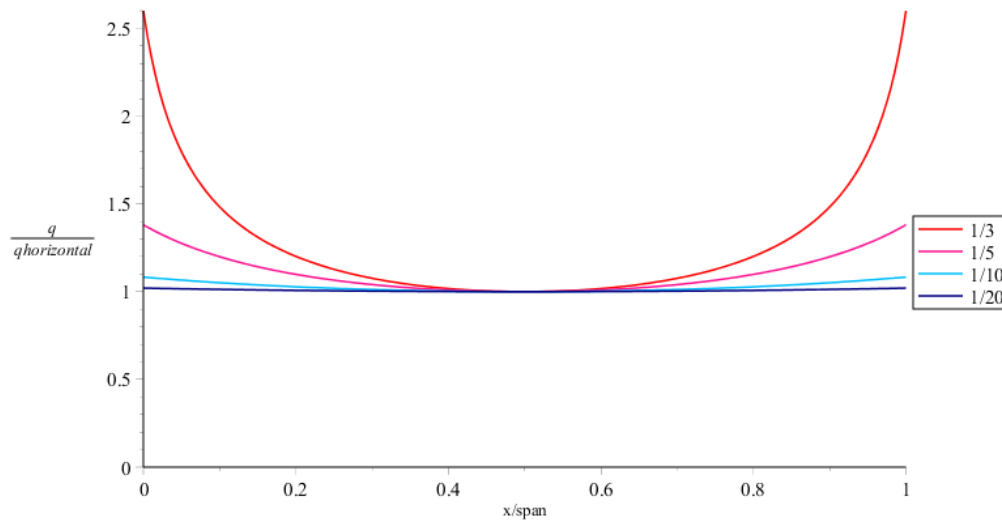


Figure D.1: Distributed loading of a circular segment, projected on the x-axis;

Table D.1: Accuracy of ‘horizontally distributed load’-assumption;

Sagitta/span-ratio [-]	Local load underestimation [%]	Total load underestimation [%]
1/3	160	27.4
1/5	38	10.3
1/10	8	2.6
1/20	2	0.7

D.2 Deviation of the line of thrust

When considering a horizontally distributed loading on an arch, it is known that the line of thrust has the shape of a parabola. However, the rise of this parabola remains unknown. This depends on the geometry of the arch. Once the horizontal support reaction is known, the rise can be computed using:

$$f = \frac{q \cdot l^2}{8 \cdot H} \quad (\text{D.3})$$

Since an arch is statically undetermined, the horizontal support reaction can not be obtained directly. One method, is to replace one of the support by a roller support. Due to the loads, there will now be a horizontal displacement at the location of this roller support. The force necessary to return the support to its original location, is the horizontal support reaction. The following equation is based on this principle (Welleman, 2012):

$$H = - \frac{\int_0^l M \cdot z \, dx}{\int_0^l z^2 \, dx} \quad (\text{D.4})$$

Using equations (D.3) and (D.4), the line of thrust can be computed. For several sagitta/span-ratios, the arch’s geometry (circular segment) and the corresponding lines of thrust are displayed in Figure D.2. For the 1/3-ratio, the eccentricity of the line of thrust is quite significant compared to the eccentricity for smaller ratio’s.

Figure D.3 provides a better display of the eccentricity.

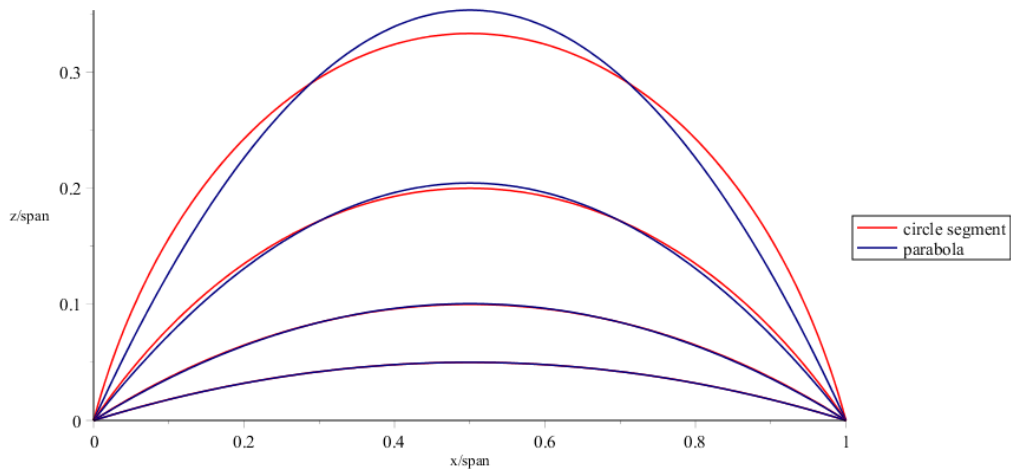


Figure D.2: Position of the Arch and line of thrust, for several s/l -ratios;

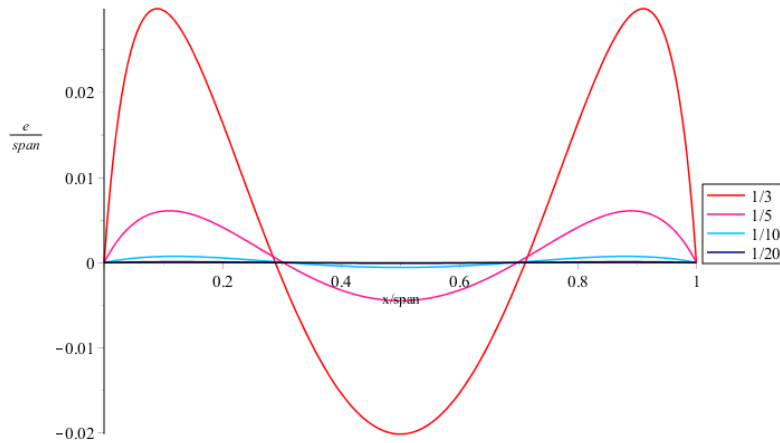


Figure D.3: Deviation of the line of thrust relative to the position of the arch, for several s/l -ratios;

For the $1/20$ -ratio, the circle-segment approaches the line of thrust quite well. A small eccentricity remains:

$$e \approx 9.2055 \cdot 10^{-5} \cdot l$$

This eccentricity is relatively small, compared to the eccentricity that arises in case of asymmetrical loads. Therefore these initial eccentricities can usually be neglected. *Neglecting the initial eccentricity, means that the geometry of the arch can be approximated by a parabola.*

D.3 Circle expression

In a xz -plane, the general equation for a circle can be formulated as follows:

$$(x - a)^2 + (z - b)^2 = r^2 \quad (\text{D.5})$$

with radius r , and center (a, b)

The following expression can be used to obtain the radius, given the sagitta (rise of a circular segment) and span:

$$r = \frac{s}{2} + \frac{l^2}{8s} \quad (\text{D.6})$$

with sagitta s and span l

If the arch spans from $x = 0$ to $x = l$, it follows that:

$$a = \frac{1}{2}l \quad (\text{D.7})$$

For a z -axis pointing downward, it holds that:

$$b = r - s \quad (\text{D.8})$$

Substitution of expressions (D.6), (D.7) and (D.8) in (D.5) and application of the sagitta/span-ratio ($\frac{s}{l} = \frac{1}{20}$), provides:

$$\left(x - \frac{1}{2} \cdot l\right)^2 + \left(z - \frac{99}{40} \cdot l\right)^2 = \left(\frac{101}{40} \cdot l\right)^2 \quad (\text{D.9})$$

Solving (D.9) for z , taking into account the relevant domain, provides the following function:

$$z(x) = -\sqrt{\left(\frac{101}{40} \cdot l\right)^2 - \left(x - \frac{1}{2} \cdot l\right)^2} + \frac{99}{40} \cdot l \quad \text{for } x \in [0, l] \quad (\text{D.10})$$

E Background information

E.1 Scale levels of imperfections

The magnitude and type of imperfection (overall or random) is mostly related to the production method which is used. By post processing casted elements (overall) imperfections can be removed. Possible methods for post processing are:

- CNC-milling (Computer Numeric Control)
- Waterjet cutting
- Grinding
- Polishing

After post processing with a CNC-machine, the bricks appear to be flat. Most likely the overall brick imperfection is no longer present. However, smaller imperfections may still be present. They are randomly distributed and vary in magnitude. The so called *primary profile* (i.e. texture of a surface), is generally described by distinguishing the following terms:

- Waviness (wavelength shapes at mesoscale)
- Roughness (wavelength shapes at micro-/nanoscale)

To illustrate the difference between macro-, meso- and microscale, the waterjet cut brick in Figure E.1 is considered. At macroscale the curved shape of the brick is defined. The waviness that can be observed is a result of waterjet cutting a relatively thick object. On the right, a pattern relating to the roughness can be observed. Although the shape of these waves cannot be observed, its presence is illustrated by the white speckle pattern.

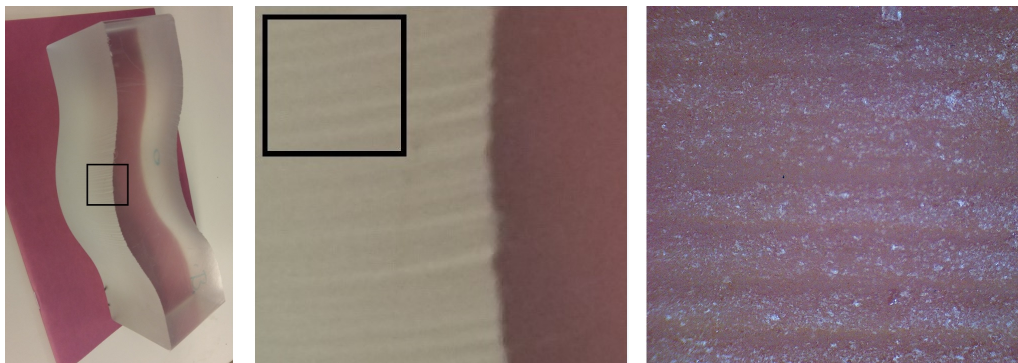


Figure E.1: Definition of a surface at macro-, meso- and microscale;

E.2 Fine and Kinney

For glass, the code ‘NEN 2608:2014’ evaluates the risk for a *structural element* of float glass, based on the method of Fine and Kinney. The method determines the risk based on several factors and is given by the following formula:

$$RD = LD \times ED \times SD \quad (\text{E.1})$$

In which,

RD is the Risk of Damage

LD is the Likelihood of Damage, intentional or unintentional

ED is the level of Exposure to the Damage

SD is the Seriousness of the consequences of the Damage

Those factors can be determined using Table E.1, E.2 and E.3, which are translations from the NEN 2608:2014. The results obtained from the tables will be partially subjective (e.g. it is arguable whether an event is ‘impossible’ or ‘virtually impossible’).

Table E.1: LD, translated from NEN 2608:2014;

Likelihood of damage, intentional or unintentional	LD
Impossible	0.1
Virtually impossible	0.2
Considerable, but very unlikely	0.5
Only possible at long term	1
Unusual, but possible	3
Very well possible	6
Can be expected	10

Table E.2: ED, translated from NEN 2608:2014;

Level of exposure to the damage	ED
Very rarely	0.5
Couple of times a year	1
Monthly	2
Weekly	3
Daily	6
Continuously	10

Table E.3: ES, translated from NEN 2608:2014;

Seriousness of the consequences of the damage	ES
No first aid treatment	0.1
Minor injuries, first aid treatment, without absence	1
Minor injuries, first aid treatment, with absence	3
Serious injuries, treatment by doctor and long aftercare	7
One fatality	15
More than one fatality	40
Catastrophe, many fatalities	100

Based on the result of the calculation, the damage that has to be considered can be determined by using Table E.4. This method applies on laminated glass panels. The laminated panels, consist of several layers. The expression of the damage is based on the number of layers that are broken.

Table E.4: Damage that has to be considered in calculation, translated from NEN 2608:2014;

Risk	Damage to structural element
$RD \leq 70$	One-sided lateral fracture
$70 \leq RD \leq 400$	Two-sided lateral fracture
$RD \geq 400$	Complete fracture of structural element

So for an RD value lower than 70, one layer of glass has to be considered broken. The structural calculation is carried out by observing the remaining layers. For an RD value bigger than 400, no layers remain intact. In this case the full element has failed. The structure will need a secondary load path to guarantee the safety.

According to the NEN 2608:2014, the consequence class of a structural element may be lower than that of the full structure, given that the RD value is low. This consequence class can be determined from Table E.5.

Table E.5: Determining of the consequence class of a single structural element, translated from NEN 2608:2014;

Consequence class full structure	Loading by persons or furniture	Risk to injury, RL			
		$RL \leq 3.8$	$3.8 < RL \leq 9.4$	$9.4 < RL \leq 10$	$10 < RL \leq 25$
CC1	-	CC1			
CC2	Inapplicable	CC1		CC2	
	Applicable	CC2			
CC3	Inapplicable	CC1	CC2		CC3
	Applicable	CC2			CC3

Bibliography

- Bensing, C., Behling, S., Ingenhoven, C. and Fuchs, A. (2010). *Innovative Design + Construction, manufacturing and design synergies in the building process*, Institut für internationale Architektur-Dokumentation, München. (pp. 82-84), ISBN: 3955531716. 13, 14
- Bos, F. P. (2007). *Towards a combined probabilistic/consequence-based safety approach of structural glass members*, In L.J. Sluys et al, HERON Vol. 52 No.1/2 Structural glass, Delft. (pp. 59-86). 50
- Bourhis, E. (2008). *Glass mechanics and technology*, 2 edn, Wiley-VCH, Weinheim. (pp. 5-7), ISBN: 3527679464. 39, 40
- Brincke, E. H. J. (2013). Glazen brug burgers' zoo opent wereld aan toepassingen, *Glas in Beeld*, nr. 5 . (pp. 8-11). 12
- Brincke, E. H. J. (2016). Lecture for course: Technoledge structural design, march 10, 2016. 52
- Dietrich, N., Jerry, S. and Bruce, K. (1995). *Glass Block*, Jester, T. C., Twentieth-century building materials: History and conservation, McGraw-Hill, New York. (p. 163). 19
- Haldimann, M., Luible, A. and Overend, M. (2008). *Structural use of glass*, Structural engineering documents 10, International Association for Bridge and Structural Engineering, Zürich. (pp. 51,58,60). 45, 46, 47
- Hartsuijker, C. and Welleman, J. W. (2007). *Constructiemechanica 3, Module: Stabiliteit van het evenwicht*, TU Delft, Delft. 31
- Heyman, J. (1995). *The stone skeleton: structural engineering of masonry architecture*, Cambridge University Press, Cambridge. (pp. 3-25), ISBN: 0521472709. 31, 32, 33, 34, 35
- Hoogenboom, P. C. J. (2014). Shell analysis course handout. 29
- Lomholt, I. (2014). Monumento madrid. www.e-architect.co.uk, consulted March 11, 2016. 23
- Louter, P. C. (2011). *Fragile yet ductile, structural aspects of reinforced glass beams*, PhD thesis, TU Delft, Wöhrmann Print service, Zutphen. (pp. 43-58). 40, 41, 43, 48, 49, 50
- Louter, P. C. (2016). Lecture for course: Technoledge structural design, february 18, 2016. 14
- Lyme, C. (2015). China completes the 'world's longest glass walkway' stretching a quarter-of-a-mile above a 980ft canyon. Dailymail: www.dailymail.co.uk, consulted April 13, 2016. 15

- McKenzie, H. W. and Hand, R. J. (1999). *Basic optical stress measurement in glass*, Society of glass technology, Sheffield. (pp. 3-20), ISBN: 0900682272. 128
- Nakamura, H. (2012). Optical house, hiroshima. www.nakam.info/en, photos by Koji Fujii, consulted March 11, 2016. 22
- Nijsse, R. (2003). *Glass in structures: elements, concepts designs*, Birkhäuser - Publishers for architecture, Basel. ISBN: 9783764364397. 11, 12, 13, 16
- Oikonomopoulou, F., Veer, F., Nijsse, R. and Baardolf, K. (2014). *A completely transparent, adhesively bonded soda-lime glass block masonry system*, In U. Knaack and T. Klein, Journal of facade design and engineering Vol. 2, No.3-4, IOS Press, Delft. (pp. 201-221). 19, 20, 23, 25, 41, 43, 44, 52, 53, 109, 120
- Oschendorf, J. A. (2002). *Collapse of masonry structures*, PhD thesis, University of Cambridge, Cambridge. (pp. 74-89). 32, 33, 60, 62, 154
- Pepi, J. W. (2014). *Strength properties of glass and ceramics*, Spie Press, Washington. (pp. xi and 3-8), ISBN: 9780819498366. 44, 45, 46, 47
- Piano, R. (2013). Maison hermes, tokyo. www.simlievler.wordpress.com, consulted March 16, 2016. 21
- Rinaldi, M. (2014). Go-ahead the glass bridge by thomas heatherwick. aasarchitecture.com, consulted April 14, 2016. 17
- Schittich, C., Staib, G., Balkow, D., Schuler, M. and Sobek, W. (2014). *Glass Construction manual*, 2 edn, Institut für internationale Architektur-Dokumentation GmbH and Co, München. (pp. 60-62, 90, 99-101), ISBN: 9780819498366. 40, 41, 42, 51, 52
- Snijder, A., Smits, J., Bristogianni, T. and Nijsse, R. (2016). *Design and engineering of a dry assembled glass block pedestrian bridge*, In Bos et al., Challenging Glass 5 - Conference on architectural and structural applications of glass, Ghent. (pp. 227-234). 4
- Townsend, S. (2014). Heatherwick to resurrect king's cross 'glass' bridge. www.architectsjournal.co.uk, consulted April 14, 2016. 17
- Veer, F. A. (2007). *The strength of glass, a nontransparent value*, In L.J. Sluys et al, HERON Vol. 52 No.1/2 Structural glass, Delft. (pp. 87-104). 40, 42, 47, 48
- Welleman, J. W. (2012). *Notities over kabels en bogen: Parametrisch modelleren met MAPLE*, Betonvereniging, Den Hoorn. (pp. 3-9, 13, 26-28, 34 50-57). 28, 29, 30, 31, 36, 37, 156, 158
- Wittenberg, D. and Krynski, M. (2010). *Design of a single span nine metre long glass bridge*, In Bos et al., Challenging Glass 2 - Conference on architectural and structural applications of glass, Delft. (pp. 227-234). 14, 15
- Wong, M. H. (2015). Visitors 'scream' as china's new mountainside glass walkway cracks. CNN: edition.cnn.com, consulted April 14, 2016. 15, 16

Illustrations chapter headers

Chapter	Description	Source
Chapter 1	An impression of the design for TU Delft's glass masonry bridge	Snijder (2015)
Chapter 2	Glass icicles: Glass bridge design consisting of two cantilevering structures	Nijse (2003)
Chapter 3	Crystal Houses in PC. Hoofstraat in Amsterdam	mvrdiv.nl
Chapter 4	Stone masonry arch	wall.alphacoders.com
Chapter 5	Cast glass production by Poesia Company in Italy	Oikonomopoulou et al., (2014)
Chapter 6	Analytical 3D plot of the line of thrust for varying arch thickness	Author
Chapter 7	Principal compressive stress plot of an arch segment	Author
Chapter 8	Glass block, such as applied in the Crystal Houses	Author
Chapter 9	Mock up of 1m span glass arch for testing	Author